



Institutt for energi-
og prosesssteknikk

Bacheloroppgave


Oppgavens tittel: Termiske Egenskaper av Semi-solid State Litium-ion Batterier	Gitt dato: 10.01.2022
	Innleveringsdato: 20.05.2022
Project title (ENG): Thermal Properties of Semi-solid State Lithium-ion Batteries	Antall sider rapport / sider vedlagt: 64/12
Gruppedeltakere: Emil Gjerde Dyb Kristian Lossius Skogrand Kigen Øyvind Kristoffer Høgseth	Veileder: Jacob Joseph Lamb Markus Solberg Wahl
Oppdragsgiver: Konfidensielt	Prosjektnummer: 22BIFOREN-003
	Kontaktperson hos oppdragsgiver: Konfidensielt


Fritt tilgjengelig:

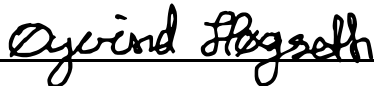
Tilgjengelig etter avtale med oppdragsgiver:

Rapporten frigitt etter:

Gruppedeltakere signaturer:







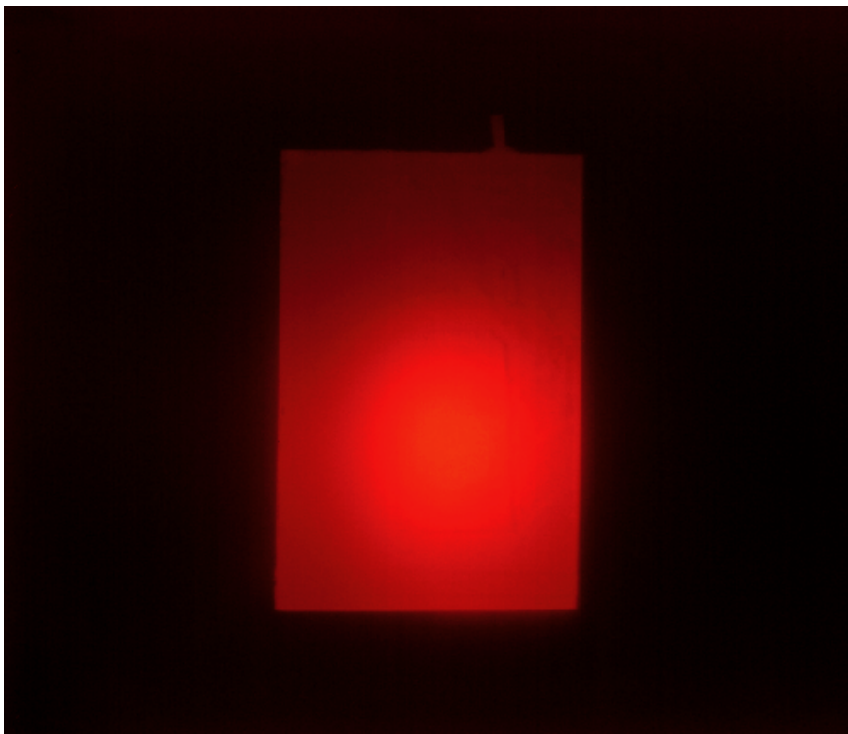


Norwegian University of
Science and Technology

FACULTY OF ENGINEERING
DEPARTMENT OF ENERGY AND PROCESS ENGINEERING
STUDY FIELD RENEWABLE ENERGY

Thermal Properties of Semi-solid State Lithium-ion Batteries

BACHELOR THESIS



Emil Gjerde Dyb
Kristian Lossius Skogrand Kigen
Øyvind Kristoffer Høgseth

Trondheim,
Spring 2022

Preface

All three authors chose to specialize in energy storage during our bachelor study in renewable energy engineering. Therefore, we were all interested in writing a bachelor thesis dealing with this area of study. Our interest in lithium-ion batteries in particular, originates from our shared view on the technology's arguably irreplaceable role in the world's transition to sustainable energy.

This interest was the primary motivation behind reaching out to the partner company for the thesis. Initially, we had minimal knowledge about semi-solid state lithium-ion batteries. Finally, however, we agreed that the thesis proposed was both intriguing and challenging. With our shared interest and excitement toward the related field of study, the group gladly accepted the proposed thesis and partnership.

We received fantastic help from different people during our work, which was necessary for the successful completion of the thesis. We are very thankful for all the help we received throughout the semester and would like to extend a special thanks to our internal supervisors, Jacob Joseph Lamb and Markus Solberg Wahl, for crucial guidance and help throughout the entire thesis. We would also like to thank our external supervisors who made the thesis possible and have assisted with crucial equipment, knowledge and assistance. Furthermore, we want to thank Odne Stokke Burheim and Lena Spitthoff for their help and input on the practical aspects of running experiments on thermal conductivity. In addition, we would like to thank the employees in the workshop department at Varmeteknisk, with Bjørn Volset at the forefront, for outstanding support and assistance in obtaining the necessary equipment for our thesis. Last but not least, we want to extend gratitude to Dominik Osinski, who contributed with the thermal camera, which added great visuals to our laboratory experiments.

Finally, we would like to thank each other for excellent collaboration and for maintaining a solid shared work ethic throughout the thesis.

Abstract

Thermal Properties of Semi-solid State Lithium-ion Batteries

The purpose of this project is to investigate the thermal conductivity, specific heat capacity and heat generation of semi-solid state lithium-ion batteries (LIB), and compare these to the thermal properties of conventional LIBs.

Semi-solid state LIB technology is a new and promising technology meant to improve on the industry standard. While the conventional LIB technology contains solid electrodes and liquid electrolyte, the electrodes and electrolyte of the semi-solid state LIBs are co-suspended, creating a clay-like structure. This way, several components and production steps are eliminated, making the technology cheaper and easier to manufacture, and lowering the energy consumption during production. The semi-solid state electrodes can also be produced thicker than conventional electrodes, causing an increase in relative percentage of active material to inactive material. This leads to an increase in energy density. Due to the clay-like structure, the batteries can be formed into different shapes, making them viable for wearable technology as well as being able to sustain more mechanical stress.

The theory section of this thesis describes the fundamentals of lithium-ion batteries, e.g. the composition of the batteries themselves and ageing mechanisms. This part of the thesis also presents the fundamentals of heat transfer, as well as some general battery terminologies.

To measure the thermal conductivity, a previously constructed setup made to measure thermal conductivity in electrode material is used. To measure specific heat capacity, thermocouples taped to an insulated water bath of Styrofoam with a given temperature is used. Here, the heated pouch cells are placed and the temperature development in the system is measured. After conducting formation cycles, the internal resistance is found by conducting Hybrid Pulse Power Characterization (HPPC) tests at different states of charge (SOC). The specific heat generation is then calculated from the internal resistance.

From the results gathered, the semi-solid state LIBs exhibits both a higher thermal conductivity and higher specific heat capacity. For the HPPC-testing, due to a broken current collector, broken tabs, or a suspected internal short circuit, only two of the conventional cells and unfortunately none of the semi-solid state cells were able to produce results. However, due to the increased thickness and therefore diffusion distance in the electrodes of the semi-solid state cells, the internal resistance and specific heat generation is expected to be greater than for the conventional cells.

Sammendrag

Termiske Egenskaper til Semi-solid State Litium-ion Batterier

Formålet med denne bacheloroppgaven er å undersøke termisk ledningsevne, spesifikk varmekapasitet og varmegenerering i semi-solid state litium-ion batterier (LIB), og sammenligne disse med de termiske egenskapene til konvensjonelle LIB.

Semi-solid state LIB-teknologi er en ny og lovende teknologi ment å forbedre industristandarden. Mens den konvensjonelle LIB-teknologien inneholder faste elektroder og flytende elektrolytt, er elektrodene og elektrolytten til semi-solid state LIB samsuspendert. Dette skaper en leirelignende struktur. På denne måten elimineres flere komponenter og produksjonstrinn, noe som gjør teknologien billigere og enklere å produsere, samt at produksjonen har lavere energiforbruk. Semi-solid state elektrodene kan også produseres tykkere enn konvensjonelle elektroder, noe som gir en økning i relativ prosentandel av aktivt materiale til inaktivt materiale. Dette fører til en økning i energitetthet. På grunn av den leirelignende strukturen, kan batteriene formes i forskjellige former, noe som gjør dem aktuelle for bærbar teknologi i tillegg til å være mer robust mot mekanisk påkjenning.

Teoridelen av denne oppgaven beskriver det grunnleggende ved litiumionbatterier, fra selve batterienes sammensetning til deres aldringsmekanismer. Denne delen av oppgaven presenterer også det grunnleggende om varmeoverføring, samt noen generelle terminologier.

For å måle den termiske ledningsevnen ble det brukt et tidligere konstruert oppsett laget for å måle varmeledningsevnen i elektrodemateriale. For spesifikk varmekapasitet ble det brukt et isolert vannbad av isopor med gitt temperatur, som de oppvarmede posecellene ble plassert i og temperaturutviklingen i systemet ble målt. Den interne motstanden ble funnet ved å kjøre HPPC-tester for forskjellige ladningstilstander, og den spesifikke varmegenereringen ble deretter beregnet fra den indre motstanden.

Fra resultatene måler semi-solid batteriene høyere for både termisk ledningsevne og spesifikk varmekapasitet. For HPPC-testingen, på grunn av en ødelagt current collector, ødelagte tabs eller en mistenkt intern kortslutning, var det bare to av de konvensjonelle cellene og dessverre ingen av semi-solid-cellene som var i stand til å gi resultater. Men på grunn av den økte elektrodetykkelsen og derfor diffusjonsavstanden i elektrodene til semi-solid-cellene, forventes den indre resistansen og dermed varmeutviklingen å være større enn for de konvensjonelle cellene.

Table of Contents

Preface	i
Abstract	ii
Sammendrag	iii
List of Figures	vii
List of Tables	ix
Glossary	x
Abbreviations	xii
Nomenclature	xiii
Computer Programs	xiv
1 Introduction	1
1.1 Objective	1
2 Theory	2
2.1 Fundamentals of Lithium-ion Batteries	2
2.2 Composition of a LIB	3
2.2.1 Electrodes	4
2.2.2 Separator	7
2.2.3 Electrolyte	8
2.2.4 Current Collectors and Tabs	8
2.2.5 Production of LIBs	8
2.2.6 Physical Properties of Electrodes	9
2.3 General Terminology	11
2.3.1 Terminal Voltage	11
2.3.2 Open Circuit Voltage (OCV)	11
2.3.3 Capacity	11
2.3.4 Internal Resistance	12
2.3.5 C-rate	12
2.3.6 State of Health (SOH)	12
2.3.7 State of Charge (SOC)	12

2.3.8	Depth of Discharge (DOD)	13
2.3.9	Constant Current and Constant Voltage	13
2.3.10	Hybrid Pulse Power Characterization (HPPC)	13
2.4	Degradation	14
2.4.1	Triggering Conditions	14
2.4.2	Ageing Effects on Negative Electrode	16
2.4.3	Ageing Effects on Positive Electrode	18
2.5	Thermal Properties of LIBs	19
2.5.1	Heat Generation in LIBs	19
2.5.2	Thermal Conductivity	21
2.5.3	Heat Capacity	21
2.5.4	Development Trends	22
2.6	Semi-Solid State Lithium-ion Batteries	22
2.6.1	General Composition	22
2.6.2	Technological Advances	23
2.6.3	Differences in Thermal Properties	24
2.7	Sustainability	24
2.7.1	Raw Material Extraction	25
2.7.2	Production and Use	25
2.7.3	End-of-life Management	25
2.7.4	Material Recovery Technologies	26
3	Methods	27
3.1	Input Data	27
3.2	Thermal Property Measurements	28
3.2.1	Thermal Conductivity (κ)	28
3.2.2	Specific Heat Capacity (c_p)	30
3.2.3	Heat Generation	32
3.3	Thermal Imaging	34
4	Results	36
4.1	Thermal Conductivity Test Results	36
4.2	Specific Heat Capacity Test Results	38
4.3	Heat Generation Test Results	40
4.4	Thermal Imaging Results	46

5 Discussion	49
5.1 Thermal Conductivity Tests	49
5.2 Specific Heat Capacity	51
5.2.1 Uncertainties and Improvements	52
5.3 Internal Resistance	53
5.3.1 Heat Generation from Internal Resistance	56
5.4 Thermal Imaging	57
6 Conclusions	58
6.1 Further Research	58
Bibliography	60
Appendices	A-1
A MATLAB Scripts	A-1
A.1 Specific Heat Capacity	A-1
A.2 Internal Resistance and Specific Heat Generation	A-3
B LabVIEW	B-1
B.1 Thermal Conductivity	B-1
B.2 Specific Heat Capacity	B-2
C Formation and HPPC-Program	C-1
D Excel Documents	D-1
D.1 Internal Resistance and Specific Heat Generation	D-1

List of Figures

1	Standard electrode potentials presented in the electrochemical series. Reprinted from Nagpal [12].	3
2	Schematic sketch of the main components of a LIB. Reprinted from Gregory L. Plett [14].	4
3	Main characteristics of the most common LIB chemistries. Reprinted from Zubi et al. [20].	5
4	Illustration of intercalation process in a LIB. Reprinted from Gregory L. Plett [14].	6
5	Production steps for a LIB. Reprinted from Bryntesen et al. [30].	9
6	Energy consumption of LIB production for factories producing 1450, 146000, 1 million and 50 million cells annually, respectively. Reprinted from Bryntesen et al. [30].	9
7	Cell energy density as a function of single side cathode thickness for three different cathode porosities. Reprinted from Kwade et al. [31].	10
8	Simplified sketch of the pathway through a semi-solid state cathode. Edited from Bryntesen et al. [30].	11
9	Standard CC-CV curve. Reprinted from Maranda [41].	13
10	Effect of temperature on LIB cycle life at 50 % DOD. Reprinted from Zia et al. [45].	15
11	LIB cycle life vs DOD. Reprinted from Zia et al. [45].	16
12	Illustration of unstable SEI development on the negative electrode. Reprinted from Barre et al. [43].	17
13	Cracking progress of an electrode particle. Reprinted from Xu et al. [48].	18
14	Dendrite formation. Reprinted from Gordon [49].	18
15	Illustration of the internal heat sources in LIBs [9, 52].	20
16	Differences in general composition between a semi-solid state LIB (left) and a conventional LIB (right). Reprinted from Bryntesen et al. [30].	23
17	Valuable metals in dead LIBs by weight. Reprinted from Yang et al. [68].	26
18	The three conventional LIBs to the left and the three semi-solid state LIBs to the right.	27
19	Schematic sketch of the thermal conductivity meter. Reprinted from Richter et al. [69].	29
20	Thermal conductivity meter prepared for measurements.	29
21	Styrofoam insulated water bath.	30
22	Styrofoam insulated water bath with two thermocouples.	31
23	Semi-solid state stack heating in the thermal chamber.	32
24	The three conventional pouch cells connected to the terminals in the thermal chamber, ready for testing.	33
25	Example of voltage and current development in a HPPC-test. Reprinted from Schweiger et al. [72].	33
26	Thermal camera.	34

27	Thermal resistance (r_{th}) as a function of sample thickness (Δx) for both technologies.	37
28	Thermal conductivity as a function of pressure.	38
29	Results from the heat capacity test. Three thermocouples measuring the temperature of three different spots in the insulated water bath. The initial temperature raise of the green curve is because this thermocouple lies on the bottom of the water bath directly under the cell stack.	39
30	Voltage and current as a function of time. This is the plot for conventional pouch cell number two for the whole cycling test. The voltage is slowly brought up to 4.2 V, where the formation process starts. Here, the battery slowly gets charged and discharged between 3.9-4.2 V. The HPPC-tests can be viewed from approximately 8.5 hours.	41
31	Voltage and current as a function of time during the formation.	41
32	Voltage and current as a function of time during all five HPPC-tests. The different HPPC-tests are marked with their corresponding SOC, as well as explanations to different stages of the current curve.	42
33	Voltage and current against time during the HPPC-test at 90 % SOC for conventional cell 2.	42
34	Voltage and current against time during the HPPC-test at 90 % SOC for conventional cell 2, zoomed in at the first pulses.	43
35	Voltage and current as a function of time for the whole cycling test for conventional cell 3.	44
36	Voltage and current against time during the formation process for conventional cell 3.	44
37	Voltage and current over time for the whole HPPC-process for conventional cell 3. All five HPPC-tests are shown as the thick vertical lines.	45
38	Voltage and current against time for conventional cell 3. The picture is zoomed in on the second HPPC-test performed under 90 % SOC.	45
39	Thermal imaging of pouch cell in the thermal conductivity jig with insulation. . .	47
40	Thermal imaging of pouch cell in the thermal conductivity jig without insulation. .	48
41	Heat dissipation in conventional cell (left) and semi-solid cell (right).	48
42	Alignment process of the steel rods with the circles drawn under the pressure gauges.	50
43	Voltage and current against time from $t = 0$ to end of formation process for conventional cells.	54
44	Three semi-solid state cells, the middle one having long enough tabs for formation and HPPC-testing.	55
45	Internal resistance as a function of SOC for both cells. Plots for both charge and discharge are presented in the figure.	55
46	Specific heat generation as a function of SOC for both cells. Plots for both charge and discharge are presented in the figure.	56

List of Tables

1	Cell data provided by the industry partner	27
2	Dimensions of the LIBs	28
3	Cell sample thicknesses for both technologies	36
4	Thermal conductivity for both technologies at different pressures	37
5	Measured and calculated values from the specific heat capacity test for both stacks	40
6	Total mass of each cell	40
7	Values for voltage and current used in internal resistance calculation	43
8	Internal resistance and irreversible heat generation for conventional cell 2 for all HPPC-tests performed at different SOC	43
9	Values for voltage and current used in internal resistance calculation	46
10	Internal resistance and irreversible heat generation for conventional cell 3 for all HPPC-tests performed at different SOC	46

Glossary

Active material	Material which participates in the chemical charge/discharge reactions
Additive	Material which give the electrodes favorable properties, such as improved performance, stability and safety
Anode	The electrode in an electrochemical cell where an oxidation reaction takes place
Calendar ageing	Unavoidable ageing characteristic and comprises all aging processes that lead to a degradation of a battery cell
Calendering	Process used to smooth, coat, or compress a material
Capacity	Total amount of electric charge stored within the battery
Cathode	The electrode in an electrochemical cell where a reduction reaction takes place.
Current collector	Provides conduction of electrons between the electrodes and the external circuits
Cycle ageing	Degradation associated with usage and is impacted by charge-discharge cycling
Deintercalatio	Removal of ions from the electrode
Depth of Discharge (DOD)	The amount of charge removed from the battery related to the total amount of charge that can be stored in the battery.
Electrode	An electrical conductor that makes contact with the nonmetallic circuit parts in a cell
Electrolyte	Medium that electrically conducts ions between the electrodes
Entropy	A thermodynamic quantity representing the unavailability of a system's thermal energy for conversion into mechanical work
Heat Capacity	Ratio of the heat absorbed by a material to the temperature
Intercalation	Process where ions get inserted into the electrode
Internal resistance	Opposition to electric current flow within the battery
Lithium plating	A degradation mechanism which decrease the capacity. Low temperatures and high charge C-rate leads to a reduction of Li-ions into lithium metal on the graphite electrode
Open Circuit Voltage	Maximum available voltage. The electrical potential difference between two disconnected terminals
Overpotential	The cause of irreversible energy loss in the form of heat generation
Porosity	The percentage of void space or pores in a material. It is the ratio between the volume of pores and the total volume of the material
Seperator	The separator is a material that lets certain particles through, while excluding others. Its purpose is to separate the electrodes from direct contact with each other to avoid internal short circuits
Solid Electrolyte Interphase (SEI)	A passivating layer on the negative electrode which forms when the cell is operated outside the electrochemical stability range of the electrolyte
State of Charge (SOC)	Measure of the amount of usable charge left in a cell
State of Health (SOH)	Measure of the battery's current capacity compared to its original capacity

Terminal Voltage	Voltage measured across the terminals of the battery when there is no load connected to the terminals
Thermal Conductivity	Material property that indicates a substance's ability to transfer heat through thermal conduction
Tortuosity	A measure of the length through a porous electrode divided by the length of that electrode itself, and can determine the length of the ionic pathways through the electrode

Abbreviations

BMS	Battery Management System
BTMS	Battery Thermal Management System
C-rate	Normalized Current-rate
CC-CV	Constant Current - Constant Voltage
DEC	Diethyl Carbonate
DMC	Dimethyl Carbonate
DOD	Depth of Discharge
EC	Ethylene Carbonate
EMC	Ethyl Methyl Carbonate
ESS	Energy Storage System
EV	Electric Vehicle
HF	Hydrofluoric Acid
HPPC	Hybrid Pulse Power Characterization
IR	Internal Resistance
LAM	Loss of Active Material
LCO	Lithium Cobalt Oxide
LFP	Lithium Iron Phosphate
LIB	Lithium-ion Battery
LLI	Loss of Lithium Inventory
LMO	Lithium Manganese Oxide
NCA	(Lithium) Nickel Cobalt Aluminium
NMC	(Lithium) Nickel Manganese Cobalt
NMP	n-Methylpyrrolidone
NTNU	Norwegian University of Science and Technology
OCV	Open Circuit Voltage
PC	Propylene Carbonate
PVDF	Polyvinylidene Fluoride
SEI	Solid Electrolyte Interphase
SOC	State of Charge
SOF	State of Function
SOH	State of Health
SOT	Standard Operating Temperature

Nomenclature

C_p	Heat capacity [$\text{J}\cdot\text{K}^{-1}$]
c_p	Specific Heat Capacity [$\text{J}\cdot\text{kg}^{-1}\cdot\text{K}^{-1}$]
$C\text{-rate}$	The rate of which the battery is charged or discharged [h^{-1}]
ϵ	Battery efficiency [%]
I	Current [A]
ΔI	Current difference [A]
κ	Thermal Conductivity [$\text{W}\cdot\text{m}^{-1}\cdot\text{K}^{-1}$]
L	Length of the electrode [μm]
L'	Length of the pathway through the porous electrode [μm]
η	Overpotential [V]
η_{ohmic}	Ohmic overpotential [V]
η_{con}	Concentration overpotential [V]
η_a	Activation overpotential [V]
τ	Tortuosity [-]
Q	Heat [J]
Q_e	Capacity [Ah]
\dot{Q}	Heat generation rate [W]
\dot{Q}_{jou}	Joule heat rate [W]
\dot{Q}_n	Total or maximum charge [W]
\dot{Q}_{re}	Reaction heat rate [W]
q_i	Specific irreversible heat generation [$\text{J}\cdot\text{kg}^{-1}$]
q_r	Specific reversible heat generation [$\text{J}\cdot\text{kg}^{-1}$]
q_x	Heat flux [$\text{W}\cdot\text{m}^{-2}$]
R_i	Internal resistance [Ω]
S	Entropy [$\text{J}\cdot\text{K}^{-1}$]
ΔS	Change in entropy [$\text{J}\cdot\text{K}^{-1}$]
T	Temperature [$^{\circ}\text{C}$ and K]
t	Time [s, min, and h]
ΔT	Change in temperature [$^{\circ}\text{C}$ and K]
U	Internal energy [J]
$U_{Terminal}$	Terminal voltage [V]
U_{OCV}	Open circuit voltage [V]
W	Work [J]

Computer Programs

During the thesis work, several computer programs were used. The most critical of these are listed below.

MATLAB: a high-level programming language and numeric computing environment developed by MathWorks. MATLAB allows matrix manipulations, plotting of functions and data, implementation of algorithms, creation of user interfaces, and interfacing with programs written in other languages [1].

LabVIEW: a graphical programming environment developed by National Instruments, and are used by engineers to develop automated research, data acquisition, instrument control, test automation, analysis and signal processing, validation, and production test systems. It is a complex program that is well design to build automated test systems for testing and measurements in many different applications [2].

MITS Pro: a high precision battery test equipment developed by ARBIN INSTRUMENTS. It serves as the interface platform for all of Arbin's testing systems; covering all energy storage testing applications including electrochemistry, basic life cycling, and real-world simulations [3].

Zotero: a software developed by Corporation for Digital Scholarship, and can easily collect, organize, cite, and share research. Zotero instantly creates references and bibliographies for any text editor, and directly inside Word, LibreOffice, and Google Docs [4].

Microsoft Excel: an industry leading spreadsheet software program, and a powerful data visualization and analysis tool developed by Microsoft. Advanced calculations, tables and graphical presentations can easily be run in Excel [5].

1 Introduction

With the increasing attention to global climate change, utilizing renewable energy and other low-carbon and sustainable solutions has grown increasingly important. In coherence with the rise of renewable energy and the electric revolution in the transport industry and storage applications, the demand for batteries is predicted to increase even further in the foreseeable future. As a result of this, the battery industry has grown more appealing than ever before. Many established and emerging companies intend to meet the increasing demand by building factories and improving their technology and production output.

The lithium-ion battery (LIB) is the industry standard secondary battery, powering most modern portable technology due to its superior energy density, power density, and lifetime. With this high energy efficiency, its applications extend to stationary solutions such as storing the surplus of energy from renewable sources and mobile solutions such as electric vehicles (EVs). Using this technology for such purposes leads to significant reductions in greenhouse gas emissions [6].

Researchers worldwide are looking into every possible solution for optimizing the LIB technology and, at the same time, making that solution economically viable. One new technology showing great potential is the semi-solid state LIB technology. Semi-solid state LIBs contain electrodes that are co-suspended with the electrolyte, creating a clay-like composition. In the production process of these batteries, several steps and components are eliminated such as the binding agent, casting-, drying-, and calendaring processes. Therefore, the electrodes can be made thicker, further increasing the ratio of active components to the inactive components. This again leads to an increase in energy density [7]. Another consequence of eliminating the previously mentioned production steps and components, is an easier and less energy consuming manufacturing process as well as reduced production costs. Such new technologies call for extensive research in areas such as performance, thermal properties, safety, and ageing. In this thesis, the thermal conductivity, specific heat capacity, and heat generation of the semi-solid state LIB will be researched and compared to a conventional LIB variant.

1.1 Objective

This project aims to measure and report the thermal properties of semi-solid state LIBs and compare these to those of conventional LIBs. The thermal properties in question are the thermal conductivity, specific heat capacity, and heat generation. These results will be presented and discussed to supplement the industry with valuable data to further research and develop the LIB technology. A common goal for the students is to learn about this new technology, as well as thermal property testing of LIBs.

For the industry, the semi-solid state LIB technology show great potential for lowering manufacturing cost as well as production output. With the higher energy density, the EV market could benefit from longer range and reductions in weight.

Semi-solid state LIBs apply relatively new technology with minimal openly available research and information as of writing this thesis. This presents an excellent opportunity to contribute the industry with valuable data on the technology. This bachelor thesis aims to produce results on the thermal properties of semi-solid state LIBs to aid the technology's future growth in the growing LIB market.

All measurements and experiments on the batteries will be carried out in collaboration with the supervisors in the battery laboratories of NTNU campus Gløshaugen.

2 Theory

The theory section of this thesis will focus on the fundamentals of LIBs, the differences between semi-solid state and conventional LIBs, and the thermal properties related to both technologies. The thermal properties to be investigated include thermal conductivity, heat capacity, and heat generation calculated from internal resistance. The internal resistance will be measured through HPPC-tests.

2.1 Fundamentals of Lithium-ion Batteries

Secondary LIBs are rechargeable electrochemical storage devices that transport lithium-ions from the anode to the cathode [8]. They are frequently used as power suppliers in electronic devices and electric vehicles, and for energy storage in buildings. Every cell in a LIB has two electrodes, an anode and a cathode, which can store lithium ions. Depending on how many lithium-ions are stored, the electrodes can have a difference in potential. This potential can move lithium-ions and electron current between the electrodes, the latter of which can be extracted to a load. Intercalation happens when ions get inserted into the electrode, while deintercalation describes the removal of ions from the electrode [9].

Some advantages of LIBs compared to other battery types is that they are highly energetic (high specific energy and power) and are therefore ideal for mobile applications. They also have no memory effect, and a slow self-discharge rate. Some disadvantages are that they are relatively expensive, the cell temperature has to be monitored in order to prevent temperature extremes, there is not yet an established industry standard for recycling large LIBs, protection circuits are required to protect the battery, and the batteries will start to degrade from the moment they are made (calendar ageing) [10].

A LIB consists of an anode, cathode, separator, electrolyte, and one positive and one negative current collector (see Figure 2) [11]. When cycled, the electrodes are connected to an external circuit through which the electrons travel. Due to a historic misconception, what is considered positive current (I [A]) in the literature always moves in the direction opposite of the direction the electrons move. The battery is protected by a casing, which varies depending on the size and intended use of the battery.

The basic working principle of the LIB is that when the battery is fully charged, the lithium ions are concentrated at the side of the anode and negative current collector. When the battery gets discharged, positively charged lithium ions travel from the anode to the cathode through the battery's electrolyte and separator. Simultaneously, the free electrons from the oxidized lithium atoms travel from the negative current collector to the positive current collector through an external circuit. This circuit is where the energy in the battery can be utilized by connecting a load. When the electrons reach the positive current collector, they merge with the Li-ions, which get reduced to neutral Li-atoms. When the battery is fully discharged, the lithium will be concentrated at the side of the cathode and positive current collector [8]. This process can be expressed as a chemical reaction, like the one presented in Equation 2.4.



	$\text{F}_2(\text{g}) + 2 \text{e}^- \longrightarrow 2 \text{F}(\text{aq})$	2.87	
	$\text{H}_2\text{O}_2(\text{aq}) + 2 \text{H}^+(\text{aq}) + 2 \text{e}^- \longrightarrow 2 \text{H}_2\text{O}(\text{l})$	1.78	
	$\text{MnO}_4^-(\text{aq}) + 8 \text{H}^+(\text{aq}) + 5 \text{e}^- \longrightarrow \text{Mn}^{2+}(\text{aq}) + 4 \text{H}_2\text{O}(\text{l})$	1.51	
	$\text{Cl}_2(\text{g}) + 2 \text{e}^- \longrightarrow 2 \text{Cl}^-(\text{aq})$	1.36	
	$\text{Cr}_2\text{O}_7^{2-}(\text{aq}) + 14 \text{H}^+(\text{aq}) + 6 \text{e}^- \longrightarrow 2 \text{Cr}^{3+}(\text{aq}) + 7 \text{H}_2\text{O}(\text{l})$	1.33	
	$\text{O}_2(\text{g}) + 4 \text{H}^+(\text{aq}) + 4 \text{e}^- \longrightarrow 2 \text{H}_2\text{O}(\text{l})$	1.23	
	$\text{Br}_2(\text{l}) + 2 \text{e}^- \longrightarrow 2 \text{Br}^-(\text{aq})$	1.09	
	$\text{Ag}^+(\text{aq}) + \text{e}^- \longrightarrow \text{Ag}(\text{s})$	0.80	
	$\text{Fe}^{3+}(\text{aq}) + \text{e}^- \longrightarrow \text{Fe}^{2+}(\text{aq})$	0.77	
	$\text{O}_2(\text{g}) + 2 \text{H}^+(\text{aq}) + 2 \text{e}^- \longrightarrow \text{H}_2\text{O}_2(\text{aq})$	0.70	
	$\text{I}_2(\text{s}) + 2 \text{e}^- \longrightarrow 2 \text{I}^-(\text{aq})$	0.54	
	$\text{O}_2(\text{g}) + 2 \text{H}_2\text{O}(\text{l}) + 4 \text{e}^- \longrightarrow 4 \text{OH}^-(\text{aq})$	0.40	
	$\text{Cu}^{2+}(\text{aq}) + 2 \text{e}^- \longrightarrow \text{Cu}(\text{s})$	0.34	
	$\text{Sn}^{4+}(\text{aq}) + 2 \text{e}^- \longrightarrow \text{Sn}^{2+}(\text{aq})$	0.15	
	$2 \text{H}^+(\text{aq}) + 2 \text{e}^- \longrightarrow \text{H}_2(\text{g})$	0	
	$\text{Pb}^{2+}(\text{aq}) + 2 \text{e}^- \longrightarrow \text{Pb}(\text{s})$	-0.13	
	$\text{Ni}^{2+}(\text{aq}) + 2 \text{e}^- \longrightarrow \text{Ni}(\text{s})$	-0.26	
$\text{Cd}^{2+}(\text{aq}) + 2 \text{e}^- \longrightarrow \text{Cd}(\text{s})$	-0.40		
$\text{Fe}^{2+}(\text{aq}) + 2 \text{e}^- \longrightarrow \text{Fe}(\text{s})$	-0.45		
$\text{Zn}^{2+}(\text{aq}) + 2 \text{e}^- \longrightarrow \text{Zn}(\text{s})$	-0.76		
$2 \text{H}_2\text{O}(\text{l}) + 2 \text{e}^- \longrightarrow \text{H}_2(\text{g}) + 2 \text{OH}^-(\text{aq})$	-0.83		
$\text{Al}^{3+}(\text{aq}) + 3 \text{e}^- \longrightarrow \text{Al}(\text{s})$	-1.66		
$\text{Mg}^{2+}(\text{aq}) + 2 \text{e}^- \longrightarrow \text{Mg}(\text{s})$	-2.37		
$\text{Na}^+(\text{aq}) + \text{e}^- \longrightarrow \text{Na}(\text{s})$	-2.71		
$\text{Li}^+(\text{aq}) + \text{e}^- \longrightarrow \text{Li}(\text{s})$	-3.04		

Figure 1: Standard electrode potentials presented in the electrochemical series. Reprinted from Nagpal [12].

In order to reverse the cycle, energy is added to the battery. This causes the lithium ions on the side of the positive current collector to move to the negative current collector through the electrolyte and separator [13]. In the electrochemical series presented in Figure 1, lithium has the lowest reduction potential of any element, allowing LIBs to have the highest possible cell potential. In addition, lithium is also the third lightest element and has one of the smallest ionic radii of any single charged ion. These factors allow LIBs to have high gravimetric and volumetric energy capacities and power densities, giving them an advantage in several different application areas [6].

2.2 Composition of a LIB

This section presents the most important components of a LIB:

- Electrodes - stores the energy in the form of lithium ions and electrons.
- Separator - separates the electrodes to prevent internal short circuit.
- Electrolyte - a pathway for ions to travel while insulating electrons.
- Current collectors - pathways for electrons to travel.
- Tabs - external connections to the electrodes.
- Outer casing - the outside layer of a LIB, often in the form of a pouch

A schematic of the main components of a LIB as well as the direction of electrons and ions during charge and discharge is presented in Figure 2. Note that the electrodes are not one uniform mass but rather particles that are pinched next to each other. The light blue substance surrounding the particles is the electrolyte. Note that the current moves in the opposite direction of the electron flow through the external circuit.

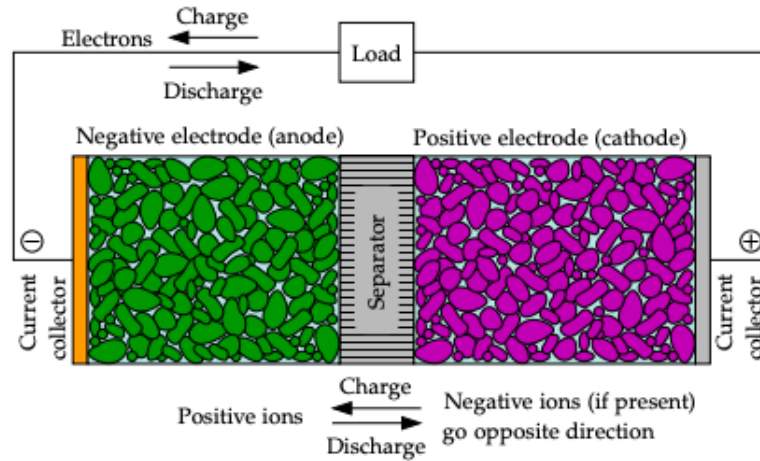


Figure 2: Schematic sketch of the main components of a LIB. Reprinted from Gregory L. Plett [14].

The terminologies unit cell, cell and battery describe three different stages of electrochemical storage. Unit cell is the smallest functional unit and contains one electrode pair as well the required auxiliary parts. Cell is the assembly of multiple unit cells placed in parallel inside a casing. Battery is the assembly of multiple cells, placed in a casing together with a cooling system and a battery management system. For this thesis, please note that the term "LIB" refers to Lithium-ion battery and the term "cell" refers to a unit cell, containing one electrode pair.

2.2.1 Electrodes

As stated above, the electrodes are critical components of all batteries, including LIBs. An electrode is typically a metallic conductor in a solid state, where an electrode reaction occurs between the electrode and the electrolyte. A typical battery unit cell consists of two electrodes and an electrolyte. The electrodes are connected through an external circuit, through which the battery can charge and discharge, given that the battery in question is a secondary battery [15].

During charging (electrolysis), oxidation occurs at the positive electrode, making it the anode, while reduction occurs at the negative electrode, making it the cathode. Conversely, during discharge, reduction occurs at the positive electrode, making it the cathode, and oxidation occurs at the negative electrode, making it the anode [15].

In LIBs, the negative electrode (anode) is usually carbon-based, either structured as hard carbon or graphite C_6 . Carbon is cheap, has a low delithiation potential versus Li/Li^+ , high Li diffusivity, high electrical conductivity, and relatively low volume changes during lithiation and delithiation [6, 16]. The most crucial difference between negative electrodes is their content of silicon. Commonly, modern negative electrodes have a small percentage of silicon, which increases the energy density but introduces challenges regarding cell stability, which limits the amount of silicon that can be used [17, 18].

The positive electrode (cathode) normally consists of transition metal oxide such as lithium-manganese-oxide (LMO), lithium-nickel-oxide, lithium-iron-oxide and lithium-cobalt-oxide (LCO), but lithium-iron-phosphate (LFP), nickel-manganese-cobalt (NMC), nickel-cobalt-aluminium (NCA) are also widely used [19, 20]. The use of cobalt is reduced in today's LIBs due to its high cost, rarity, toxicity, low thermal stability, and high degradation at high current (more on this in Section 2.7). Therefore, cobalt is being replaced with cheaper transition metals like manganese, nickel (even though this metal shares negative characteristics with cobalt), and iron, resulting in the most common chemistries in new LIBs being LFP and NMC [6, 16]. The cell's characteristics, such as power and energy density, resilience to degradation, cost, and safety, are highly dependent on the cathode material [9].

The conventional LIBs studied in this thesis are of the NMC type cathode. The NMC cells have high power density, maturity, durability, and performance [20]. A comparison of the characteristics of different LIB chemistries is presented in Figure 3 below.



Figure 3: Main characteristics of the most common LIB chemistries. Reprinted from Zubi et al. [20].

The electrode compounds are typically mixed with an active mass and additives to create better properties for the cell. The active material is the material that participates in the chemical charge/discharge reactions. The additives are materials that give the electrodes other favorable properties, such as improved performance, stability, and safety. They are often printed onto the metal current collectors, a process called coating [16, 20]. Typical additives in LIBs are carbon black, binder, pore-forming additives and wetting additives.

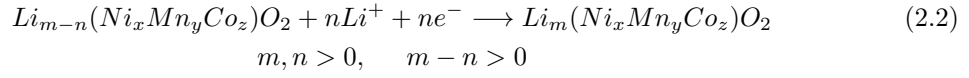
Anode

Oxidation always occurs at the anode in an electrochemical reaction [21]. An example of such an oxidation reaction is displayed in the half cell reaction in Equation 2.1 below [22].



Cathode

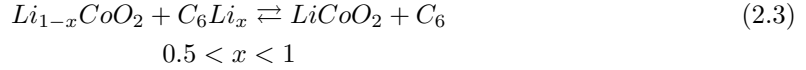
Reduction always occurs at the cathode in an electrochemical reaction [23]. An example of a reduction reaction is displayed in the half cell reaction in Equation 2.2 below [22].



As aforementioned, the electrodes on which the oxidation and reduction reactions occur switch with the flow of the energy in a battery. Therefore, the industry standard is to apply the terms **negative** and **positive electrode** instead of anode and cathode in the case of secondary batteries, meaning rechargeable batteries [23]. Furthermore, if the terms cathode and anode are used in the context of LIBs, the literature typically refers to a discharge setting.

Reactions

This section presents the chemical reactions during charge and discharge for LIBs. The discharge reactions go from left to right, whereas the charging reactions go from right to left. The general chemical reaction for an LCO battery is expressed in Equation 2.3 below:



Another widely used cathode material, as previously mentioned, is the NMC material. The general reaction for such batteries is expressed in Equation 2.4 [22]:

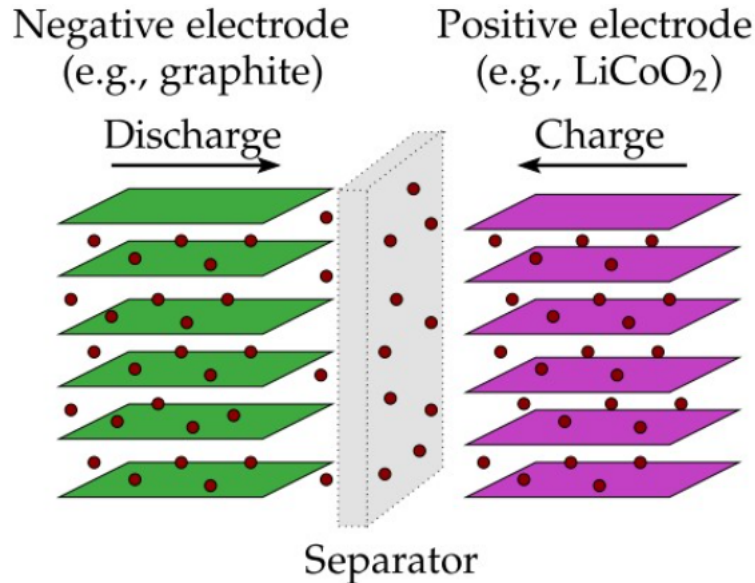
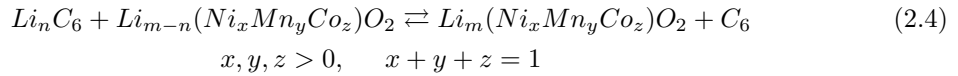


Figure 4: Illustration of intercalation process in a LIB. Reprinted from Gregory L. Plett [14].

Figure 4 above illustrates the intercalation and deintercalation process in a LIB. The red dots represent the Li-ions, the purple plates represent the positive electrode material, and the green plates represent the negative electrode materials. The Li-ions move between the electrodes through

the separator, where the arrows illustrate the directions the ions would move during discharge and charge. Although not included in this illustration, for a balanced reaction, the electrons would in this instance part with the electrode structure and move through an external circuit to the opposite electrode structure (direction also depending on the energy flow). It is important to note that the lithium ions are stored in the electrode structure rather than being a part of the electrode material itself [9]. This can be seen in the half cell reactions in Equation 2.1 and 2.2, but since the Li-ions (and electrons) cancel out in the total reaction, misconceptions can be made.

Each electrode has a certain amount of lithium-ions. Amongst other factors, this contributes to a cell's electrochemical potential. When these ions move from the negative electrode to the positive electrode during discharge, the potential difference between the electrodes decreases until equilibrium is reached, which is when the battery is considered fully discharged [9].

Cycling

The cell is usually stable only in a specific voltage interval or potential window. For the NMC-based LIBs used in this thesis, a typical potential window is between 2.8–4.3 V [24]. This means that the NMC cell only should be cycled within this voltage interval. If the cell is discharged below the cut-off voltage of 2.75 V, this can increase the irreversible capacity degradation and lower cycle and calendar life. On the other hand, if the cell is charged above the cut-off voltage of 4.25 V, it can decompose the electrolyte, creating toxic gases and, worst case, an explosion. The nominal voltage of NMC cells is around 3.6 - 3.7 V, depending on the cell manufacturer [25].

The NMC cell tends to catch fire after reaching 80 °C. Therefore, it is important to use a battery management system (BMS) that cuts off the cell once it is charged to 4.25 V. The operating temperature of LIBs also affect the cycle and calendaring ageing of the battery pack. Therefore, it is desirable to maintain a standard operating temperature (SOT) of 25 °C to maximize the battery lifetime. The operating temperature during charge and discharge should ideally be between 0 and 45 °C and –20 to 55 °C, respectively. As for voltage control, it is also important to use a battery thermal management system (BTMS) for temperature control to avoid potential heat damage and fire in the battery [25].

As mentioned above, the cycling life depends on the operating temperature. The cycle life of an NMC cell cycled at standard operating temperature can vary between 500 - 1500 cycles, depending on the application - for example, an electric vehicle (EV) or an energy storage system (ESS), cell manufacturer, and form factor [25].

SEI

When LIBs are cycled, either charging or discharging, they typically operate outside the electrochemical stability range of the electrolyte, which makes the organic electrolyte partially decrease and forms a passivating layer on the negative electrode. This layer is called the solid electrolyte interphase (SEI) [16]. SEI is key for anode-electrolyte interactions and for enhancing the lithium-ion battery lifespan [26]. Even though the SEI mostly prevents the reduction of electrolytes, an unstable SEI layer leads to further consumption of Li-ions and an increase in the impedance of the cell during the operational lifetime, which contributes to lower performance and faster degradation [16].

2.2.2 Separator

The separator is a material that lets certain particles through while excluding others. By not letting electrons travel through, the separator avoids internal short circuits in the battery. As the name implies, its purpose is to separate the electrodes from direct contact. At the same time, it must allow Li-ions to pass through so that the ions can move between the electrodes [16].

Separators are usually membranes with holes large enough for Li-ions to pass while too small for

electrode particles to pass through [27]. It is most common to use separators in LIBs that utilize mostly polyolefin-based micro-porous membranes. These membranes have good chemical stability and mechanical properties, and are economically viable [16].

2.2.3 Electrolyte

The electrolyte is a medium that electrically conducts ions between the electrodes. It consists of two main parts; a soluble salt and a polar solvent. Water, though applicable for batteries such as NiCd and NiMH, is a significant safety hazard for LIBs [28]. This is due to the intense exothermal reaction between lithium and water, where the products are lithium hydroxide ($\text{LiOH}(\text{aq})$) and highly flammable hydrogen gas ($\text{H}_2(\text{g})$).

The solvent dissolves the salt into cations and anions, which gives the electrolyte its ionic conductive properties and therefore improves the cell's performance. LIB performances are determined by combining the electrode materials, salts, and electrolyte solvents. In LIBs, the electrolyte is typically composed of lithium salts dissolved in non-aqueous organic carbonate solvents [19]. The most common salt used in LIBs is lithium hexafluorophosphate (LiPF_6), while other common salts are LiBF_4 and LiClO_4 . The solvent is usually a mixture of several solvents, such as ethylene carbonate (EC), propylene carbonate (PC), dimethyl carbonate (DMC), ethyl methyl carbonate (EMC), and diethyl carbonate (DEC) [14].

The electrolyte is a medium that interacts with all components in the cell and is therefore really important for the battery's power density, cycling stability, and safety. For an electrolyte to be considered good, it should have good ionic conductivity whilst being electronically insulating, have a wide electrochemical stability window to prevent electrolyte degradation, being inert to other components, as well as being cheap and non-toxic [16].

2.2.4 Current Collectors and Tabs

Current collectors usually made from a copper (Cu) plate and an aluminium (Al) plate, are components that bridge the electrical current generated in the LIBs with external circuits. These components greatly influence the batteries' capacity, rate capability, and long-term stability. Throughout the evolution of LIBs, the current collectors have been made thinner and thinner to increase the energy density of the batteries. Following the future evolution of LIBs, such as the semi-solid state LIB technology, current collectors have to be made flexible due to the clay-like structures of the electrodes [29]. The tabs are welded onto the current collectors making it possible to transfer the energy onto an external load.

2.2.5 Production of LIBs

Production of LIBs generally starts with creating a slurry mixture containing a binding agent, active material, a solvent, and a conductive additive (see Figure 5). The active material is usually NMC or LCO, and the conductive additive is usually carbon black. This slurry is coated onto current collectors, which for the cathode is usually aluminium and copper for the anode. Then the solvent is removed through a drying process, and the dried coated layer is compressed to a specific thickness through a calendaring machine. The layer is then cut into the desired size, and the electrodes are assembled into cells. Finally, the electrolyte is filled in a dry room with strict humidity conditions, and the cell is packaged. The cells can be packaged into different geometries such as a pouch cell, cylindrical cell, button cell, or prismatic cell [16, 30].

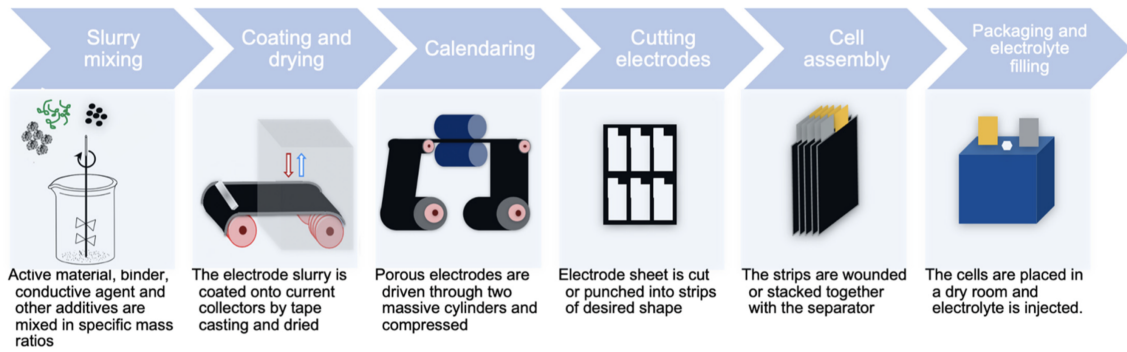


Figure 5: Production steps for a LIB. Reprinted from Bryntesen et al. [30].

As Figure 6 presents below, the energy consumption concerning the production of a LIB is largely dedicated to manufacturing of the cathodes. The energy consumption presented is per 1 Wh of cell energy. As the production volume increases, the efficiency increases with it. For the production of 1450 cells, cathode production accounts for 82 % of the energy consumption. However, even with a production volume of 50 million cells annually, cathode production still accounts for 19 % of the energy consumption. It is therefore essential to research possibilities for eliminating or streamlining such production steps [30].

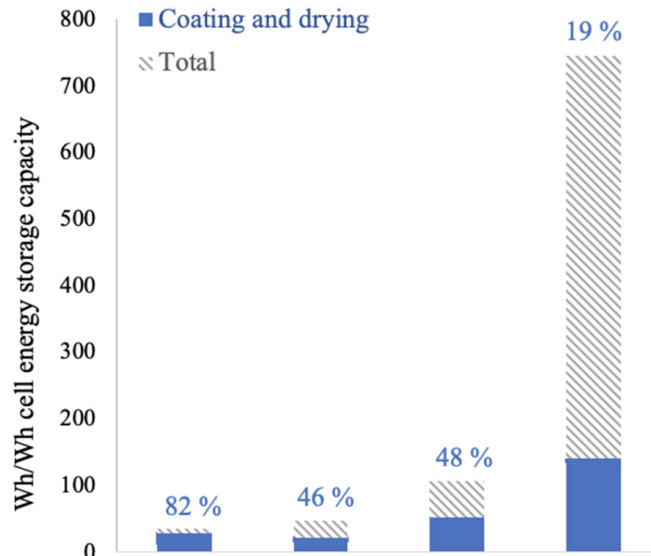


Figure 6: Energy consumption of LIB production for factories producing 1450, 146000, 1 million and 50 million cells annually, respectively. Reprinted from Bryntesen et al. [30].

2.2.6 Physical Properties of Electrodes

The physical properties of the electrode, such as loading and compression/porosity, are critical factors in determining the battery's performance and cell's characteristics.

The loading of an electrode is determined by the active mass per area to the current collector. Generally, a higher loading leads to higher specific energy. This is because a higher loading means the battery contains a higher percentage of active materials than inactive/inert materials [9].

The compression of the electrode determines the porosity. As the electrode is compressed, the porosity decreases. A porous material is a material that contains pores. An example of such a material, or rather an object, is a sponge. However, for a porous electrode, the material contains several million of these pores on a microscopic level. In a high compression, where the porosity

is decreased, the resistance to the electrons will be lower. For a lower compression, the ionic resistance is reduced [9].

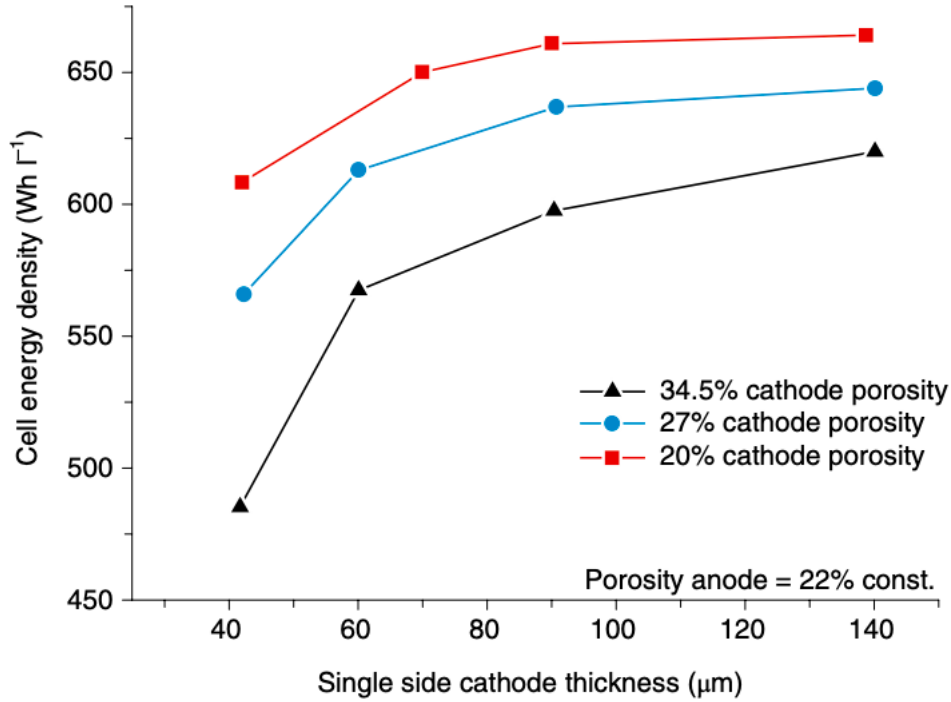


Figure 7: Cell energy density as a function of single side cathode thickness for three different cathode porosities. Reprinted from Kwade et al. [31].

Figure 7 shows the effect of single-side cathode thickness on cell energy density at three different porosities achieved by different calendering line loads. This indicates the benefits of calendering the electrodes to reduce their porosity, which improves the particles' contact and enhances the volumetric energy density. However, too much calendering causes the porosity to eventually become so low that the mechanical structure fails, and the electrodes are destroyed. [31]

Tortuosity measures the length through a porous electrode divided by the length of that electrode itself and can determine the length of the ionic pathways through the electrode. This property describes the geometric complexity of the porous electrode. It can be determined by Equation 2.5, where L' is the length of the pathway through the porous electrode, and L is the length of the electrode itself [9, 32].

$$\tau = \left(\frac{L'}{L}\right)^2 \quad (2.5)$$

Figure 8 shows a simplified sketch of a porous cathode. The white line L' represents the length of a pathway through the cathode, and L represents the length of the cathode. It should be noted that the sketch of the battery is of a semi-solid state LIB, which is presented in detail in Section 2.6.

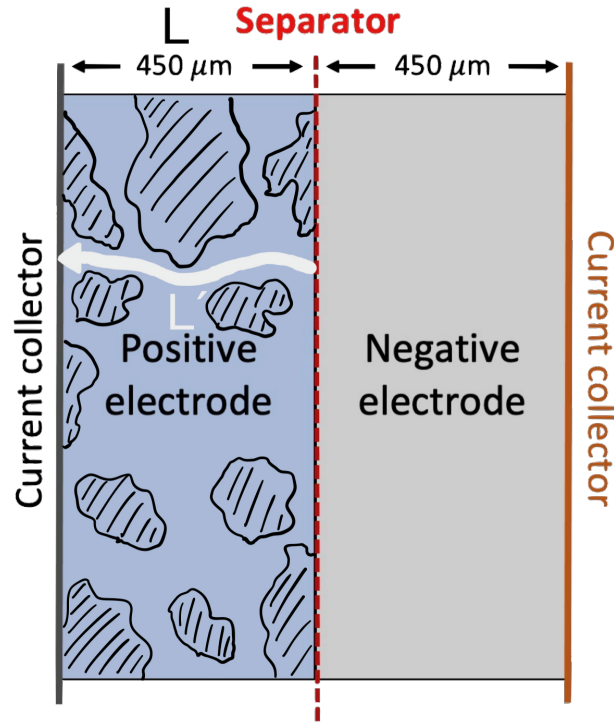


Figure 8: Simplified sketch of the pathway through a semi-solid state cathode. Edited from Bryntesen et al. [30].

2.3 General Terminology

This section presents general battery terminology used in this thesis.

2.3.1 Terminal Voltage

The terminal voltage of a battery is the voltage measured at the battery's terminals. The terminal voltage is the voltage that an external circuit can utilize. The equation for terminal voltage is displayed in Equation 2.6 below.

$$U_{Terminal} = U_{OCV} - \eta(I) \quad (2.6)$$

In this equation, $U_{Terminal}$ is the terminal voltage, U_{OCV} is the open circuit voltage, and $\eta(I)$ is the overpotential.

2.3.2 Open Circuit Voltage (OCV)

The open circuit voltage (OCV) of a battery is the terminal voltage when no polarization effects or voltage drop on the internal impedance is present [33]. This is clearly displayed in Equation 2.6.

2.3.3 Capacity

The capacity of a battery is defined as the total amount of electric charge stored within the battery due to electrochemical reactions. The electric charge is accumulated during charge and released during discharge [34].

Battery capacity is given under by Equation 2.7 below.

$$Q_e = I \cdot t \quad (2.7)$$

where Q_e is the capacity [Ah], I is the discharge current [A] and t is the discharge time [h].

2.3.4 Internal Resistance

The internal resistance (R_i) of a battery is the opposition to electric current flow within the battery. Internal resistance can be divided into two main components; *electronic resistance*, which is the resistance of the materials in the battery, as well as how these materials make contact with each other. The other is *ionic resistance*, which is the resistance due to electrochemical factors such as electrode surface area, electrolyte conductivity, and ion mobility. These ionic factors are commonly referred to as polarization effects, and they occur much slower than electronic effects [35].

Internal resistance can be expressed using Ohm's law, which is presented in Equation 2.8 below.

$$R_i [\Omega] = \frac{\Delta U [\text{V}]}{\Delta I [\text{A}]} \quad (2.8)$$

where R_i is the internal resistance, ΔU is the potential difference and ΔI is the current difference.

The internal resistance is an Ohmic resistance, meaning it follows Ohm's law. Therefore, the overpotential due to the internal resistance occurs instantaneously [36].

2.3.5 C-rate

The C-rate of a battery presents the rate at which the battery is charged or discharged [37]. C-rate is directly proportional to the current and inversely proportional to the capacity- For a given current, the C-rate can be calculated from Equation 2.9 below.

$$C\text{-rate} [\text{h}^{-1}] = \frac{\text{Current} [\text{A}]}{\text{Capacity} [\text{Ah}]} \quad (2.9)$$

For example, a fully charged 3 Ah battery with a C-rate of 1 C will be able to provide a 3 A current for 1 hour. If the given C-rate was 0.5 C or 2 C, the resulting discharged currents would be 1.5 A for 2 hours or 6 A for 30 minutes, respectively. The same principle applies during charging.

2.3.6 State of Health (SOH)

The state of health (SOH) of a battery measures the battery's current capacity compared to its original capacity. The equation for SOH is given in Equation 2.10 below.

$$SOH [\%] = \frac{\text{Current capacity} [\text{Ah}]}{\text{Original capacity} [\text{Ah}]} \cdot 100 \% \quad (2.10)$$

In order to obtain the best estimate of a battery's SOH, the battery's original and current capacity should be measured for the same C-rate and temperature since capacity is dependent on both of these factors.

2.3.7 State of Charge (SOC)

The state of charge (SOC) of a battery measures the amount of usable charge left in a cell. It is defined as the ratio of the available capacity $Q(t)$ and the maximum possible charge that can be stored in a battery Q_n [38]. SOC is given by Equation 2.11 below.

$$SOC [\%] = \frac{Q(t) [\text{Ah}]}{Q_n [\text{Ah}]} \cdot 100\% \quad (2.11)$$

2.3.8 Depth of Discharge (DOD)

The depth of discharge is a similar measure as SOC to get an overview of the battery's condition and is, in several contexts, preferred to use before SOC. DOD is defined as the amount of charge removed from the battery at the given state (Q_d) related to the total amount of charge (Q_n) that can be stored in this battery [39]. This is expressed mathematically in Equation 2.12 below.

$$DOD [\%] = \frac{\text{Removed amount of charge [Ah]}}{\text{Maximum available amount of charge [Ah]}} \cdot 100\% \quad (2.12)$$

The relationship between DOD and SOC is given in Equation 2.13:

$$DOD = 100\% - SOC \quad (2.13)$$

Ideally, a LIB should not be cycled over 60 % DOD to maintain an optimal lifespan. This means that the battery only should be charged and discharged within a SOC interval of 60 %. For example, under a DOD of 60 % around a SOC of 50 %, the cell operates within 20 - 80 % of its full capacity, which is desirable for maximizing the lifetime of a battery [40]. In other words, a larger SOC window than this leads to faster ageing of the cell [10].

2.3.9 Constant Current and Constant Voltage

A common way of charging LIBs is the constant current - constant voltage (CC-CV) method. As the name suggests, CC-CV is practiced firstly by charging the battery with a constant current. When the battery reaches a specific voltage (terminal voltage), the constant current step is finished, and the constant voltage step is initialized. During the constant voltage step, the terminal voltage is kept constant. As the battery's open circuit voltage (OCV) approaches the terminal voltage, the charging current decreases. When the current reaches the cut-off current, the charging process is concluded, and the battery is declared fully charged. The CC-CV charging process is presented in Figure 9 below [41].

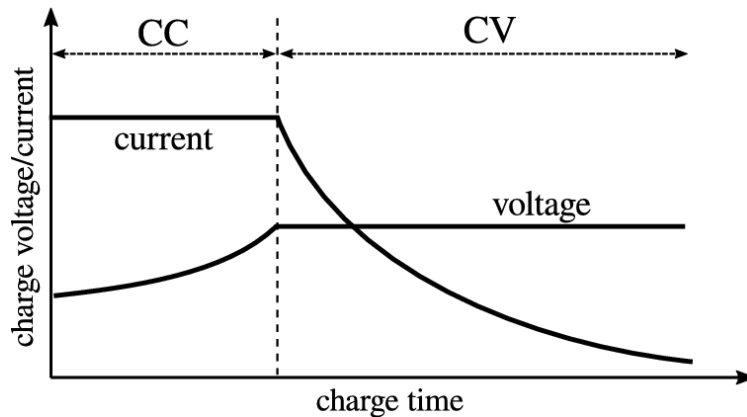


Figure 9: Standard CC-CV curve. Reprinted from Maranda [41].

2.3.10 Hybrid Pulse Power Characterization (HPPC)

An HPPC-test is a method used to determine the dynamic performance characteristics of a battery [42]. It is often used to investigate internal resistance and overpotentials and is an alternative to

electrochemical impedance spectroscopy [10].

The actual testing involves determining the battery power capability over the cell's usable voltage range by discharging and charging the cell multiple times with a constant C-rate over a given time. This provides a test profile with pulses at various SOC and, if desired, different temperatures and current loads [42]. The pulses indicate how big the voltage drops and current drops are at a given time. The magnitude of these drops or differences can then be used to calculate internal resistance from Ohm's law (Equation 2.8).

2.4 Degradation

This section will give an overview of the most common degradation mechanisms in a LIB. There are three levels of degradation: operation effects, cell-level effects, and mechanisms that initialize these effects [9].

The degradation of batteries can be dissociated into cycle ageing and calendar ageing. The terms define the ageing caused by time and the use of the batteries. Calendar ageing is an unavoidable ageing characteristic of LIBs that starts at the moment the battery is constructed. In contrast, cycle ageing is associated with usage and is impacted by charging and discharging (cycling) the LIBs [43]. Even though calendar ageing is unavoidable, there are optimal storage conditions for LIBs where this ageing mechanism can be minimized.

Electrochemical ageing initially takes place in the chemical composition of the electrolyte, but the main ageing phenomenon comes from the degradation of electrodes and can either be chemical or mechanical. The ageing process is different on the positive and negative electrodes, and the origin of the ageing mechanisms is strongly dependent on electrode composition [43].

In short, degradation leads to a change in the electrolyte's chemical composition, modification of structural properties, and loss of active material (depletion of lithium). The consequences of this are a decrease in capacity, an increase in impedance, and a loss of available peak power [43].

Generally, it can be said that if the capacity decreases below 70 %, it is considered the end of the battery's life [10].

Several factors affect the speed of the ageing processes, such as SOC, temperature, overcharging, time, short circuits [43].

2.4.1 Triggering Conditions

There are three main triggering conditions: temperature, SOC window, and C-rate/current density. These conditions affect the SOH, and impedance, both of which are presented in this section. The reduction of SOH is also referred to as capacity fade [9].

Temperature

For any given reaction, temperature (in addition to pressure and the amount of reactants present) has an impact on the rate at which it happens [44]. Temperature thus affects the chemical reaction rate of a LIB, affecting its capacity. The battery capacity increases with temperature due to this increase in chemical reaction rate. Increased capacity means that the battery can provide more energy at high temperatures [45]. However, it is well documented that temperature also has a considerable effect on the ageing of batteries. Higher temperature increases the degradation rate close to exponential growth in correlation to the temperature. This applies both for cycle and calendar ageing [9].

Temperature's impact on the battery's cycle life is presented in Figure 10 below, where the number of possible cycles decreases both with an increase and decrease in temperature from the standard operating temperature (SOT) of approximately 18 °C. The cycle curve in Figure 10 below has a

peak at approximately 18 °C, and the amount of possible cycles for the battery decreases almost exponentially as the temperature deviates from this point.

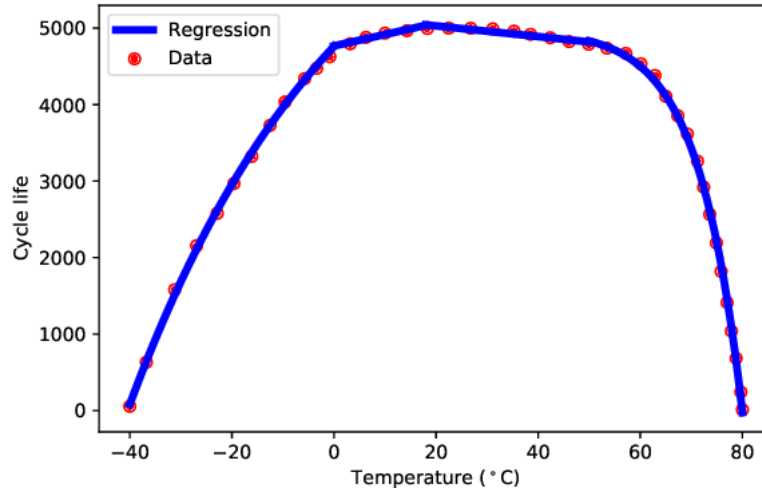


Figure 10: Effect of temperature on LIB cycle life at 50 % DOD. Reprinted from Zia et al. [45].

Higher temperatures have an impact on all three operational functions of the LIB. When the impedance increases, it harms the SOH and increases the heat generation in the battery.

Lower temperatures typically decrease a LIB's degradation rate. However, if the temperature is lower than 10 °C, this may reduce the charging capability of a LIB temporarily [9]. Low temperatures can also lead to lithium plating, which is presented in Section 2.4.2.

C-rate

The degradation rate of a LIB increases with increased current and, therefore, also with increased C-rate. Degradation occurs when Li-ions intercalate and deintercalate; this mainly occurs due to mechanical stresses from volume change [46]. Furthermore, increased C-rates lead to increased temperatures, leading to higher degradation, as stated previously.

SOC

With time, both during utilization and storage, LIBs will have a loss of active surface, which increases the negative electrode's impedance [43]. Storing or cycling LIBs with too high or low SOC impacts cycle and calendar degradation/ageing. If the SOC is too high ($\text{SOC} \gtrsim 80\%$), this will accelerate the degradation rate due to the battery being operated outside its electrochemical stability range. When this occurs, certain chemical reactions are promoted in the electrolyte [43, 9].

Another degradation mechanism due to a high SOC window is that in the extremes, the electrodes are either fully lithiated or delithiated. This results in structural stresses [9].

DOD and SOC have minimal effect on battery power fading but strongly impact the cycle life because of the mechanical stresses and side reactions they cause [45]. Thus, higher DOD results in lesser cycle life of a LIB. Figure 11 shows the relationship between a LIB's cycle life and DOD.

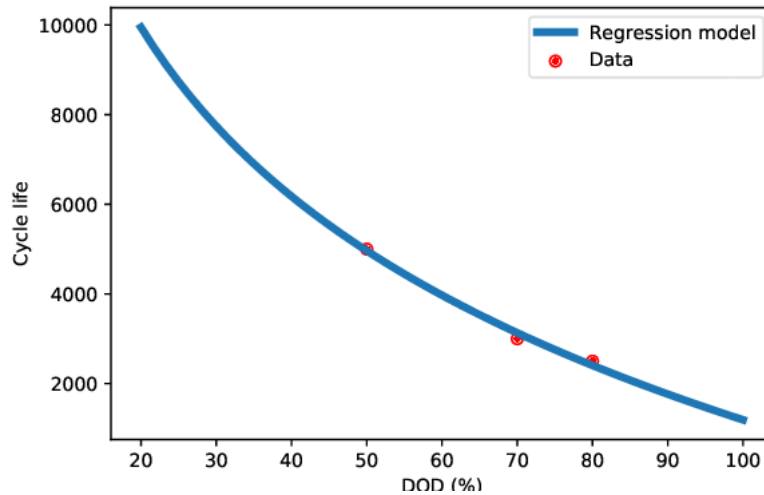


Figure 11: LIB cycle life vs DOD. Reprinted from Zia et al. [45].

Degradation Mechanisms

Above, the different factors that lead to degradation are mentioned. In this section, underlying degradation mechanisms will be introduced and put into their associated categories.

Degradation can be split into three main categories [16]:

- Increase in impedance
- Loss of active material - during cycling of the LIB, there will be some loss of the active material on the electrodes that are crucial for the intercalation processes
- Loss of lithium - loss of available Li-ions for cycling

SEI growth is often the first mechanism that occurs and contributes to the occurrence of the other mechanisms. As mentioned previously, the external triggering factors such as temperature, C-rate, and SOC-window affect how fast these degradation mechanisms develop.

2.4.2 Ageing Effects on Negative Electrode

The main ageing factor on the negative electrode, usually a graphite electrode, is the development of SEI over time [43]. Subsequent factors are the cracking of electrode particles and lithium plating.

SEI Growth

SEI is naturally created during the first charge [43]. It is a passivation film or layer that forms between the negative electrode and the electrolyte, and its role is to protect the negative electrode from possible corrosions, and the electrolyte from reductions [47]. However, the SEI is not stable as LIBs operate in tension outside the electrochemical stability range of the electrolyte, causing development of SEI over time which induces loss of Li-ions and consumption of electrolyte. This leads to increased resistance and heat generation and a decrease in capacity and power. The consumption of electrolyte could also decrease the thermal conductivity of the battery [9]. In addition, there will be a loss of Li-ions due to side reactions at the negative graphite electrode, which is reported as the primart source of calendar ageing [43].

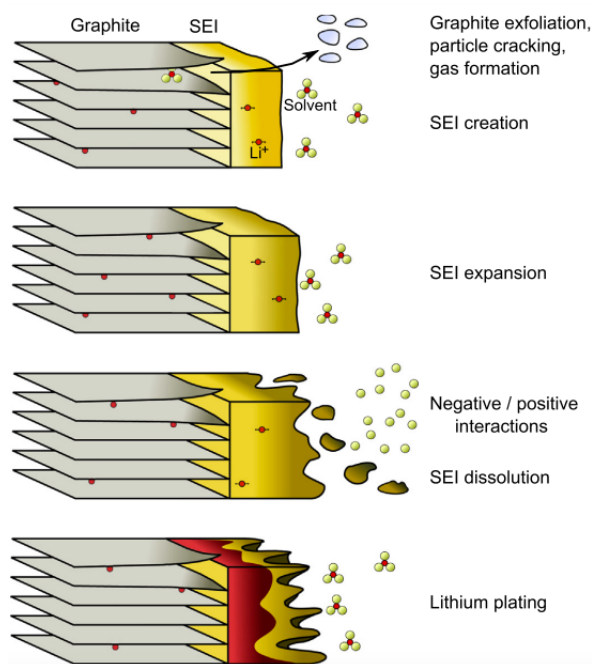


Figure 12: Illustration of unstable SEI development on the negative electrode. Reprinted from Barre et al. [43].

Figure 12 illustrates the ageing effects when there is an unstable SEI growth. With time, there is a loss of active surface, increasing the impedance in the electrode [43]. This phenomenon can occur both during utilization of the battery and during storage, so an unstable SEI affects both cycle degradation and calendar degradation.

Cracking of Electrode Particles

The SEI is permeable to Li-ions and other charged or neutral elements, causing the solvent to interact with the negative graphite electrode after diffusion through the SEI, which induces graphite exfoliation and creates gas. This gas can lead to cracking of the SEI, which allows its expansion. This gas formation can also form in the electrode pores and expand, leading to cracking of the electrode particles. However, the gas formation is relatively low and only occurs during storage with high voltage [43].

An electrode consists of millions of electrode particles that are prone to volume change during charging and discharging. Together with large SOC windows and high currents, these particles are prone to cracking [9].

As these electrode particles crack, the ions' paths to travel through get disrupted, leading to ionic and electronic conductivity loss. This conductivity loss leads to an impedance increase and a loss of power and capacity. Another consequence of cracking is that it promotes SEI growth. This, as presented above, could in the worst case lead to catastrophic failure [9]. Figure 13 displays the cracking progress of an electrode particle [48].

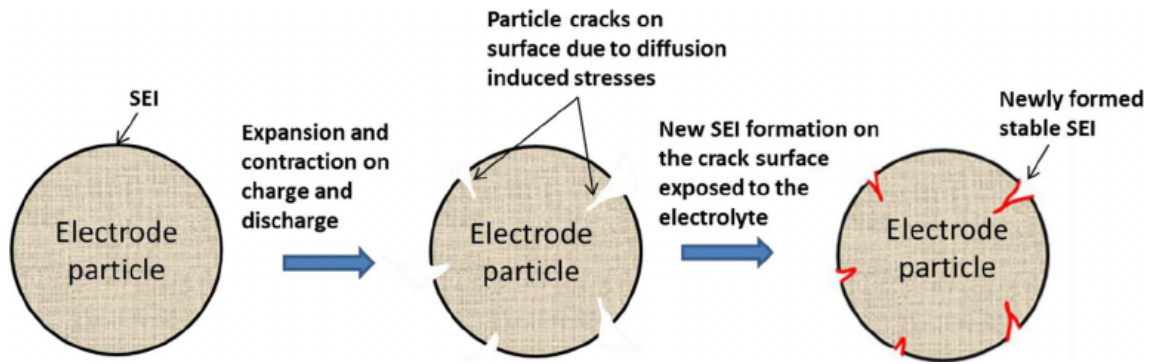


Figure 13: Cracking progress of an electrode particle. Reprinted from Xu et al. [48].

Lithium Plating

Factors such as high temperature, high SOC, overcharge, and short circuits will accelerate the loss of active surface and increase the electrode's impedance. On the contrary, low temperatures will make the Li-ions reduce into lithium metal instead of intercalating within the SEI and into the graphite electrode, which can overlay the electrode with lithium plating [9, 43]. Development of SEI and the lithium plating are responsible for the loss of cyclable Li-ions, leading to a decrease in capacity [43]. In extreme cases, lithium metal dendrites grow so large that they can puncture the separator, causing an internal short circuit and thermal runaway. Dendrite formation is presented as the "pointy" formations through the separator in Figure 14 below. Lithium plating occurs mainly during high charge C-rate when the charge rate is higher than the diffusion rate and at low temperatures. A potential window close to that where pure lithium promotes into lithium metal is the reason that lithium plating predominantly occurs on the negative electrode [9].

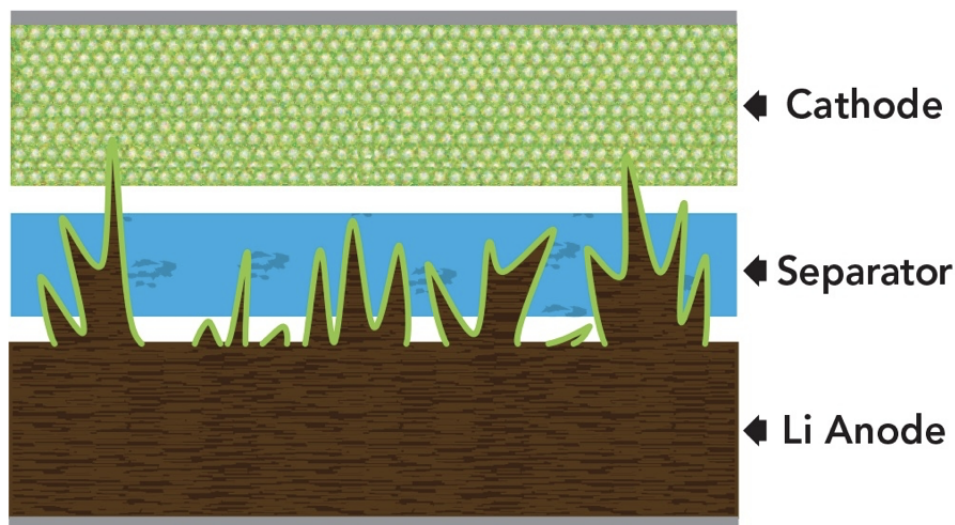


Figure 14: Dendrite formation. Reprinted from Gordon [49].

2.4.3 Ageing Effects on Positive Electrode

Research on the ageing of positive electrodes has shown that no apparent modification of the positive electrode's morphology for all battery utilization. This indicates the primordial importance of the negative electrodes in the battery ageing. SEI growth, cracking, and lithium plating have a more significant impact on the negative electrode than the positive electrode. They do not change the negative electrode's structure but rather the interphases and mechanical properties [9]. However, the positive electrode is subject to a low alteration within time, depending on the

chosen material [43]. The degradation mechanisms on the positive electrode are mainly through decomposition, and structural changes [9].

Depending on the positive electrode material, the structural changes occurring can be reversible, meaning that the structure will return to its original structure. However, if the cathode material deviates too much outside the optimal range, it can cause irreversible structure change, harming the positive electrode's functionality. In addition, some transition metals can decompose from the positive electrode and deposit on the negative electrode at high voltages [9].

There is also an SEI formation on the positive electrode, but it is more difficult to detect due to the high voltages on this electrode. In short, the observed degradation mechanisms on the positive electrode are wear of active mass, electrolyte degradation, electrolyte oxidation, and formation of an SEI, which is the interaction between positive electrode elements dissolved within the electrolyte and the negative electrode. These effects on the positive electrode are not independent, and their respective interactions differ according to the chosen positive electrode material. The negative electrode's statements highly depend on the temperature, C-rate, and SOC [43].

2.5 Thermal Properties of LIBs

This thesis aims to measure thermal properties for both semi-solid state LIBs and conventional ones and compare these with each other. The properties to be measured are thermal conductivity, specific heat capacity, internal resistance, and heat generation. All these properties follow the laws of thermodynamics and are more specifically within the first two laws. The first law of thermodynamics, conservation of energy, states that energy can change forms but neither be created nor destroyed. The second law of thermodynamics states that the entropy for an isolated system always increases [50]. These are given in Equations 2.14 and 2.15 where U [J] is the internal energy, Q [J] is heat, W [J] is work, T [K] is temperature, and S [J/K] is entropy.

$$\Delta U = Q - W \quad (2.14)$$

$$\Delta S = \frac{\Delta Q}{T} \geq 0 \quad (2.15)$$

2.5.1 Heat Generation in LIBs

LIBs are the set standard battery type for applications regarding electric vehicles due to their superior energy density and power density, and durability compared to other battery types. LIBs are a complicated electrochemical power source, and their performance is greatly affected by their operating temperatures. As the temperature decreases, the internal resistance of the battery increases as well as its available capacity decreases. This leads to shrinkage of the battery's available energy and maximum power. This means that the EV's range and performance are greatly affected by lower temperatures. The battery's temperature is not only affected by environmental factors but also by internal heat generation. For higher temperatures, the batteries are affected by safety, and aging problems [51].

There are several sources of internal heat generation in LIBs. A flow chart of the different heat sources is presented in Figure 15 below.

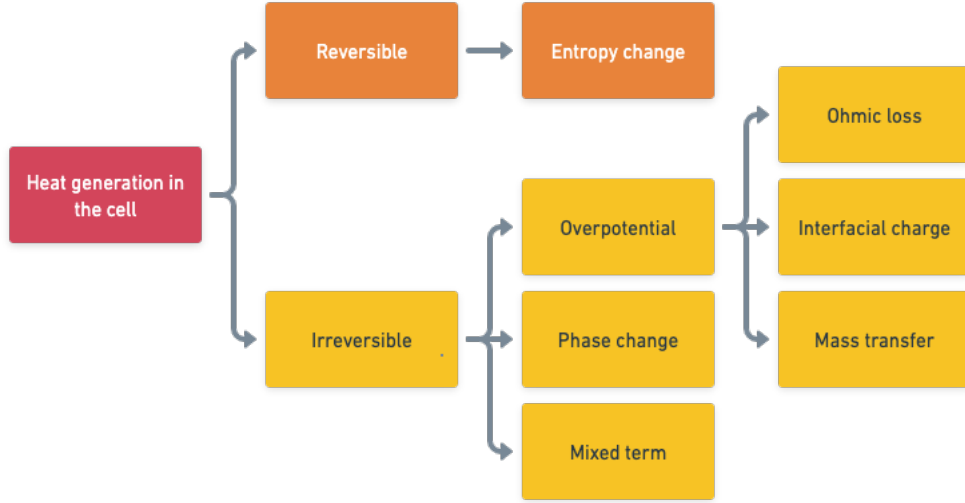


Figure 15: Illustration of the internal heat sources in LIBs [9, 52].

Several methods are applicable to measure heat generation in a LIB, for example, through an internal resistance calibration (i.e., HPPC-test). In an HPPC-test, or Hybrid Pulse Power Characterization test, the battery is charged and discharged under controlled conditions, and terminal voltage, current, and temperature measurements are monitored [53]. The internal resistance of the LIB is given in Equation 2.16, where U_{OCV} is the open circuit voltage, $U_{Terminal}$ is the terminal voltage and I is the battery operating current [51].

$$R_i = \frac{U_{OCV} - U_{Terminal}}{I} \quad (2.16)$$

Heat generation in a LIB consists of the contribution of the resistive Joule heat rate (\dot{Q}_{jou}) and the entropic or reaction heat rate (\dot{Q}_{re}), given in Equation 2.17. The Joule heat rate is determined by the battery operating current and the overpotential [51].

$$\dot{Q} = \dot{Q}_{jou} + \dot{Q}_{re} = I \cdot (U_{OCV} - U_{Terminal}) - I \cdot T \cdot \left(\frac{\partial U_{OCV}}{\partial T} \right) \quad (2.17)$$

Irreversible Heat Generation

By manipulating Equation 2.6 and Equation 2.18 for the overpotential as a function of current, I , is found.

$$\eta(I) = U_{OCV} - U_{Terminal} \quad (2.18)$$

The overpotential (η) is the cause of irreversible energy loss in the form of heat generation and can be divided into three main contributors [9, 54]:

1. **Ohmic overpotential:** This overpotential occurs when a current is drawn or applied to the cell. The ohmic overpotential is caused by the ohmic resistance in the materials of the cell, and the points of contact between these.
2. **Concentration overpotential:** Also known as diffusion overpotential, the concentration potential occurs from the resistivity created when the cell reaction is rapid, and the mass

transport is slow. It is caused by the concentration gradients of the reactants in the electrolyte and on the electrode surface.

3. **Activation overpotential:** The activation overpotential, also known as surface overpotential, is the potential required for the cell to produce current.

The sum of these overpotentials impacts the terminal voltage of the battery, following Equation 2.6. The lower the overpotential, the more efficient the battery, and thus, the less heat is generated than the extracted energy. In other terms, the efficiency of the battery, ϵ , can be expressed as shown in Equation 2.19 below.

$$\epsilon = \frac{U_{Terminal}}{U_{OCV}} = \frac{U_{OCV} - \eta}{U_{OCV}} \quad (2.19)$$

To calculate the irreversible heat generation from the internal resistance of the battery, Equation 2.20 is used [55]. In this equation, q_i [W/kg] is the specific irreversible heat generation, I [A] is the current, R_i [Ω] is the internal resistance, and m [kg] is the cell's mass.

$$q_i = \frac{I^2 \cdot R_i}{m} \quad (2.20)$$

The reversible heat generation, due to the chemical reaction within the cell, can be expressed as Equation 2.21 below [55]. In this equation, q_r [W/kg] is the specific reversible heat generation, T [K] is the temperature, ΔS [J/K] is the change in entropy, Δt [s] is the time interval, and m [kg] is the mass of the cell.

$$q_r = \frac{T \cdot \Delta S}{\Delta t \cdot m} \quad (2.21)$$

2.5.2 Thermal Conductivity

Thermal conductivity is the ability of a media to transfer heat through thermal conduction. This important thermal property has the SI units of $W \cdot m^{-1} \cdot K^{-1}$ and is typically denoted by κ , k , or λ . The higher the value of κ , the more efficient a material is at transferring heat [56].

Fourier's Law of Heat Conduction, displayed below in Equation 2.22, is an empirical equation that describes heat transfer in a solid.

$$q_x = -\kappa \cdot \frac{dT}{dx} \quad (2.22)$$

Where q_x is the heat flux in W/m^2 , κ [$W \cdot m^{-1} \cdot K^{-1}$] is the thermal conductivity of a solid, and $\frac{dT}{dx}$ is the temperature gradient in the x-direction in K/m.

2.5.3 Heat Capacity

The heat capacity is a thermodynamic ratio of the heat absorbed by a material to the change in temperature. In other words, how easy it is to change the temperature of an object by heat transfer. The heat capacity is a crucial parameter in creating a thermal model for a LIB [57]. The heat capacity is given in Equation 2.23 below, where C_p [J/K] is the heat capacity, Q [J] is the amount of heat transferred, and ΔT [K] is the temperature change. The specific heat capacity is the amount of heat needed to raise 1 kg of a material by 1 °C and can be found by dividing the heat capacity over the mass of the material [58].

$$C_p = \frac{Q}{\Delta T} \quad (2.23)$$

2.5.4 Development Trends

For the further development of LIBs there are major driving forces such as increasing the energy and power density, reducing cost, extending the lifetime, and improving on safety. To improve on energy and power density, common strategies include improving the specific and volumetric capacity of the cells. Increasing the ionic and electronic conductivity, allowing thicker electrodes, also show major potential for improving the energy and power density, as well as safety [16]. With this in mind, the semi-solid state LIB technology, containing clay-type electrodes, show potential in the development of future LIB technology.

2.6 Semi-Solid State Lithium-ion Batteries

This section introduces the semi-solid state LIB technology. It showcases the composition of the battery itself and how this technology advances energy density, reduces the relative percentage of inactive components, and has a more straightforward manufacturing process. The section also presents differences between conventional LIBs and semi-solid state LIBs [7].

2.6.1 General Composition

The semi-solid state LIB technology changes the general composition of the LIB compared to conventional ones. In these semi-solid state LIBs, the cathode includes a suspension of the active and conductive material, creating an electrode with a clay-like structure. This is done by removing the binding agent used in conventional LIBs, which may also obstruct the pore structure and increase resistance to diffusion. These semi-solid electrodes can be created much thicker than the electrodes of conventional LIBs due to the elimination of the binding agent, casting-, drying- and calendaring processes in the manufacturing of the batteries. While the electrode thickness for conventional LIBs usually varies from 50-60 μm , the thickness for the semi-solid state electrodes can vary from 250-2000 μm . The electrodes can be made thicker, leading to reduced tortuosity and higher electronic conductivity of the electrode [7]. The semi-solid state electrode includes around 60-80 wt% active material, 1-6 wt% conductive material and 20-40 wt% non-aqueous liquid electrolyte [30]. This contributes largely to the overall performance of the battery [7]. The difference in thickness is presented in Figure 16 below. The battery as a whole consists then of a cathode section and an anode section separated by a separator with current collectors on each side [30].

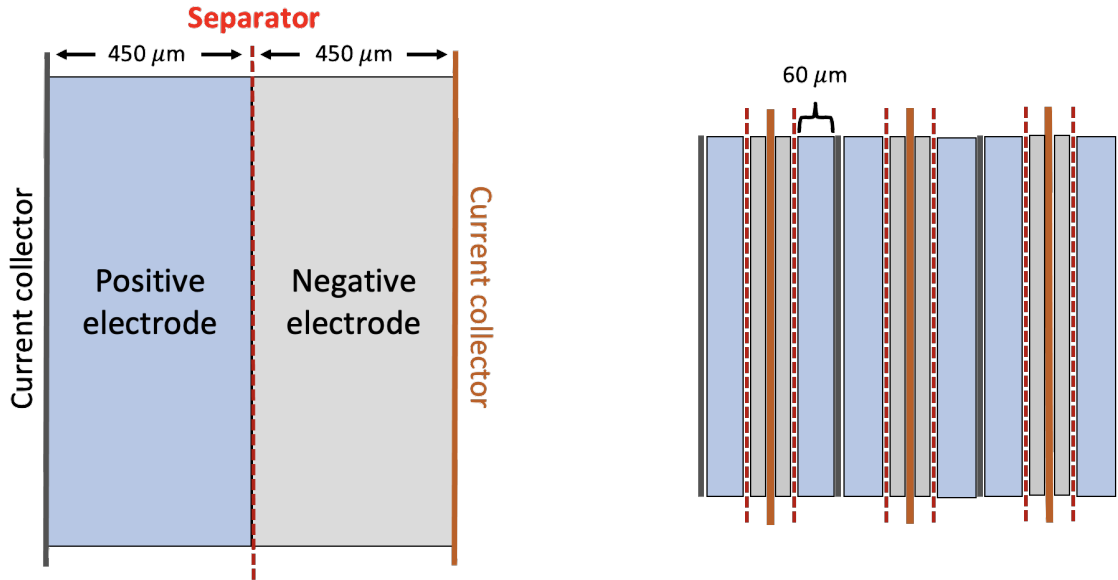


Figure 16: Differences in general composition between a semi-solid state LIB (left) and a conventional LIB (right). Reprinted from Bryntesen et al. [30].

2.6.2 Technological Advances

The semi-solid state LIB technology improves on the industry standard in several ways. This section will present the main technological advances within the categories listed below:

- Energy density
- Safety
- Production cost
- Flexibility

Energy Density

One technological advancement of the semi-solid state LIBs concerns energy density. The energy density of lithium-ion batteries has gradually increased over the years. Energy density is a function of the charge capacity [mAh/g], the volume of the electrodes [cm^3], and the ratio of active charge storing components to inactive components. Therefore, increasing the relative percentage of active components by eliminating or reducing the number of inactive components can increase the battery's energy density. For the semi-solid state LIBs, this is done by increasing the thickness of the electrodes. By eliminating the binding agent used in conventional electrodes, the volume is replaced by electrolyte, active material, and a conductive additive. The electrolyte decreases the tortuosity and increases the total salt available for ion diffusion. The active material increases the charge capacity, and the conductive additive increases the electronic conductivity. This combination results in improved rate capabilities and charge capacity [7].

Due to this increased thickness, the diffusion distance is also increased. A general consequence of thicker electrodes is higher internal resistance, which in turn results in more energy loss in form of ohmic heat generation [59]. An ideal battery has an internal resistance of 0Ω and delivers its whole voltage drop to the load. Once the internal resistance increases, more and more of the voltage drop will fall on the battery itself. This results in losses, taking the form of, for example, heat generation. In other words, decreasing internal resistance leads to higher current output.

Safety

With the electrode and electrolyte being co-suspended into a solid-liquid or semi-solid state, the safety concerning thermal runaways is drastically improved. In addition, researchers have found that the semi-solid state electrode functioned "self-healing", therefore preventing the tiny cracks that serve as the initial seeds for the dendrite caused by SEI formation leading to a reduced risk of thermal runaways [60].

As previously mentioned, the binding agent can be removed for the semi-solid state electrodes. The binding agent is typically the most toxic material used in LIBs [61]. For many LIBs today, PVDF (polyvinylidene fluoride) is used as a binder. This is a material that, under pyrolysis, releases several toxic greenhouse gases and chemical hazards such as HF and perfluorocarbons [62]. As well as the removal of the PVDF-binder, the solvent NMP (n-Methylpyrrolidone) is also removed, which is another highly toxic chemical [63].

Production Cost

As previously mentioned, the ratio of active components to inactive components has been increased, and several production steps have been eliminated. This leads to a cost reduction in the manufacturing process of the batteries. The batteries can, in other words, be produced much cheaper and simpler. Additionally, as depicted in Section 2.2.5, by removing these production steps concerning the cathode, the energy consumption is reduced significantly.

Flexibility

The semi-solid state LIB with a clay-like structure may be able to be formed into different shapes and placed where conventional batteries will not fit. One possible application for this is fitting batteries into the corners of car batteries. Another positive factor of the clay-like composition is that the batteries may be able to sustain a greater amount of external mechanical damage. Damage to conventional LIBs can negatively impact electronic performance and cause catastrophic failure. Due to the semi-solid electrode having a certain amount of "fluidity", the electrodes can sustain a significant amount of mechanical abuse by flowing around the region of the impact [64].

2.6.3 Differences in Thermal Properties

The purpose of this bachelor thesis is to measure the thermal properties of the semi-solid state LIBs and discover the differences in thermal properties between conventional and semi-solid state LIBs. The practical differences between the two is presented in Section 4.

The most significant difference between the technologies is that the electrodes are solid and the electrolyte liquid for conventional batteries, while for the semi-solid state batteries the electrode and electrolyte are co-suspended creating a clay-like composition. This means that the natural interface between the electrodes and electrolyte of the conventional cells, is removed in semi-solid state cells. This, along with the difference in thickness for the electrodes for the two LIB-types, may naturally lead to differences in thermal characteristics.

2.7 Sustainability

In current times, where sustainability has gained an increasingly large focus, it is essential to address both the challenges and possibilities of LIBs concerning sustainability.

2.7.1 Raw Material Extraction

Starting with a significant challenge, raw material extraction is a dicey subject. In order to produce a functional LIB, including the electrodes, resources such as graphite, lithium, cobalt, nickel, and manganese are typically needed in varying amounts. While lithium formerly was the point of most concern, current data points toward cobalt being the most significant challenge in terms of sustainability and availability in the long term [65]. Cobalt is mainly sourced in the Democratic Republic of the Congo, with a production of approximately 95,000 MT in 2020. This accounted for approximately 60 % of the global production [66]. In terms of cobalt extraction, Russia claims second place, with a production of about 6,300 MT in 2020, followed by Australia with 5,700 MT and the Philippines with 4,700 MT the same year [66]. By comparing the production volumes of the four largest cobalt extractors globally, it is clear how massive a contributor the Democratic Republic of the Congo is. This complicates sustainability matters severely, as the country is historically known for political instability and little transparency in its supply chains.

Such instabilities may cause rapid price changes and resource shortages. In turn, situations like this may severely impact the global production of LIBs and thus also products relying on these batteries, like EVs and portable electronics.

Thus, a long-term sustainability goal is ensuring a stable flow of cobalt, ideally with a more extensive geographic diversity. Additionally, a sustainable supply chain will require recycling of the precious resources in LIBs, as well as the development of technology less dependent or entirely independent of cobalt [65, 67].

2.7.2 Production and Use

Technological advancements toward minimizing the use of cobalt in electrode production are vital steps toward sustainable LIB production. Furthermore, increasing the performance of LIBs in areas such as energy density, power density, and lifetime has the potential to up their sustainability. Such advancements may increase the emissions in the production steps of the batteries. However, they may also greatly reduce the electricity consumption and losses during cycling over the life of the batteries [65].

2.7.3 End-of-life Management

When the "useful" lifetime of a LIB is over, there are still multiple options for reuse and recovery before they ultimately need to be disposed of.

For instance, LIBs used in EVs that have aged to a degree where they no longer can be utilized in said vehicles may still be utilized for less demanding energy storage purposes. Such purposes can for instance be utilizing the aged LIBs in fast charging stations for EVs and utilizing the batteries as a back-up power supply for the power grid. Reusing aged LIBs is the end-of-life solution that shows the greatest potential for both economic and environmental sustainability [65].

Eventually, however, all LIBs reach a point where they are deemed useless or "dead" and thus can no longer be used for energy storage. The amount of annual LIB waste was estimated to be between 200 and 500 million tons by 2020 [68]. Since LIBs contain flammable organic (separator and electrolyte) in addition to toxic substances such as cobalt, a typical landfill solution would pose a considerable threat both to human health and to the environment [68]. Furthermore, recycling valuable metals, namely cobalt, lithium, nickel, aluminium, and copper, from the dead batteries would up the sustainability of LIBs. Both by limiting waste and pollutants and also by limiting resource constraints.

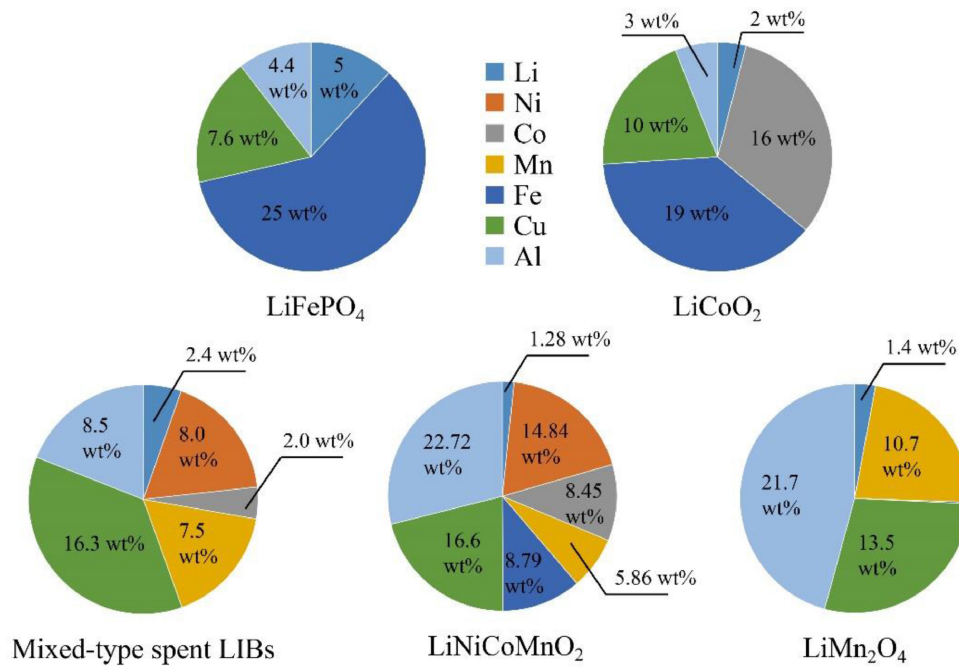


Figure 17: Valuable metals in dead LIBs by weight. Reprinted from Yang et al. [68].

Figure 17 presents the gravimetric shares of valuable metals in a handful of LIB types. Note that the atoms' atomic mass plays a large role in this distribution. Hence, even though stoichiometrically there is as much lithium as cobalt in $LiCoO_2$, Co has a wt% of 16, whereas Li has a wt% of 2.

2.7.4 Material Recovery Technologies

Current and developing material recovery technologies for LIBs are typically combinations of chemical and physical processes. The chemical processes can be categorized into hydrometallurgical, pyrometallurgical, combined pyro-hydrometallurgical, and regeneration. These processes can produce products such as metal alloys, high purity metals, and active battery materials [68].

The majority of reported recovery technologies are still at the laboratory scale, with only a few of these being applied on an industrial scale.

3 Methods

Measurements were made for the thermal properties of both the semi-solid state and conventional LIBs. The properties in question are thermal conductivity, specific heat capacity, and heat generation calculated from internal resistance. This section will present the methods used for these measurements. All six pouch cells are presented in Figure 18.

The measurements for the thermal conductivity test and the specific heat capacity test were done with the advanced measuring program LabVIEW. The internal resistance test was run with the MITS Pro software. Calculations and figures from the specific heat capacity experiment and the internal resistance experiment were done in self-made MATLAB scripts and Excel document, attached in Appendix A and D, while calculations and figures from the thermal conductivity experiment were made in an existing MATLAB script. Appendix B presents screen prints of LabVIEW's thermal conductivity and specific heat capacity program windows. Appendix C shows the MITS Pro program window for the formation and HPPC-procedure.

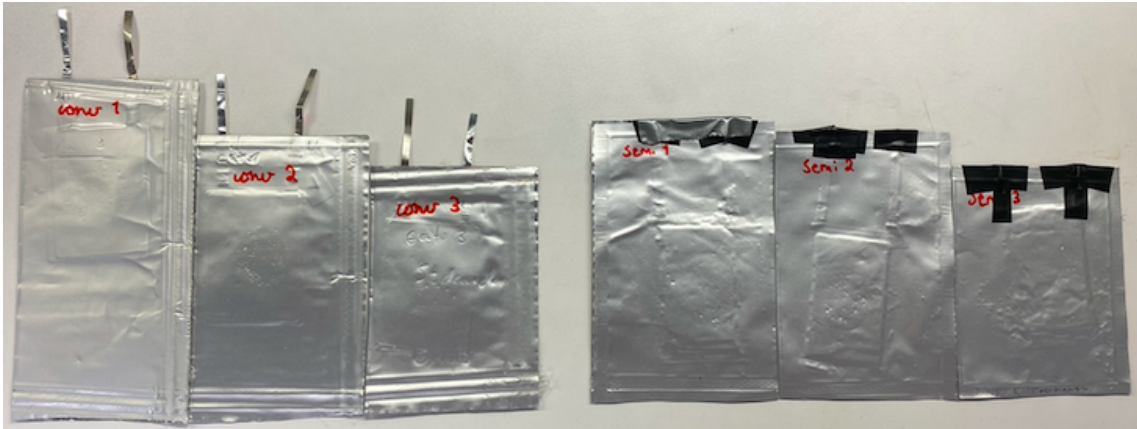


Figure 18: The three conventional LIBs to the left and the three semi-solid state LIBs to the right.

3.1 Input Data

The batteries used in the measurements are of semi-solid state and conventional LIB technologies. The measurements are meant to give insight into the differences between the technologies. For the measurements, three differently sized pouch cells were used for each technology, containing one electrode pair per cell. The active material in the conventional and the semi-solid state LIBs used in this thesis is NMC442. NMC442 consists of 40 % Ni, 40 % Mn and 20 % Co. Values supplied by the project partner for the cathode mass [g] and the capacity [mAh] for the conventional cells are given in Table 1 below. From this table, it can be observed that the cathode mass and capacity of the cells vary for the conventional cells. For the semi-solid state cells, the given capacity is 173 mAh, while the mass of these cells was not provided. The total mass of each cell was also measured using a laboratory-grade weight, presented in Section 4.3.

Table 1: Cell data provided by the industry partner

	Conventional cells			Semi-solid cells		
Cell number	1	2	3	1	2	3
NMC mass [g]	369.09	300.43	465.33	-	-	-
Capacity [mAh]	65.4	49.6	76.7	173	173	173

Using data provided by the project partner, the dimensions of the conventional and semi-solid state cells are displayed in Table 2 below. In the tables, the "From supplier" column describes the thicknesses at the production stage of the materials, and the "Measured" column represents the

measured values prior to the assembly of the cells. The thickness of the cells was also measured prior to testing with a micrometer measuring device. These values are presented in Section 4.1. The battery components are presented in the table as a cross-section of the battery, containing pouch material on both sides.

Table 2: Dimensions of the LIBs

Battery component	From supplier [μm]	Measured [μm]
Conventional cells:		
Pouch		108
Al current collector	23	20
NMC electrode		102
Separator		26
Graphite electrode		109
Cu current collector	18	18
Pouch		108
Total		491
Semi-solid state cells:		
Pouch		108
Al current collector	23	20
NMC electrode	x	-
Separator		26
Graphite electrode	y	-
Cu current collector	18	18
Pouch		108
Total		280

In Table 2, the thicknesses of the NMC electrode and the graphite electrode are marked as "x" and "y", respectively. For the sake of this project, the NMC electrode was requested to be 200 μm thick and the graphite electrode 300 μm thick, making the total thickness of these batteries 780 μm .

3.2 Thermal Property Measurements

Throughout this project, three main thermal property measurements were conducted. These were for thermal conductivity, specific heat capacity, and internal resistance. The data collected from these measurements were utilized to calculate other properties of the batteries.

3.2.1 Thermal Conductivity (κ)

In order to record data on the thermal conductivity of the batteries, a jig constructed for thermal conductivity measurements was used (see Figure 19). The electrodes used in the measurements were fresh, which means they have not yet been cycled and had no considerable ageing degradation.

Both the semi-solid state and conventional LIB samples were stacked between the steel rods of the jig, which held constant temperatures due to the constant flow of water through the inlets. By knowing the thermal conductivity value of the steel rods, the program calculated how much heat was transferred between the rods. The thermal conductivity meter measured the thickness of the samples, in addition to the temperatures at equidistant points of the sample, and the temperature drop over the sample [69]. As the thermal conductivity of the metal rods was known, the temperature difference over the samples was utilized to find their thermal conductivity. The measurements produced a graph of the thermal resistance, which is the inverse slope of the thermal conductivity [9]. The samples were stacked from one to three at different pressures to produce data with an acceptable margin of error.

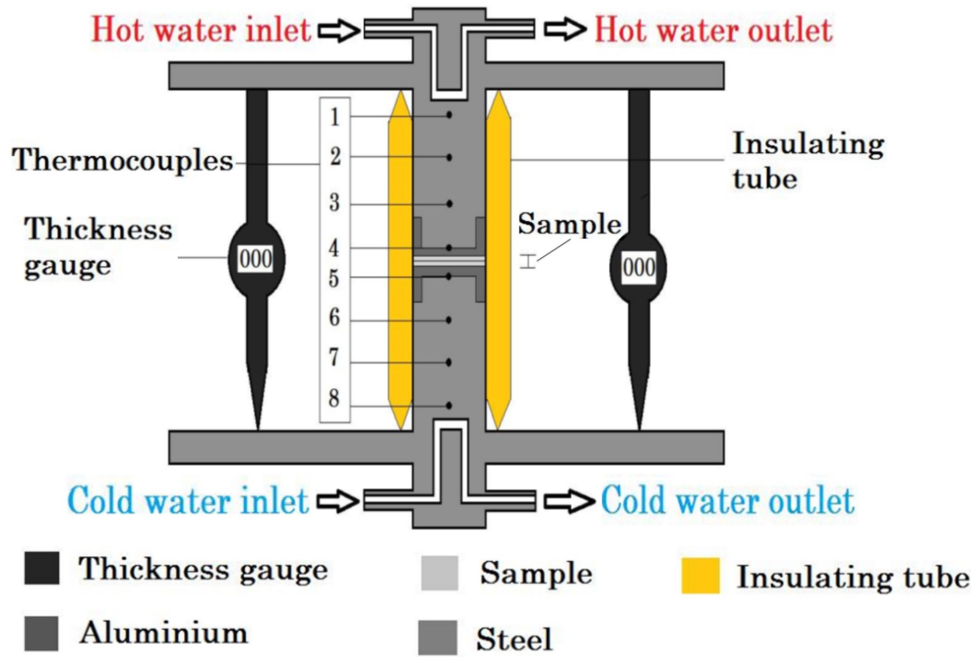
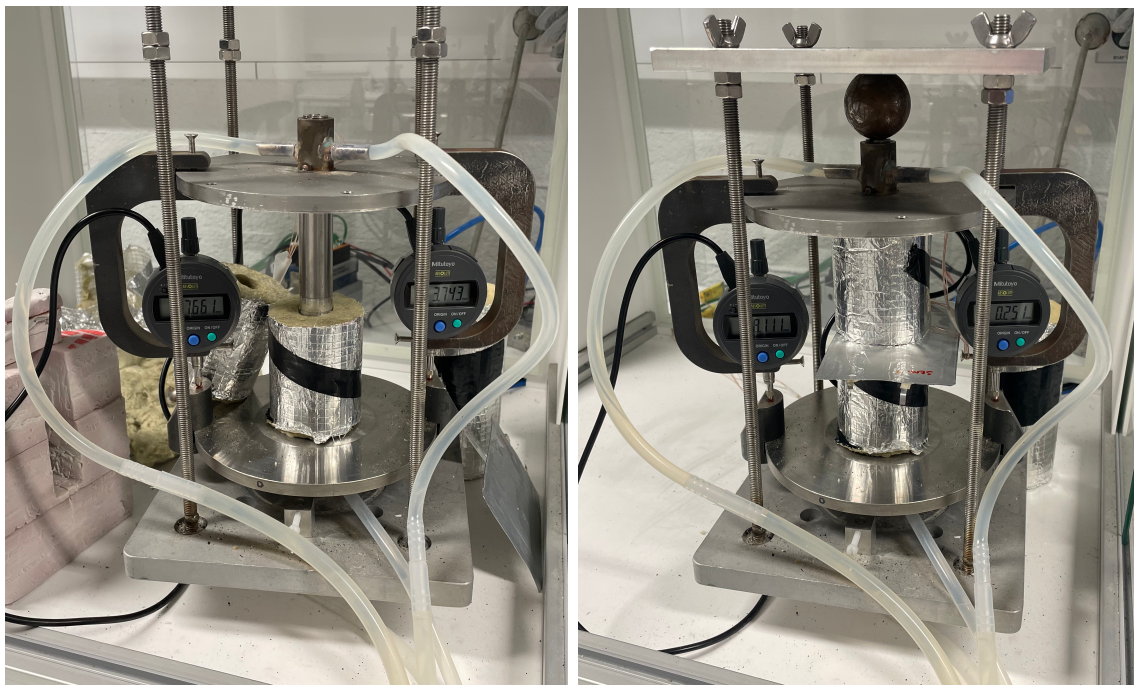


Figure 19: Schematic sketch of the thermal conductivity meter. Reprinted from Richter et al. [69].

In order to perform the measurements with minimal heat loss through the rods, an insulating tube was fitted tightly around the entire length of the rods. This tube, which had been applied in previous experiments, was divided through its centre, so the pouch cells fit inside the insulated jig. This way, the entirety of the experimental setup was adequately insulated from external impact and minimized the heat loss from the steel rods and the pouch cells. In Figure 20 the jig is presented, showing the insulation tube cut in half on the left and the setup containing a pouch cell ready for testing on the right.



(a) Jig without cells.

(b) Jig with pouch cell ready for measurement.

Figure 20: Thermal conductivity meter prepared for measurements.

To ensure minimal heat loss through the surface of the pouch cells exceeding the insulation tube, an infrared camera was used to inspect the thermal gradients on the pouch cell.

The experimental setup had the option to put significant pressure on the samples. However, since the batteries used in these experiments were pouch cells and not robust button cells, lower pressures were applied in order to avoid damaging the cells. Additionally, with the semi-solid state cells having a clay-like structure, high pressures could shift the cell's contents and possibly cause damage. Therefore, although higher pressures were deemed safe for shorter time periods, each test done for thermal conductivity was set to approximately one hour per cell.

The maximum temperature of the circulating water was set to 38 °C, and the minimum temperature was set to 10 °C. This way, the average temperature was close to room temperature. Throughout the tests, different pressures were applied to the batteries to examine the effects of this. The different pressures tested on the batteries were 2.7, 3.2, 3.5, 3.8, and 4.1 bar.

The data gathered contains two calibrations, one before the tests and one after. A file folder containing these calibrations, the tests, and an Excel file containing the thicknesses of the cells was run in a MATLAB script producing results in another Excel file. A set of buttons made of a material with known thermal conductivity was used to calibrate the program correctly. This way, the data could be adjusted to calculate the correct thermal conductivity of the pouch cells.

3.2.2 Specific Heat Capacity (c_p)

The specific heat capacity for the cell was found using an insulated water bath, where the initial temperatures of the water and the pouch cells were known. The pouch cells were placed into the water bath, and the temperature development was monitored until the temperatures reached a steady state. By applying Equation 3.1 below, the temperature differences and the known specific heat capacity of water were used to calculate the specific heat capacity of the cells. The water was enclosed by Styrofoam to insulate the heat from the surroundings. The water bath made of a Styrofoam board is presented in Figure 21 below.



Figure 21: Styrofoam insulated water bath.

To execute this measurement, a small bath containing water had to be made of XPS foam plates. The hole cut out in the Styrofoam had to be sized to contain the pouch cell stacks and water. In this case, the outline of the insulating bath was 17 cm x 8.5 cm and had a volume of 0.2 liters. 50 grams of water was used for these experiments. The floor and walls of the water bath were covered with a thin plastic layer to ensure the water stayed in the bath. Two thermocouples, which measure the temperature, were taped to the bottom of the water bath and one on the top of the cell stack to measure the temperature development. Figure 22 shows the water bath containing the two thermocouples on top of the waterproofing plastic.

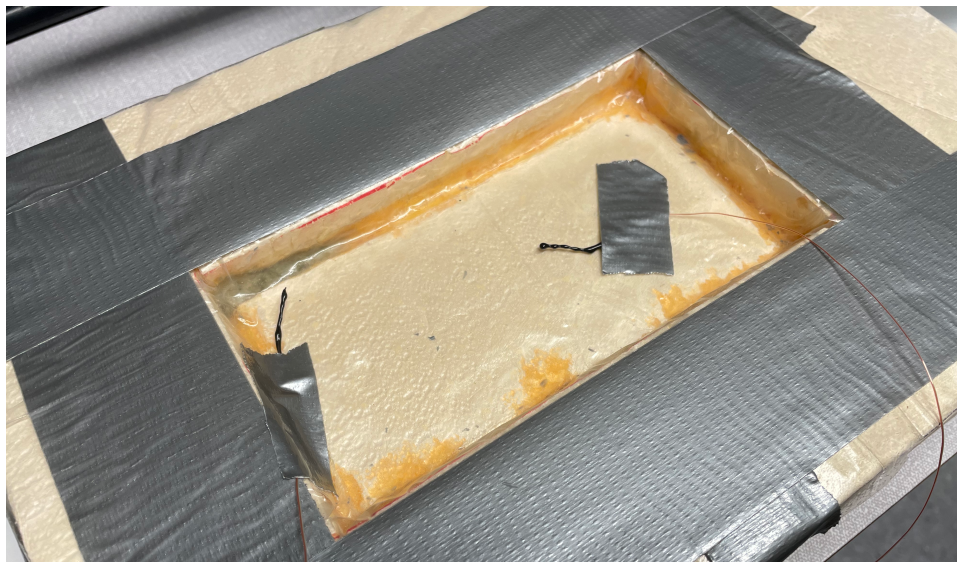


Figure 22: Styrofoam insulated water bath with two thermocouples.

The cells' tabs were sealed in insulating tape to keep them sealed from water to prevent a short circuit between the tabs of the cells.

The water for the bath was heated with a magnetic stirrer hotplate to reach a temperature of 21 °C, and the pouch cells were heated in a thermal chamber to a temperature of 45 °C. The temperature of the water and the pouch cells were measured until they reached an equilibrium temperature of room temperature, approximately 22 °C. To decrease the uncertainty, the test was repeated several times while the initial temperature of the water was adjusted until convergence was reached with the expected steady-state end temperature of 22 °C.

Because of the large difference in mass between the pouch cells and the water, the overall temperature mainly depended on the temperature of the water. To compensate for this, the cells were stacked and taped together, three conventional and three semi-solid state cells on top of each other, to increase the total mass of the cells and the degree of influence on the final temperature in the water bath. The pouch cells were also placed between two insulating Glava plates in the thermal chamber to minimize the heat loss when moving the cells from the thermal chamber to the water bath. The mass of the stacked pouch cells is presented in Table 5. Pictures of the semi-solid state stack is given in Figure 23 below.



(a) The semi-solid state stack in the thermal chamber.

(b) The semi-solid state stack with insulation in the thermal chamber.

Figure 23: Semi-solid state stack heating in the thermal chamber.

The specific heat capacity was then calculated using Equation 3.1 as presented below [9].

$$c_{p,cell} = c_{p,water} \cdot \frac{m_{water}}{m_{cell}} \cdot \frac{T_{end} - T_{water}}{T_{cell} - T_{end}} \quad (3.1)$$

where $c_{p,cell}$ is the specific heat capacity of the pouch cells, $c_{p,water}$ is specific heat capacity of water, m_{water} and m_{cell} is the mass of the water and the pouch cells, respectively, T_{end} is the steady-state end temperature for the system, and T_{water} and T_{cell} are the initial temperatures of the water and the pouch cells, respectively.

3.2.3 Heat Generation

To find the batteries' internal resistances, HPPC-tests were performed according to the procedure presented in Section 2.3.10. Prior to these tests, the batteries were placed in thermal chambers at a temperature of 35 °C, as presented in Figure 24 below, and put through a formation process. The formation process is the initial charge and discharge of a cell. During this process, the SEI is formed on the electrode [70]. As the batteries had never been charged, the SEI formation was crucial for executing the HPPC-tests.

The formation process is done by partially charging and discharging the batteries. The batteries then rested before charging them back up again for HPPC-testing. In the case of the formation process, this is a process that can go on for several days. For this project, a rapid formation cycling process was utilized. This method, proposed by Jin An et al., shortens the formation time by a factor of 6 without compromising cell performance but instead improves capacity retention [71]. This was done by having more charge-discharge cycles between 3.9-4.2 V and fewer cycles below 3.9 V. The formation process and HPPC-testing are presented in Appendix C.

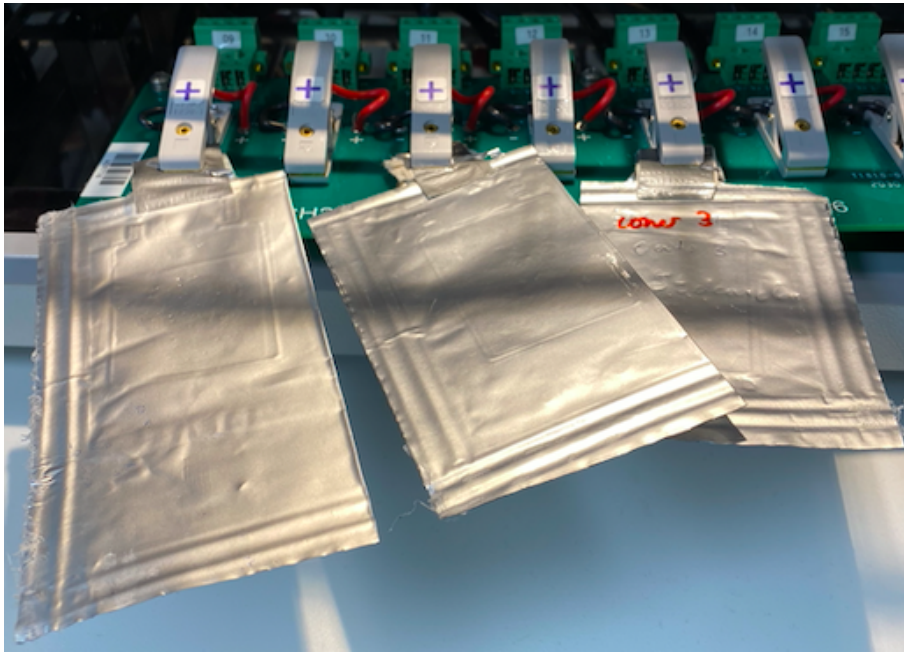


Figure 24: The three conventional pouch cells connected to the terminals in the thermal chamber, ready for testing.

After both formation and HPPC-processes, the data gathered was analyzed, and the internal resistance was found for different SOC. To establish an understanding of how the internal resistance is calculated from the data gathered, an example of an HPPC-test performed by Schweiger et al. [53] is presented in Figure 25.

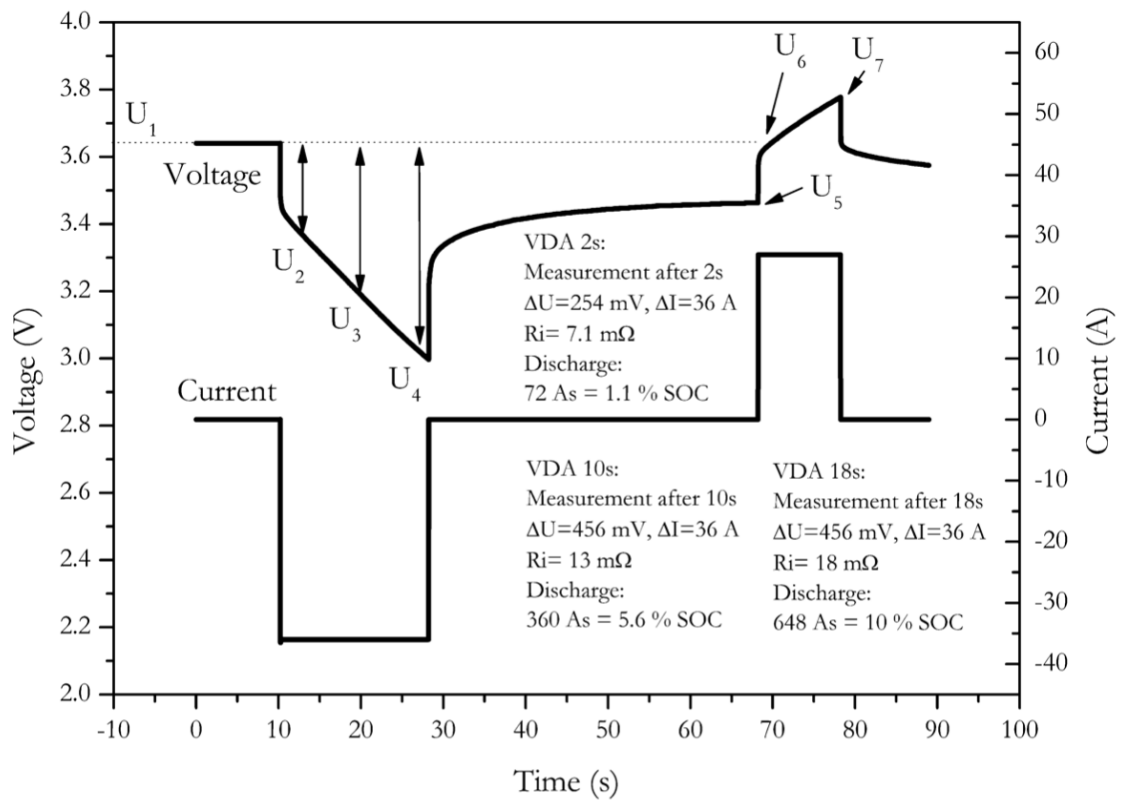


Figure 25: Example of voltage and current development in a HPPC-test. Reprinted from Schweiger et al. [72].

As presented in the middle of Figure 25, at "VDA 2s", the measurements are $\Delta U = 254$ mV and $\Delta I = 36$ A. To calculate the internal resistance at this stage, the voltage drop from U_1 and U_2 is divided by the drop in current, as shown in Equation 3.2 below. This equals the calculated value of $R_i = 7.1$ m Ω , as presented in the figure.

$$R_{i_{discharge,2s}} = \left| \frac{U_1 - U_2}{I_{discharge}} \right| \quad (3.2)$$

A more general expression is presented in Equation 3.3 below.

$$R_i = \left| \frac{\Delta U_0}{\Delta I_0} \right| = \left| \frac{U_{0s} - U_{xs}}{I_{0s} - I_{xs}} \right| \quad (3.3)$$

The absolute value sign compensates for the discharge pulse's negative value for the internal resistance. The variables in the fraction indicate when the values are retrieved. The interval "0s" to "xs" means the values at $t = 0$ seconds and $t = x$ seconds.

A similar method was used for both conventional cell 2 and 3 for different SOC, taking an interval of voltages and dividing them by the current. This method was applied for the calculations of internal resistance. However, as mentioned in Section 2.3.4, the overpotential due to internal resistance occurs instantaneously. Therefore, the internal resistance was calculated for a significantly shorter time period, than what was presented in the example above. Finally, the specific irreversible heat generation of the battery was calculated using Equation 2.20. For the mass variable in the equation, the mass of the entire pouch cell was used.

3.3 Thermal Imaging

A thermal camera was used to visualize how heat dissipated throughout the pouch cells. The camera model used in the experiment was a Xenics Gobi-640-GigE, shown in Figure 26 below.



Figure 26: Thermal camera.

To optimize the camera's ability to capture heat dissipation, one cell of each battery type was coated with matte black spray paint to minimize the reflectivity of the pouches. When used to view/measure heat on reflective surfaces, the camera will capture the objects that are reflected on the surface instead of the surface's actual heat signature. For instance, when trying to capture the heat dissipation in a mirror, one would instead see one's own heat signature being reflected back at the camera.

After spraying and drying the pouch cells, they were placed in the thermal conductivity test chamber with the insulation tube surrounding the steel rods. The intent of placing the pouch cells together with the insulation was to observe if any heat dissipated beyond the insulated region. After applying a pressure of 11.6 bar, the heat camera was calibrated, and photos were taken. Although this pressure was significantly higher than during the thermal conductivity tests, the time period for these tests was significantly shorter. The cells were also placed between the steel rods without the insulation to gain a clearer view of the measuring area.

For the final observation, a small beaker was filled with hot water and placed upon the cells. This was to observe the heat dissipation for a much higher temperature than the temperatures applied in the thermal conductivity chamber.

4 Results

This section will present the results gathered from all thermal property experiments described in Section 3. In particular, measurements were made for thermal conductivity, specific heat capacity, and irreversible heat generation due to internal resistance.

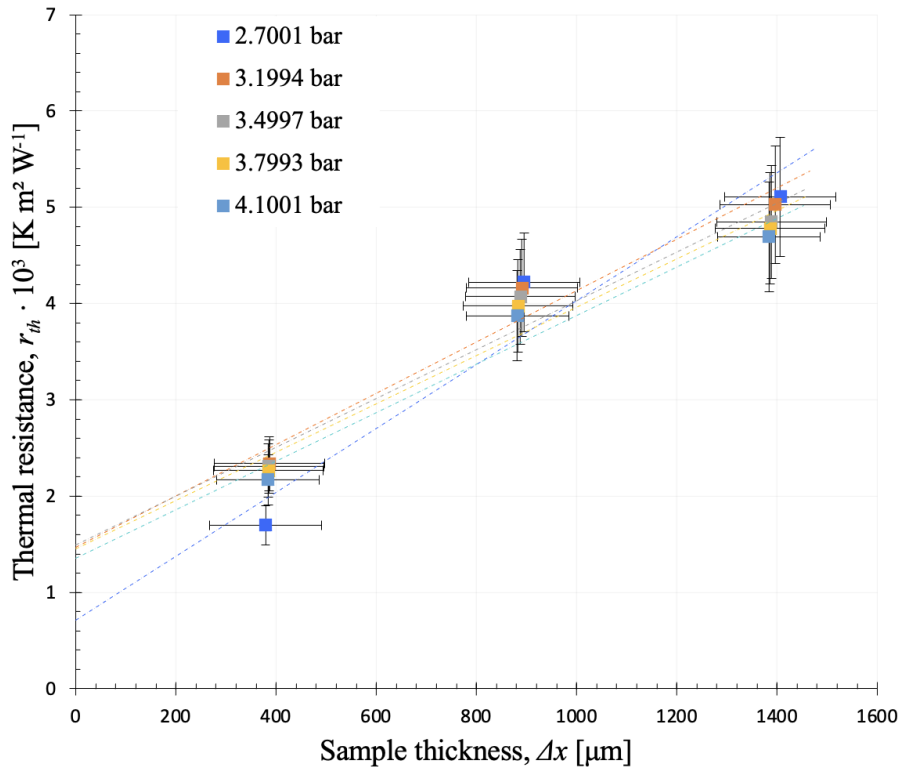
4.1 Thermal Conductivity Test Results

For the thermal conductivity measurements, the cells of both technologies were stacked from one to three cells. The thickness of each cell was measured at three different points on each cell before the tests. These measurements are presented in Table 3 below.

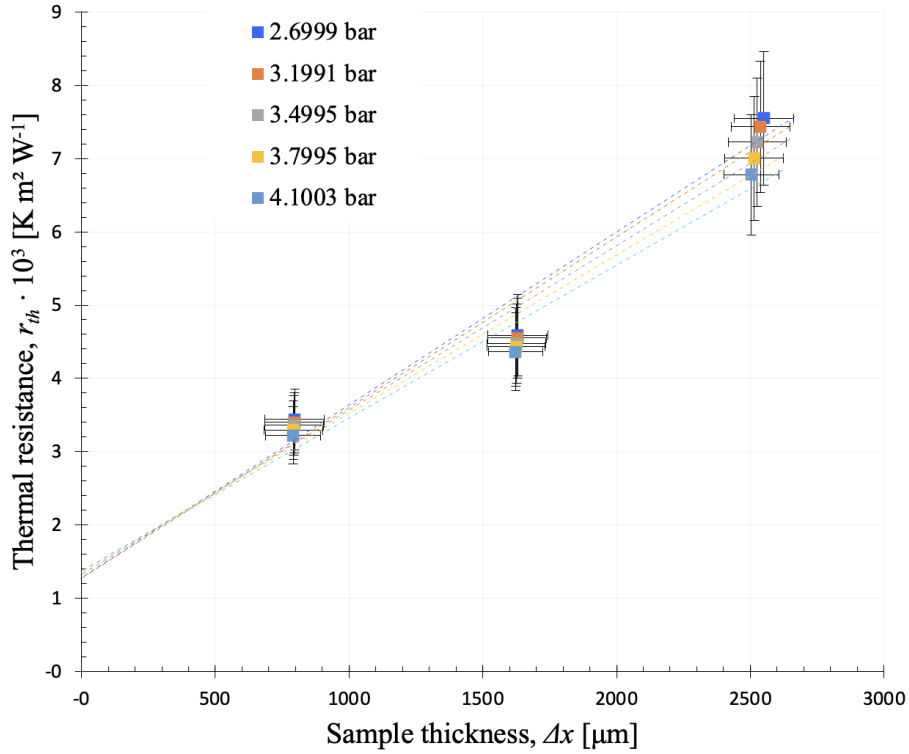
Table 3: Cell sample thicknesses for both technologies

Measurements	Conventional cells [mm]			Semi-solid cells [mm]		
Sample number	1	2	3	1	2	3
dx 1	0.432	0.479	0.480	0.828	0.841	0.816
dx 2	0.435	0.494	0.479	0.799	0.784	0.790
dx 3	0.434	0.485	0.480	0.819	0.760	0.776
dx mean $\pm 2 \cdot st.dev$	0.43 ± 0.0	0.49 ± 0.02	0.48 ± 0.0	0.82 ± 0.03	0.80 ± 0.08	0.79 ± 0.04

When stacked from one sample to three, the thermal resistance (r_{th}) will increase because the heat has to travel through more material. As presented in Figure 27, the thermal resistance increases with increasing sample thickness (Δx) for all pressures put on the batteries. Note that the total sample thickness for the semi-solid state LIBs shown in Figure 27b is thicker than for the conventional in Figure 27a. The thermal resistance is also slightly higher for the semi-solid state LIBs.



(a) Thermal resistance as a function of sample thickness for the conventional cells.



(b) Thermal resistance as a function of sample thickness for the semi-solid state cells.

Figure 27: Thermal resistance (r_{th}) as a function of sample thickness (Δx) for both technologies.

From this, the thermal conductivity of the semi-solid state LIBs and conventional LIBs was calculated. The results presented in Table 4 below include the thermal conductivity (κ) and the standard deviation.

Table 4: Thermal conductivity for both technologies at different pressures

Pressure [bar]	Conventional LIB [W/m·K]	Semi-solid State LIB [W/m·K]
2.7	0.3011 ± 0.165	0.4240 ± 0.190
3.2	0.3755 ± 0.155	0.4293 ± 0.190
3.5	0.3946 ± 0.176	0.4458 ± 0.196
3.8	0.3986 ± 0.168	0.4625 ± 0.187
4.1	0.3965 ± 0.163	0.4795 ± 0.181

The thermal conductivity for the semi-solid state LIBs was generally higher than for the conventional LIBs, with the standard deviation being significant for all measurements. Although the deviations are significant, the results show a clear difference in thermal conductivity between the conventional and semi-solid state technology. The results from the thermal conductivity tests are also presented in Figure 28 below, with error bars for the standard deviation.

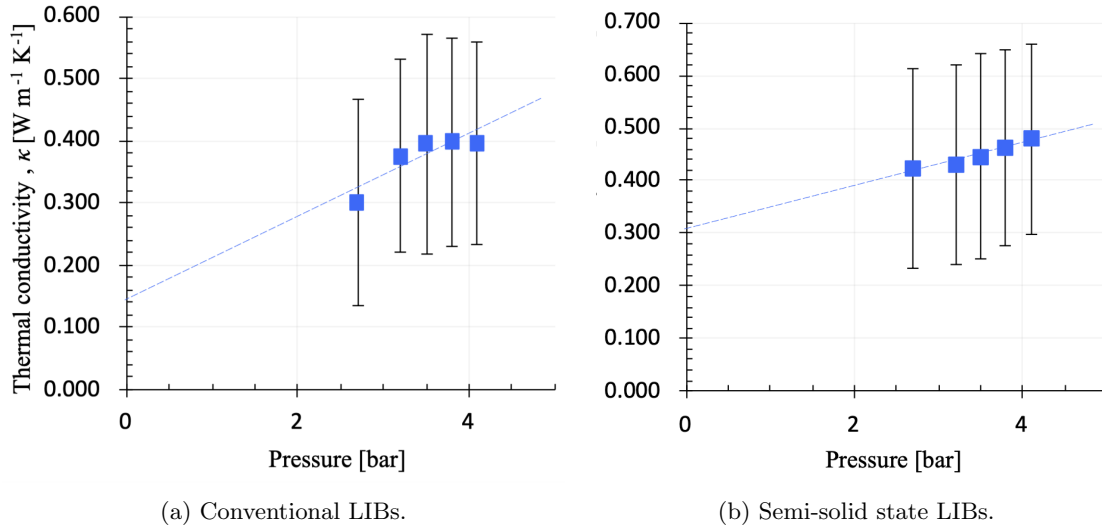


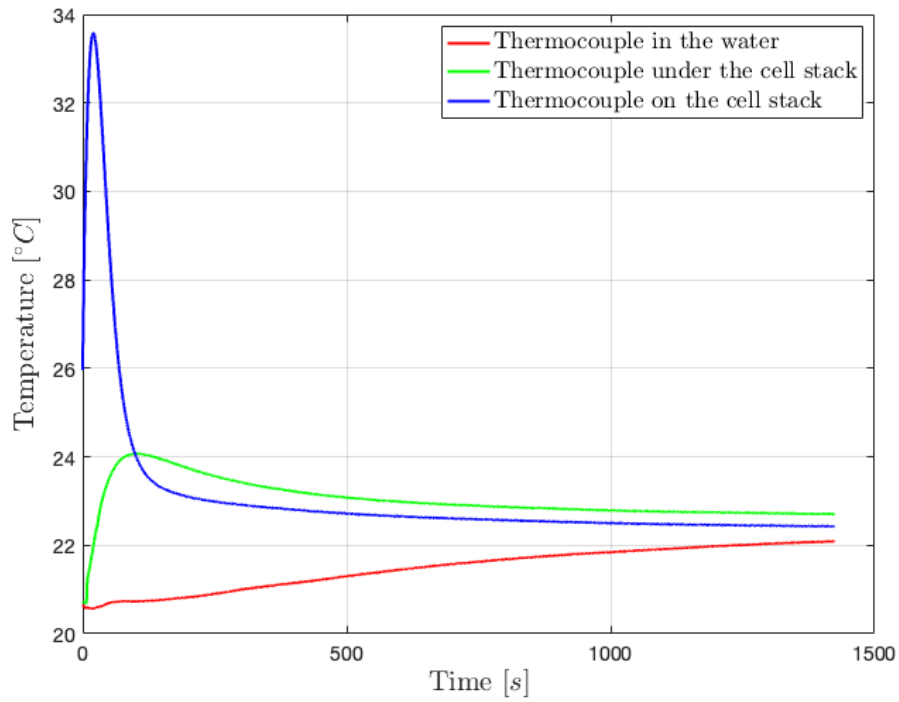
Figure 28: Thermal conductivity as a function of pressure.

4.2 Specific Heat Capacity Test Results

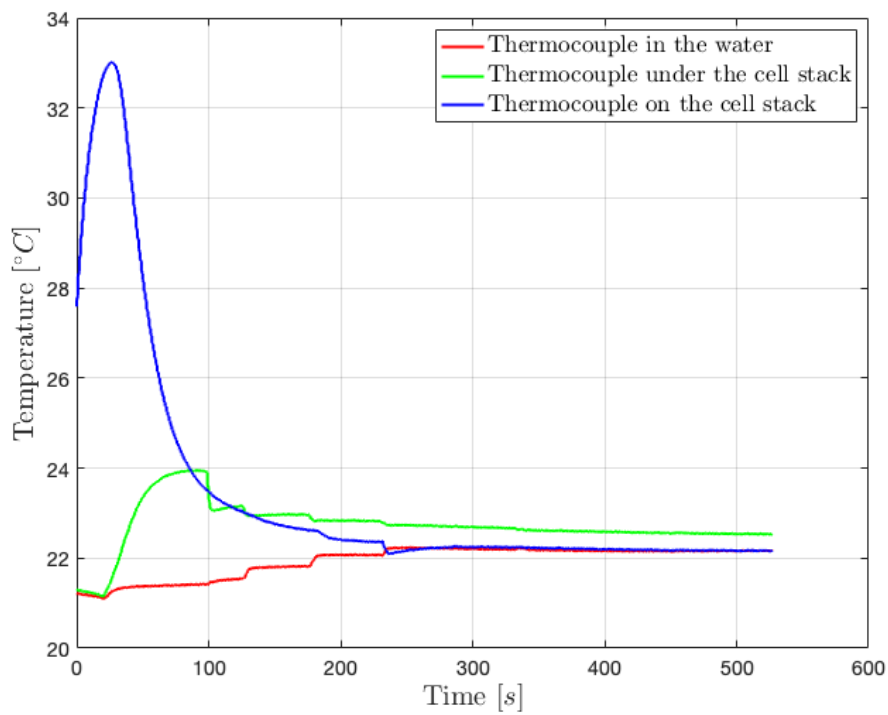
The specific heat capacity tests were performed for stacked units of the three conventional LIBs and the three semi-solid state LIBs. Both stacks of pouch cells were tested under the same conditions, and the results from the tests are presented in Figure 29 and Table 5 below.

As the stack was removed from the thermal chamber set to 45 °C, the thermocouple fastened to the stack measured 34 °C prior to the stack being placed in the water bath. As a result, this temperature was used to calculate specific heat capacity.

There was a slight delay in the stream of information from the thermocouples to the software. Therefore, it took some time from when the test started until the thermocouples measured the correct temperature. This can be observed from Figure 29 below, where the thermocouple on the cell stack takes some time to reach the maximum temperature before the temperature eventually drops when the battery gets submerged in the water bath.



(a) Temperature over time for the semi-solid state stack.



(b) Temperature over time for the conventional stack.

Figure 29: Results from the heat capacity test. Three thermocouples measuring the temperature of three different spots in the insulated water bath. The initial temperature raise of the green curve is because this thermocouple lies on the bottom of the water bath directly under the cell stack.

As seen in Figure 29a, the end temperatures do not fully converge. This is due to the thermocouples not being equally calibrated, resulting in a slight deviation. However, they converge toward a constant temperature of approximately 22.4 °C (room temperature) after approximately 1500 seconds. This is considered the steady-state end temperature. If the test was run for a longer time period, the temperatures would theoretically move closer to each other and minimize the deviation.

In Figure 29b, the temperatures are converging towards a steady-state end temperature of around 22.4 °C after approximately 600 seconds.

In Table 5 below, the results from both tests are presented.

Table 5: Measured and calculated values from the specific heat capacity test for both stacks

Variable	Value	Unit
$c_{p,water}$	4186	$\text{J}\cdot\text{kg}^{-1}\cdot\text{K}^{-1}$
m_{water}	50	g
m_{stack}	19.3	g
T_{water}	20.7	°C
T_{stack}	33.6	°C
T_{end}	22.4	°C
$c_{p,stack}$	1646.05	$\text{J}\cdot\text{kg}^{-1}\cdot\text{K}^{-1}$

(a) Semi-solid state stack.

Variable	Value	Unit
$c_{p,water}$	4186	$\text{J}\cdot\text{kg}^{-1}\cdot\text{K}^{-1}$
m_{water}	50	kg
m_{stack}	17	kg
T_{water}	21.25	°C
T_{stack}	33.02	°C
T_{end}	22.29	°C
$c_{p,stack}$	1193.31	$\text{J}\cdot\text{kg}^{-1}\cdot\text{K}^{-1}$

(b) Conventional stack.

* $c_{p,water}$ is a tabulated value, $c_{p,stack}$ is calculated from Equation 2.23 and the remaining values are measured during the test.

The test was run for two stacks with three pouch cells each, one stack with conventional pouch cells, and one with semi-solid state pouch cells. Since the specific heat capacity measures per unit of mass, the stack c_p -value is the same as per unit cell. Additionally, the tests for both the semi-solid state and the conventional stack were performed under the same conditions. Therefore the calculations for specific heat capacities have the same basis. The average specific heat capacities for the semi-solid state cells and the conventional cells are:

$$c_{p,cell,semi-solid} = 1646.05 \frac{\text{J}}{\text{kg}\cdot\text{K}} \quad \text{and} \quad c_{p,cell,conv} = 1193.31 \frac{\text{J}}{\text{kg}\cdot\text{K}}$$

4.3 Heat Generation Test Results

The formation process and HPPC-tests resulted in 2/3 conventional cells and none of the semi-solid cells producing results. One of the conventional cells (conventional cell number 1) was not able to be tested due to a broken current collector. Semi-solid cell number 2 and 3 had broken tabs and, therefore, an infinitely high internal resistance. Semi-solid cell number 1 contained a functional set of tabs but showed no increase in voltage during charging and therefore produced no results due to a suspected internal short circuit. Therefore, this section presents results for the two conventional cells that produced results.

To calculate the irreversible heat generation from the internal resistance of the cells, Equation 2.20 was used. For this equation, the cells' masses were measured. These are presented in Table 6 below.

Table 6: Total mass of each cell

Conventional cells [g]			Semi-solid cells [g]		
Sample 1	Sample 2	Sample 3	Sample 1	Sample 2	Sample 3
4.964	4.415	4.212	5.318	5.081	4.604

Figure 30 shows the entire process, including formation and HPPC-tests with the voltage applied

on the left y-axis, the current applied on the right y-axis, and elapsed time on the x-axis. The formation process started at approximately 3.8 hours and can be characterized as the sudden charging and discharging of the cell by applying and drawing current. The cell then rested from approximately 5.7 hours until the first HPPC-test started at approximately 8.5 hours.

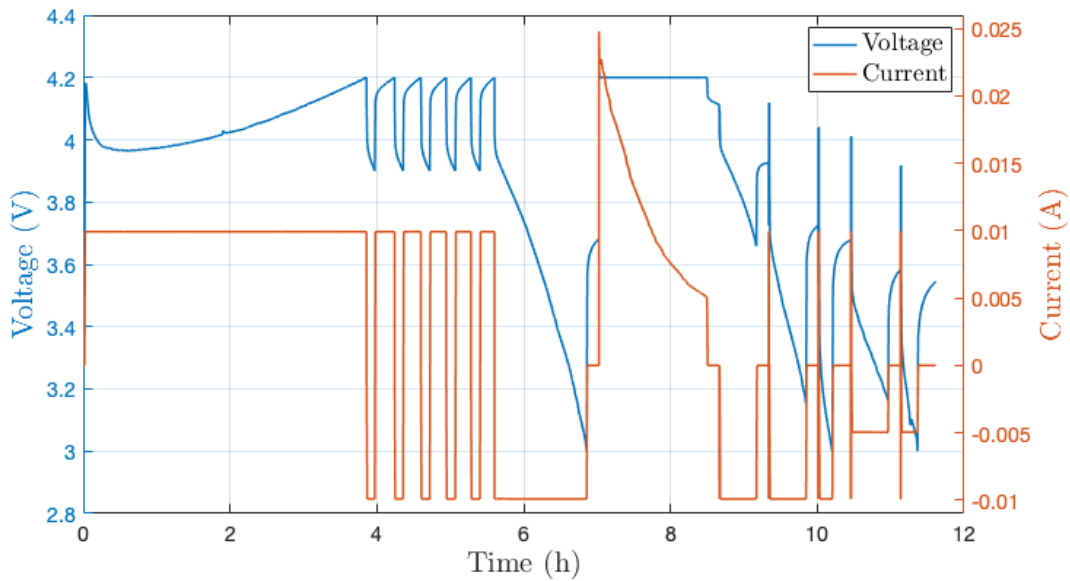


Figure 30: Voltage and current as a function of time. This is the plot for conventional pouch cell number two for the whole cycling test. The voltage is slowly brought up to 4.2 V, where the formation process starts. Here, the battery slowly gets charged and discharged between 3.9-4.2 V. The HPPC-tests can be viewed from approximately 8.5 hours.

The formation process for the conventional pouch cell number 2 is presented in Figure 31 below, showing the cell being charged and discharged. An observation made during this process is that the time of which the constant current is applied during charging decreases for each interval and is longer than the periods of constant current during discharging.

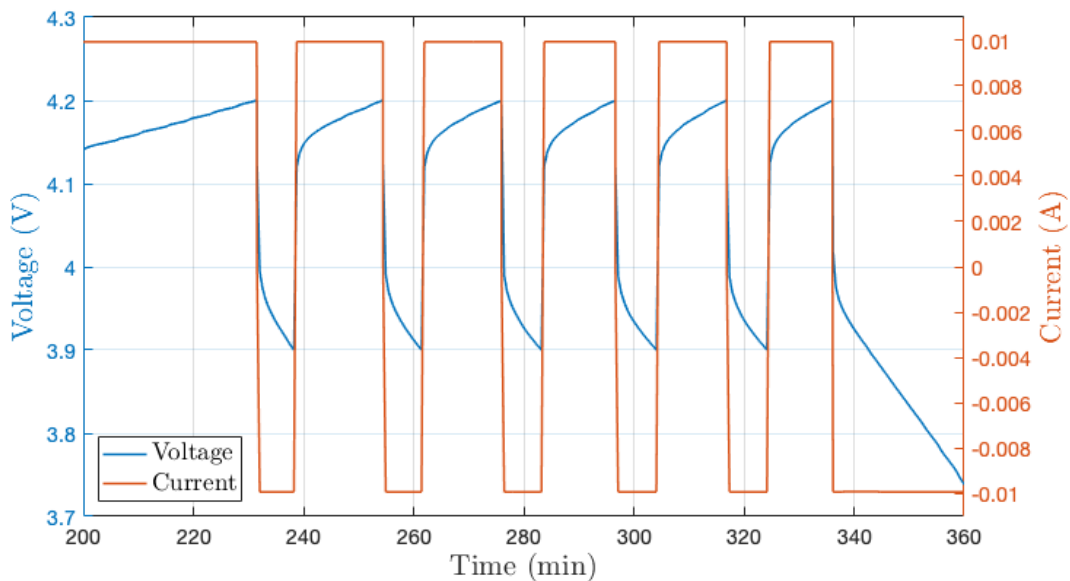


Figure 31: Voltage and current as a function of time during the formation.

A clear overview of the whole HPPC-process for conventional cell number 2 is presented in Figure 32, showing all five HPPC-tests zoomed out. All HPPC-tests are marked with the battery's respective SOC. The current graph on the lower half of the figure also shows where the CV (constant voltage) ends, as well as the different discharge currents.

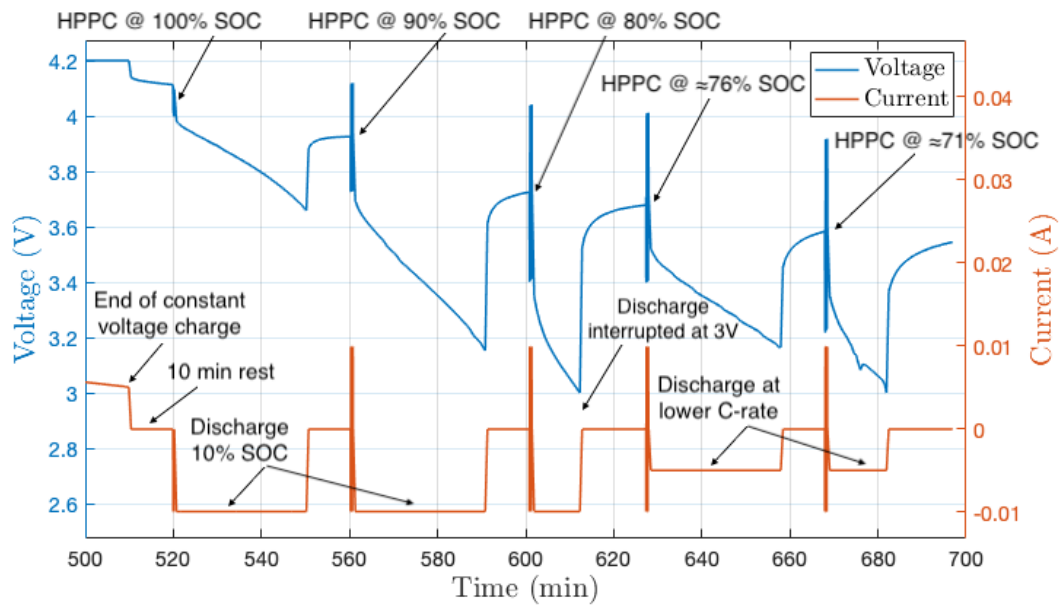


Figure 32: Voltage and current as a function of time during all five HPPC-tests. The different HPPC-tests are marked with their corresponding SOC, as well as explanations to different stages of the current curve.

A more representative picture of the second HPPC-test, at 90 % SOC, is presented in Figure 33 below.

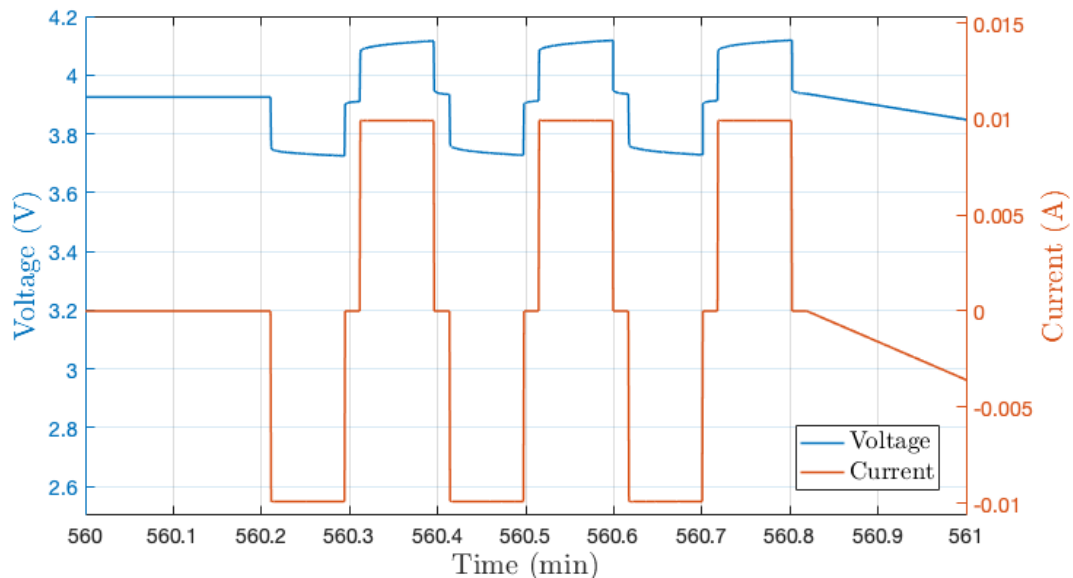


Figure 33: Voltage and current against time during the HPPC-test at 90 % SOC for conventional cell 2.

Figure 34 is a zoomed-in projection of Figure 33. It makes it easier to analyze the information of the first pulses. The relevant voltage drops used for the internal resistance calculations are marked

in the figure as, e.g., U_1 and U_2 . Associated current drops are not marked but coincide with the marked voltage drops.

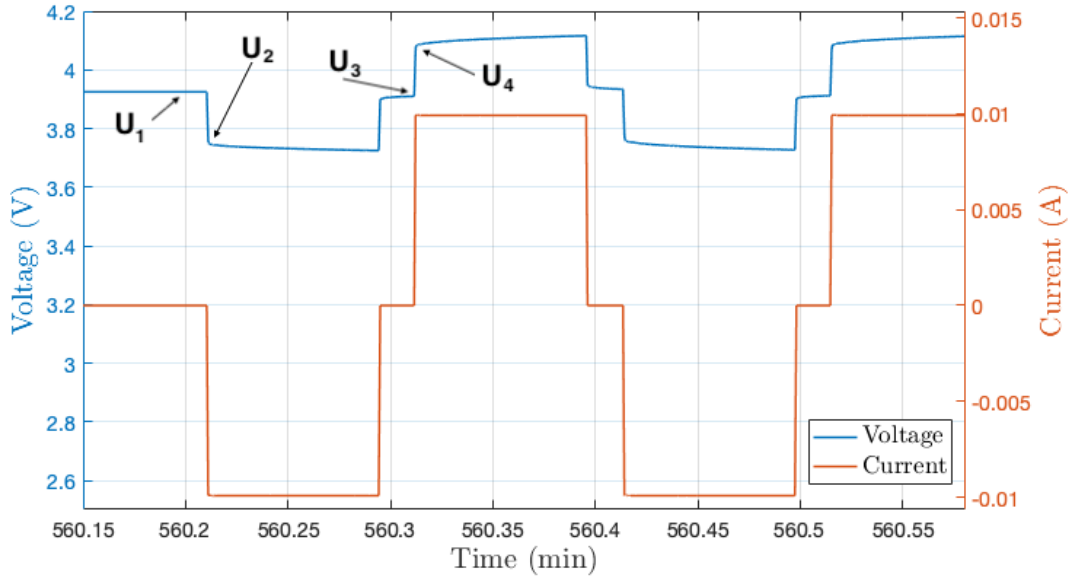


Figure 34: Voltage and current against time during the HPPC-test at 90 % SOC for conventional cell 2, zoomed in at the first pulses.

The values used for the calculation of internal resistance for this cell at 90 % SOC are presented in Table 7 below.

Table 7: Values for voltage and current used in internal resistance calculation

Value	Voltage [V]	Current [A]
U_1	3.93	0
U_2	3.75	-0.01
U_3	3.91	0
U_4	4.08	0.01

Table 8 presents the results gathered from the HPPC-tests performed on conventional cell number 2. The results include both the internal resistance for charging and discharging and the irreversible heat generation. The values used for the calculations of internal resistance as well as irreversible heat generation for both cells are given in Appendix D.1.

Table 8: Internal resistance and irreversible heat generation for conventional cell 2 for all HPPC-tests performed at different SOC

SOC	Discharge		Charge	
	Internal resistance (R_i)	Irreversible heat generation (q_i)	Internal resistance (R_i)	Irreversible heat generation (q_i)
100 %	9 Ω	0.20 W/kg	9 Ω	0.20 W/kg
90 %	18 Ω	0.41 W/kg	17 Ω	0.39 W/kg
80 %	28 Ω	0.63 W/kg	27 Ω	0.61 W/kg
76 %	27 Ω	0.61 W/kg	28 Ω	0.63 W/kg
71 %	30 Ω	0.68 W/kg	29 Ω	0.66 W/kg

For conventional cell number 3, relevant data plots are presented in the following figures. In

Figure 35, where the entirety of the formation process as well as the HPPC-tests are shown, it was observed that the formation process began at an earlier point in time. In addition, the formation process was also finished during a shorter time period.

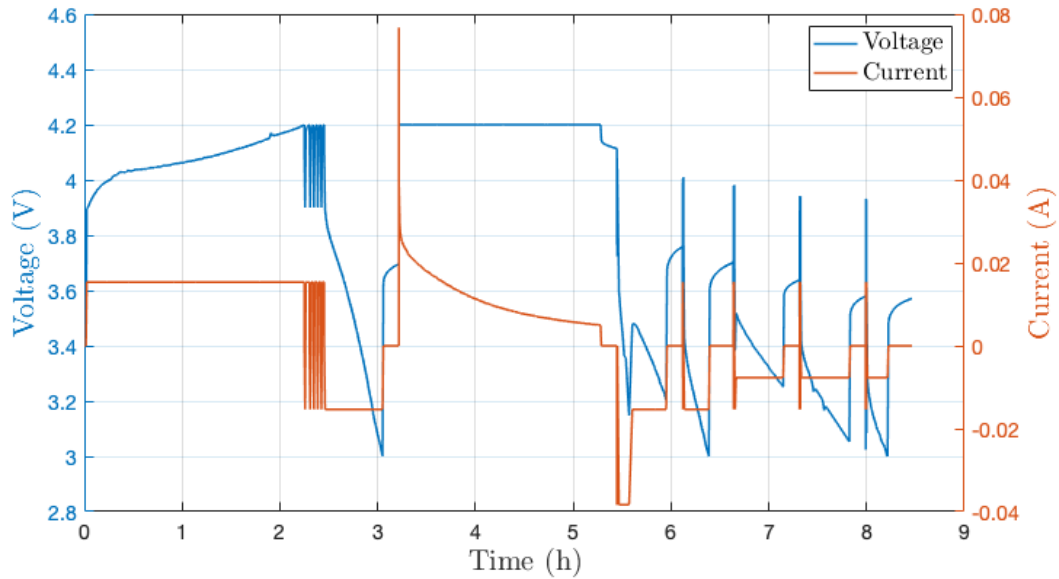


Figure 35: Voltage and current as a function of time for the whole cycling test for conventional cell 3.

Figure 36 presents a closer view of the formation process. It was observed that instead of applying an instantaneous current and voltage, they were slowly brought up to a constant charge. For the maximum discharge current, it can be observed that the discharge did not stay constant for some time but rather went back to charging. This is because the voltage reached 3.9 V faster than for conventional cell number 2.

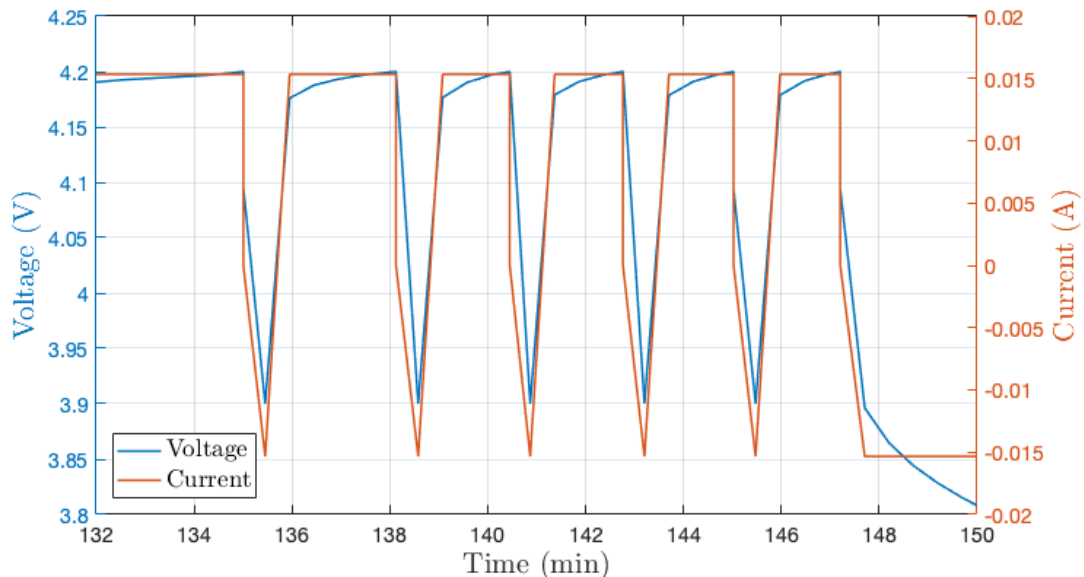


Figure 36: Voltage and current against time during the formation process for conventional cell 3.

A closer look at the HPPC-tests is presented in Figure 37. Note that there are differences in capacity for the two conventional cells, as presented in Table 1. Therefore, the discharge current,

as well as the time periods of discharging will vary between cell number 2 and 3.

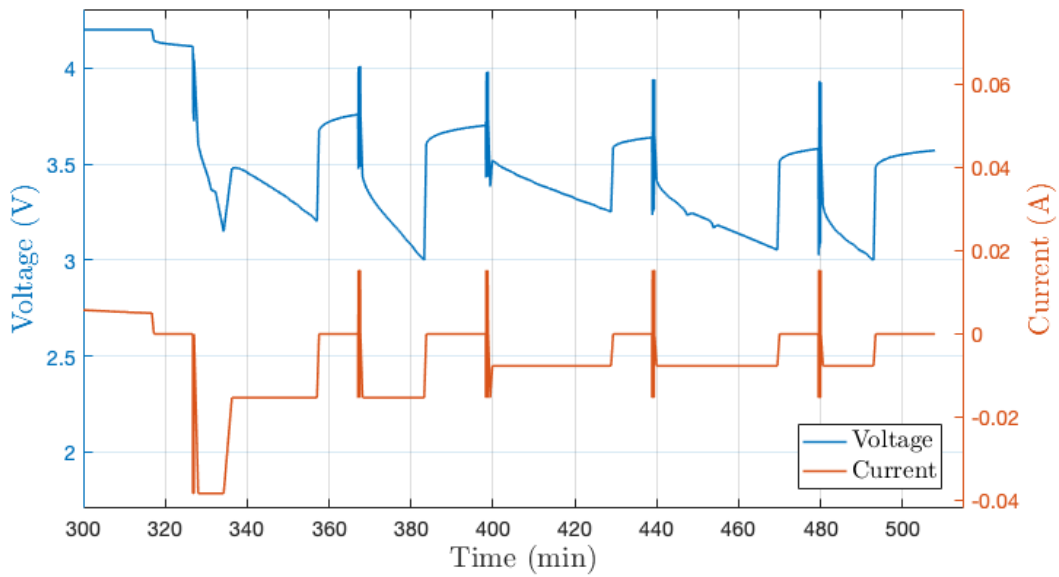


Figure 37: Voltage and current over time for the whole HPPC-process for conventional cell 3. All five HPPC-tests are shown as the thick vertical lines.

The HPPC-test performed at 90 % SOC, presented in Figure 38 below, shows the same characteristics for the cell as presented earlier. For this conventional cell, however, as mentioned previously, the C-rate was different, showing charging and discharging currents at ± 0.015 A.

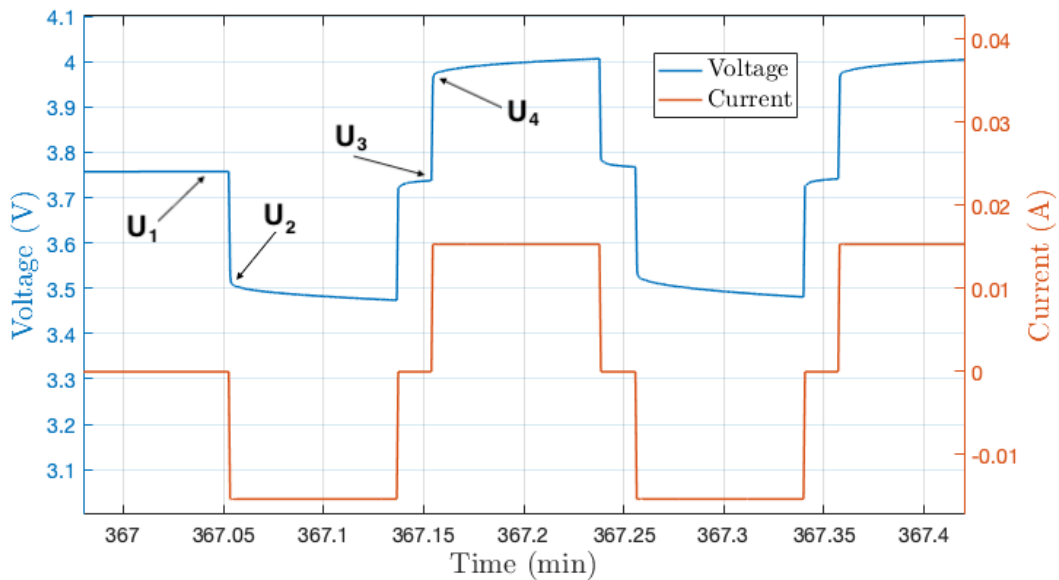


Figure 38: Voltage and current against time for conventional cell 3. The picture is zoomed in on the second HPPC-test performed under 90 % SOC.

For conventional cell number 3, the values used to calculate internal resistance are presented in Table 9 below.

Table 9: Values for voltage and current used in internal resistance calculation

Value	Voltage [V]	Current [A]
U_1	3.76	0
U_2	3.51	-0.015
U_3	3.74	0
U_4	3.97	0.015

Table 10 presents the results gathered from the HPPC-tests performed on conventional cell number 3. The results include both the internal resistance for charging and discharging and the irreversible specific heat generation. Note that the irreversible heat generation was significantly higher at 100 % SOC than for other SOC. This is because the current step had a magnitude of 0.038 A, while the others had a magnitude of 0.015 A, as presented in Table 9.

Table 10: Internal resistance and irreversible heat generation for conventional cell 3 for all HPPC-tests performed at different SOC

SOC	Discharge		Charge	
	Internal resistance (R_i)	Irreversible heat generation (q_i)	Internal resistance (R_i)	Irreversible heat generation (q_i)
100 %	7.89 Ω	2.71 W/kg	8.16 Ω	2.80 W/kg
90 %	16.67 Ω	0.89 W/kg	15.33 Ω	0.82 W/kg
80 %	16.67 Ω	0.89 W/kg	16.00 Ω	0.85 W/kg
76 %	23.33 Ω	1.25 W/kg	19.33 Ω	1.03 W/kg
71 %	30.67 Ω	1.64 W/kg	23.33 Ω	1.25 W/kg

4.4 Thermal Imaging Results

For the first thermal imaging observations, with the pouch cells placed in the thermal chamber together with the insulation around the steel rods, there was no heat dissipation to be discovered. Figure 39 below shows the pouch cell placed between the insulation, as the thermal conductivity was measured, with no apparent heat dissipation in that area. For comparison, the right corner of the cell was clamped with thumbs in this area, initially giving the area a heat signature of approximately 36 °C (body temperature). The tube on the right side of the figure contains a water flow heated to 38 °C.

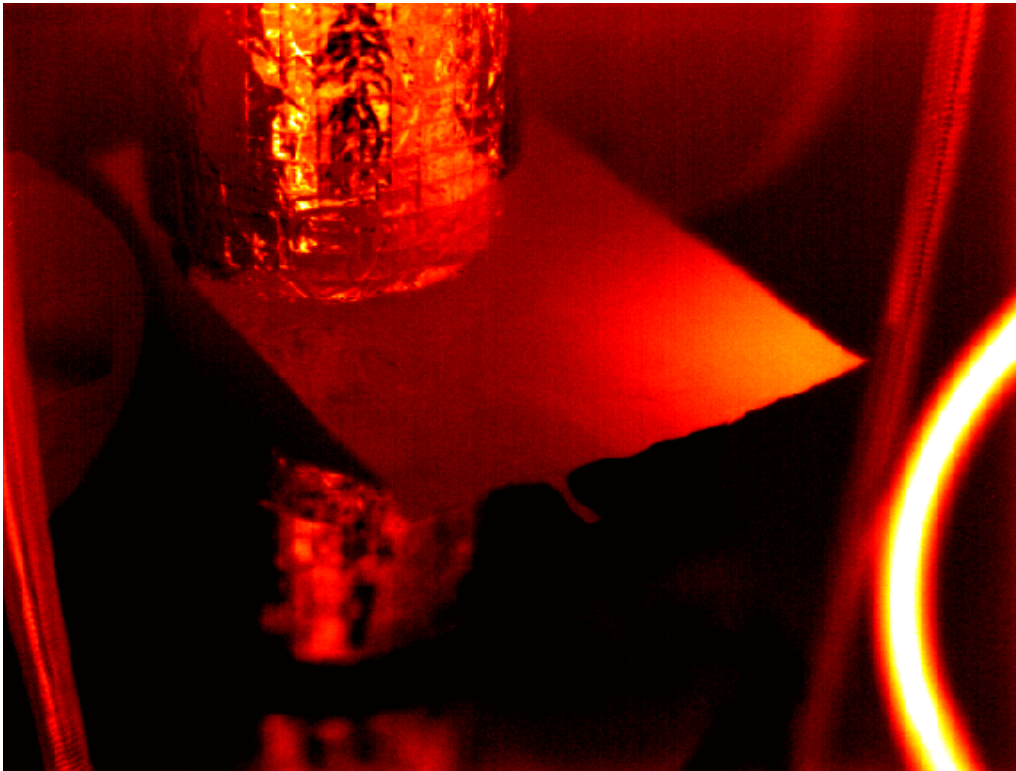


Figure 39: Thermal imaging of pouch cell in the thermal conductivity jig with insulation.

After this, the insulation was removed to closer inspect the heat dissipation around the testing area. Figure 40 shows the thermal imaging of the pouch cell between the steel rods without the thermal insulation. The steel rods proved quite reflective, but a temperature difference can be observed between the upper and lower steel rod. In the area where the upper steel rod is in contact with the pouch cell, a clear "circle" of heat can be observed. Further out from the contact point, it can be observed that the heat dissipates from the contact point. However, it does not dissipate far enough from its origin for it to be observable outside the insulation tube's radius. The insulation tube also reduces this heat transfer further.

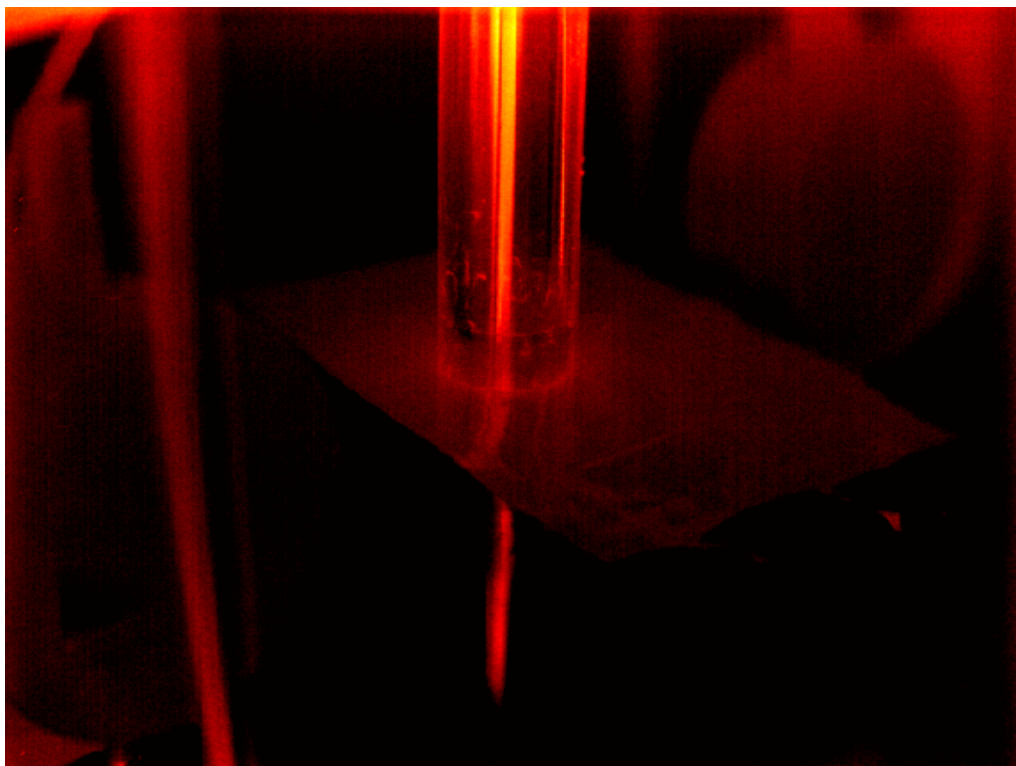


Figure 40: Thermal imaging of pouch cell in the thermal conductivity jig without insulation.

As for the beaker of hot water placed on the cells to observe the heat dissipation for a higher temperature, the camera produced the best visualization for the semi-solid cell. The image of the conventional cell, however, is much brighter. Both cells are shown in Figure 41 below. Observe the dark background due to a lower temperature. Note that the two images were taken at different times and have been merged afterward.

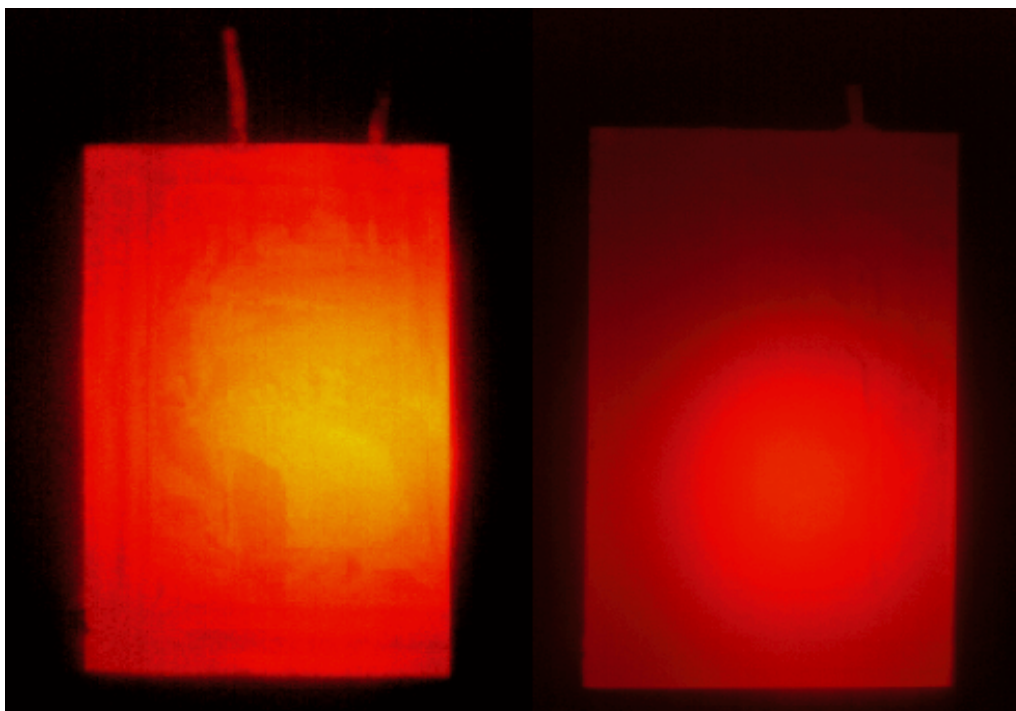


Figure 41: Heat dissipation in conventional cell (left) and semi-solid cell (right).

5 Discussion

The semi-solid state LIB technology is a new technology meant to improve the industry standard. For such new technologies, typically, little information or research can be found in the literature. It is challenging to gain information about how the semi-solid state LIB is constructed or how it works to a detailed level. Most of this information is bound by confidentiality due to the competition in the industry. Therefore, calculating theoretical values would be extremely difficult. Measurements of the thermal property values are then the only source of values obtainable.

5.1 Thermal Conductivity Tests

Due to the relative difference in the amount of current collector material compared to active material, which has a lower thermal conductivity than the metals used in the current collectors, the thermal conductivity was expected to be higher for the conventional cells than for the semi-solid state cells. However, this was not the case after testing the batteries in the thermal conductivity jig. As presented in Table 4, the thermal conductivity is generally higher for the semi-solid state cells than for the conventional. Even though the conventional cells, as mentioned above, have a higher percentage of current collector material than active material. The thickness of the pouch cells could be a deciding factor. Fourier's Law of Heat Conduction, Equation 2.22, states that if the heat flux and temperature difference remain the same throughout all the tests, a larger thickness will lead to higher thermal conductivity [73]. Another possibly influential factor could be that the semi-solid state cells contain more electrolyte than the conventional, due to the active material being a clay-like substance instead of a solid. Therefore, the electrode also brings in a notable amount of electrolyte in addition to the electrolyte added before sealing the battery. As mentioned in Section 2.6.3, the material interface between the electrode and electrolyte is eliminated. Studies have shown that the material interface contributes to over 88 % to the overall thermal resistance of LIBs [74]. The semi-solid cells could therefore have an increased thermal conductivity compared to the conventional cells, making heat removal more efficient.

The steel rods of the thermal conductivity jig are produced in the same diameter as typical button cells and therefore produce the best results for materials of this size. The steel rods can be insulated in a complete tube with the test subject inside, reducing the heat losses significantly. In the case of this study, thermal conductivity measurements were run on much larger pouch cells. Thus, the pouch cells did not fit perfectly within the insulating tube, and as shown in Figure 20, the insulation tube had to be cut in half to fit the pouch cells. This solution retained a good seal around the steel rods. However, it did not perfectly seal the entire surface area of the pouch cells, possibly leading to increased heat loss. Another possible error caused by not having a complete seal is that the steel rods that need to be precisely on top of one another to produce accurate results now had to be manually adjusted. If the steel rods deviate from each other by a couple of millimeters, the percentage of heat dissipating throughout the pouch cells increases significantly. Another source of error is heat dissipation throughout the exterior surface of the pouch cells. Since the areas of the pouch cells are larger than the area of the steel rod tips, some heat will dissipate throughout the pouch. The effects of all the different heat loss sources are presented as standard deviations in Table 4.

Comparing the thicknesses of the cells provided (Table 2) and the measured thicknesses prior to testing (Table 3), it is clear that the average measured values for the conventional LIBs are lower than that of the semi-solid state LIBs. One possible reason for this is incorrect information provided by the supplier, and another could be insufficient measurements. The latter is considered unlikely due to the batteries being measured several times. It was expected that the thicknesses would have increased for both LIB technologies due to the possibility of gas formation. If this is the case with the semi-solid cells, which on average measure $0.800 \mu\text{m}$, 2.5 % of the thickness would be gas formation or the result of an insufficient vacuum seal. Either of these could affect the thermal conductivity of the cell. However, since the conventional cells were measured thinner than the provided information, this assumption lacks credibility.

It is also worth mentioning that these batteries were made in-house and not in a production line.

Therefore, even though the batteries appear correctly made and of quality, slight errors may still occur in the production process. Such errors could be tiny air bubbles due to insufficient vacuuming and errors in thickness measurements.

Several steps were taken throughout the experimental phase concerning the thermal conductivity to decrease this deviation as much as possible. For the general insulation in the thermal conductivity jig, we tried using a Styrofoam plate to cover the entirety of the pouch cell, with holes cut out for the steel rods. This approach would potentially decrease the effects of external factors such as room temperature. However, we found that only using the tube and using the Styrofoam plates in addition to the tube resulted in minimal deviation from the original measurements. From the thermal imaging presented in Section 4.4, it was observed that the heat loss due to dissipation did not exceed the diameter of the insulating tube and that the totality of this heat loss would occur within this diameter.

To ensure the steel rods were directly on top of one another, circles were drawn on the metal plates where the thickness gauges sat, as shown in Figure 42 below. Keeping the thickness gauges within these circles kept the steel rods within a maximum of approximately 1 mm from being precisely on top of each other. As the samples were stacked on top of each other, the confidence in this approximation decreased. With the possibility of the cells not being perfectly horizontal, the upper steel rod could be slightly off-axis. This design flaw was noticed during an early test, which led to the calibration solution mentioned above.

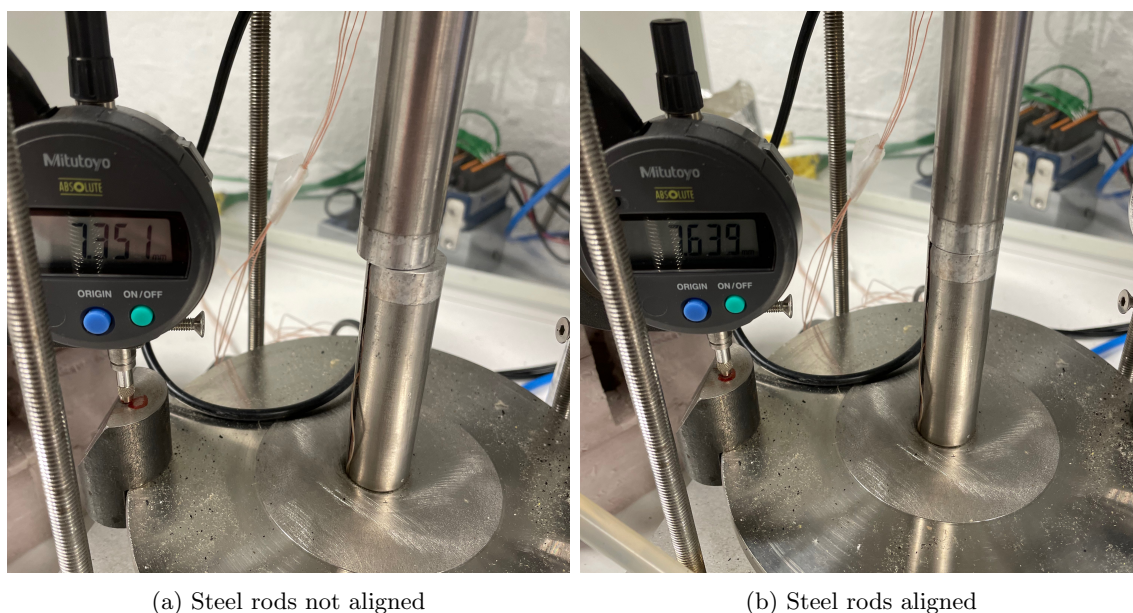


Figure 42: Alignment process of the steel rods with the circles drawn under the pressure gauges.

Modifications should be introduced to the general setup to minimize losses related to the positioning of the steel rods. Mainly, the upper part of the jig should be in a fixed position with a lever on top to raise or lower the upper steel rod. The upper steel rod would be in the same position, always ensuring direct heat transfer between the rods.

The program itself is another possible source of error. For the pressures put on the calibration material, the "standard maximum" applied pressure, according to the program, is 11.6 bar. This would mean the cells get compressed, leading to a higher heat transfer rate from the steel rods. Although this is the intended result of the pressure aspect of the experiment, the cells researched in this project (especially the semi-solid state cells) were at risk of becoming deformed or entirely broken as a result of this structural stress. This would mean, though, that the results would not be as ideal. It is possible to set a time period for how long the program applies pressure on the cells. This lets the pressure and heat transfer stabilize for better results. One possible source of error could be that the time intervals set for each pressure were too short. However, after leaving

one of the cells in the jig overnight, the program yielded no significant changes to the deviation. As a result, a conclusion was drawn that this source of error was insignificant.

The laboratory testing proved that creating good insulation for pouch cells is relatively complex. Creating an insulated box with hinges separating the pouch cell entirely from external factors could minimize heat loss, but changing the setup was outside the scope of this thesis. Another way to minimize heat loss would be constructing batteries in the form of button cells instead of pouch cells to fit perfectly in the insulated thermal conductivity jig. This would remove the issue with insulation in its entirety, presenting the possibility for an insulating tube completely covering the steel rods. Again, this would make sure that the steel rods sit directly on top of each other, removing this source of error as well. Ideally, to investigate the thermal conductivity even closer, all parts of the battery should be separated and investigated independently. This way, the thermal conductivity could be calculated using values measured with a minimal margin of error.

5.2 Specific Heat Capacity

When comparing Figure 29a and 29b, it is observable that the temperatures stabilize much faster for the conventional stack than for the semi-solid state stack. The conventional stack has reached a steady-state end temperature after around 500 seconds, while the semi-solid state stack reached a constant temperature after approximately 1500 seconds. The semi-solid state stack uses three times longer to reach the end temperature (room temperature). After all, this makes sense since the semi-solid state cells have greater specific heat capacity than the conventional ones and will retain heat longer and counteract temperature changes to a greater extent. The higher the specific heat capacity, the less the change in temperature will be for a given amount of heat applied to a given mass. This follows with the theory in Section 2.5.3.

The semi-solid state cells have a greater specific heat capacity than the conventional cells. This is most likely due to the semi-solid state cells having much thicker electrodes and holding on to the heat longer. For a thicker and more massive object, it requires more heat to change the object's temperature, given that it consists of the same materials or substances as the reference. The difference in specific heat capacity between the technologies was significant. Therefore, several factors may contribute to this deviation. For example, the temperatures could have been slightly different and may have affected the results. Here, the test could have been set up differently in order for the system to produce more consistent measurement conditions for both tests. The temperatures could have been more similar before the measurements began and the entire system could have been isolated better against external factors.

Another critical thing to mention is that there are considerable uncertainties and deviations in the results, as the cell temperatures were much smaller than they ideally would have been. A drop from 45 °C to 33 °C before entering the water bath is significant. It is difficult to know if it is correct since the thermocouples measured the temperature on the cell surface and not in the centre of the cell. The core temperature would have been higher than what the thermocouples measured, and this could give a significant deviation from the cells' actual specific heat capacity.

Realistically, the actual cell temperature should be somewhere between the theoretical (45 °C) and the measured temperature (33 °C), as one must expect a slight temperature drop from the cells being taken out of the thermal chamber until the measurement was initialized. From Equation 3.1, it is clear that the specific heat capacity will be higher for a lower temperature difference between the cells and the final temperature. Therefore, it is assumed that the calculated values for specific heat capacity are a little too high for both the conventional cells and the semi-solid state cells, as a larger T_{cell} value would produce a smaller specific heat capacity.

If it is assumed that the cell temperature was 45 °C while the rest of the temperatures and masses were the same, the specific heat capacities would be as follow:

$$c_{p,cell,semi-solid} = 815.74 \frac{\text{J}}{\text{kg} \cdot \text{K}} \quad \text{and} \quad c_{p,cell,conv} = 563.8 \frac{\text{J}}{\text{kg} \cdot \text{K}}$$

This illustrates how significant the uncertainty is, since these heat capacities differ by 49.6 %

and 47.2 % compared to those calculated in Section 4.2. Therefore, it is difficult to say how representative these results are of the actual heat capacities of the cells. However, the calculations provide a clear indication that the semi-solid state cells have a greater specific heat capacity than the conventional ones.

5.2.1 Uncertainties and Improvements

During the test, several uncertainties affected the measurements, such as limited insulation, considerable mass difference between the water and the pouch cells, difference in temperature on the surface and the core of the cells, chance of inaccurately calibrated thermocouples, a tape layer around the pouch cell stacks, and the use of tap water instead of distilled water. All these factors add to the possible sources of error and may lead to deviations from the actual results.

The insulation could have been improved since the temperature of the pouch cells dropped by around 11 °C from the small distance from the thermal chamber to the water bath. Therefore, when the measurement started, the maximum surface temperature was approximately 34 °C instead of 45 °C, which was the temperature in the thermal chamber. The calculations were therefore based on the actual starting temperature of 34 °C instead of the theoretical starting temperature of 45 °C.

The tape layer that holds the cell stacks together also leads to uncertainties in the measurements since the mass of the used tape was close to that of one cell. In addition, the tape has its own heat capacity, which also impacts the results. The total mass of the three semi-solid state pouch cells without the tape was 15 grams, so the tape made up 22 % of the mass of the stack. For the conventional cells, the total mass of this stack was 13.4 grams without the tape, so the tape accounted for 21 % of the mass of this stack. This indicates the potential impact the tape may have had on the results as it accounted for a significant proportion of the total mass of the stacks.

The temperature measurement on the surface of the cells may be different from the core temperature inside the cell. Therefore, the thermocouples may show a different temperature than the actual core temperature that is relevant. The core temperature will likely be a few degrees higher than the surface temperature since the surface is exposed to the air. If there was enough time and we were allowed to open up the cells, thermocouples could be placed inside the cells so that they would measure their core temperature as well. This would have given a more accurate measurement of the temperatures and, thereby, a more accurate specific heat capacity. Unfortunately, the semi-solid state pouch cells could not be opened due to confidentiality. Therefore, this uncertainty must be accepted for this thesis.

There was a minimal temperature contribution from the pouch cells in the water bath due to the significant mass difference between the cells and the water. The pouch cells were tiny and, therefore, were quickly impacted by the temperature differences in both the air and the water. In addition, the specific heat capacity of water is very high compared to the pouch cells. To improve the impact of the cells in the water bath, the pouch cells were stacked together to increase the mass and the temperature contribution of the cells. Unfortunately, this has a minimal impact, and the water still contributes much more toward the end temperature. To further compensate for the contribution differences, the pouch cells could have been made larger so that the mass of the cells became closer to the mass of the required water in the water bath. This would increase the contribution of the pouch cells since the mass affects the heat capacity. In addition, another liquid than water with lower heat capacity could have been used. This would also make the differences smaller. For example, a methanol bath could have been used as methanol has a specific heat capacity of $2530 \text{ J}\cdot\text{kg}^{-1}\cdot\text{K}^{-1}$, i.e., approximately 1.7 times lower than water.

However, even though the results were not perfect, some results from the test illustrate the development of the temperatures. There were several uncertainties in the experiment, yet the temperature trend was the most important. Therefore, this test proved helpful in giving an idea of the specific heat capacity of the pouch cells. To minimize the uncertainties, the pouch cells could have been insulated better, the thermocouples could have been calibrated more accurately, and the cells could have been made larger. Additionally, we could have used more accurate and sensitive measuring

instruments, opened up the cells and measured the core temperature with thermocouples inside the cells, and distilled water could have been used instead of tap water for more accurate knowledge of its thermal properties. Regardless, we got results that clearly displayed the development in the water bath. Therefore, we are satisfied with the results even though the sources of error were numerous.

5.3 Internal Resistance

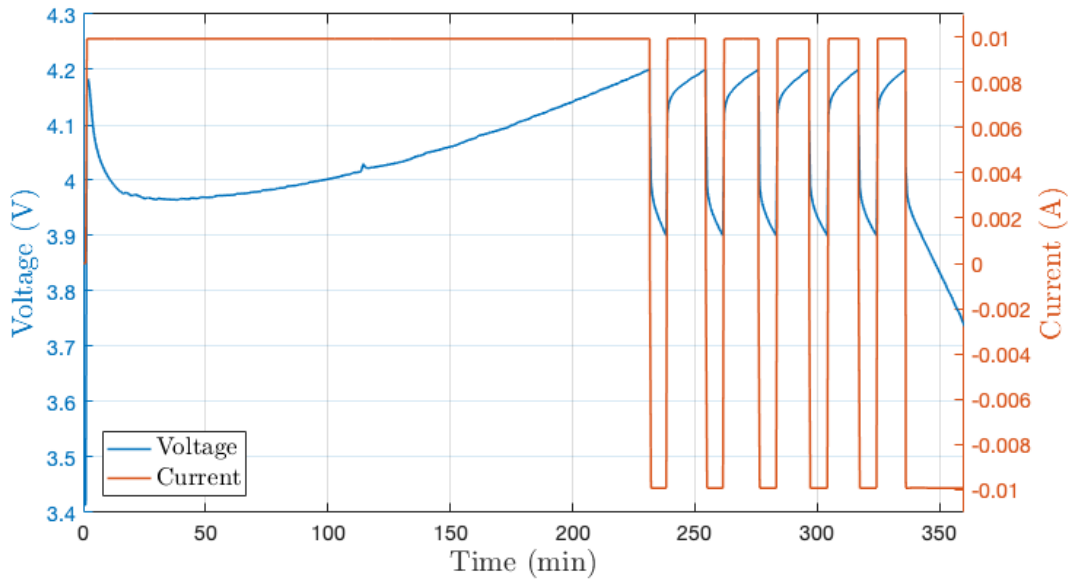
Data for conventional cell number 2 and 3 were presented in the internal resistance results. All conventional cells were tested. However, due to a broken current collector in cell number 1, only cell 2 and 3 produced results of value. For the semi-solid cells, only one of them had long enough tabs for the "clip" to attach and apply current, while the tabs on the other two were either too short or ripped off, most likely due to rough handling during the previous experiments.

Conventional cell number 2 and 3 tested with no other problems than an occasional change in applied current. Meanwhile, the tests performed on the semi-solid state cells did not yield any results of value. As observed in Table 8 and 10, the internal resistances for conventional cell 2 and 3 were high. The internal resistance was expected to be even higher for the semi-solid state cells due to their thicker electrodes. As mentioned in Section 2.6.2, this is a common consequence related to increased diffusion distance. Therefore, charging the semi-solid state cells proved difficult, even though several different C-rates were applied. An effect of the increased internal resistance is an increase in heat generation. One possible reason the semi-solid cell did not produce valuable results could be an internal short circuit in the cell. As soon as the current was disengaged, the voltage dropped simultaneously, which is a sign of short circuits. This happens when there is a flow of current between the anode and the cathode, which means they were most likely in contact with each other. This may be direct physical contact or electrical contact, as the separator could be damaged.

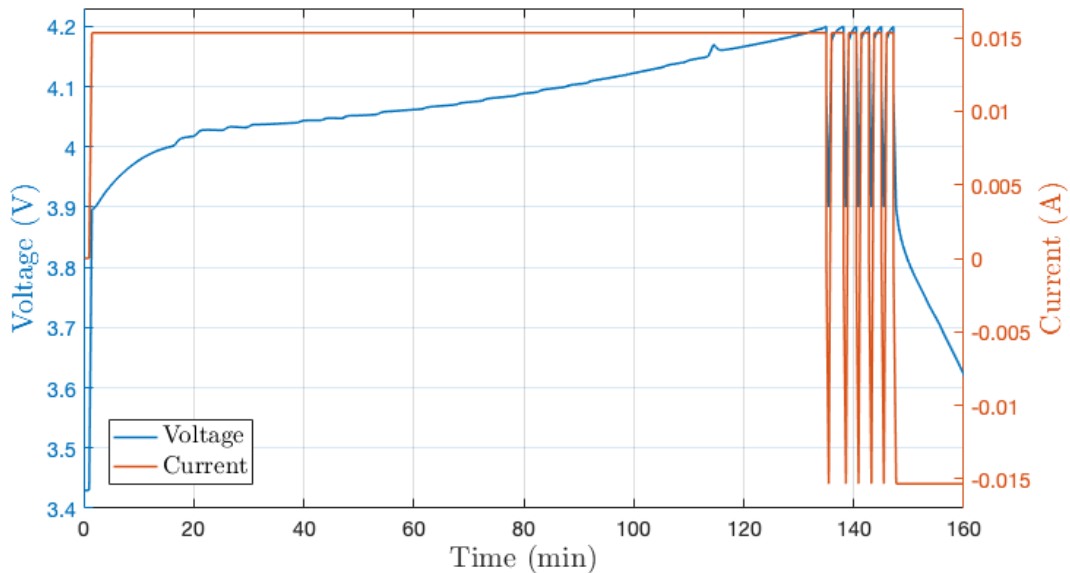
As mentioned earlier, the semi-solid state LIB technology is young. The testing equipment and software used in the internal resistance measurements have primarily been used to test conventional cells. The nature of how a semi-solid state LIB acts when current is applied is therefore mostly unknown, and no specialized openly available programs have been created for these batteries yet. The processes of formation and HPPC-testing for semi-solid state LIBs may therefore be entirely different to those for conventional NMC442 LIBs. After scouring the internet, no other information or research was found on the formation and HPPC-testing of semi-solid state LIBs. To determine precisely how much more heat was generated for the semi-solid state LIBs than that of the conventional LIBs, it is suitable to suggest more research in this area. With more time, several different C-rates and other procedures could be tested to gain more knowledge on how these batteries perform.

For the charging and formation processes for conventional cells number 2 and 3 (presented in Figure 43 below), certain elements stood out. The first of which can be observed in Figure 43a, where the voltage starts at approximately 4.2 V, then decreases to below 4 V before slowly increasing again to 4.2 V. A more "typical" process can be observed for conventional cell number 3 in Figure 43b. In the figure, the voltage instantaneously increases to 3.9 V and then slowly increases to 4.2 V. Explanations for this are speculative at best; it could, for example, be equipment-related or related to an increase in permeability between the electrolyte and anode caused by the SEI-layer that forms.

The time period of the formation process also differs significantly for the two conventional cells. While conventional cell number 2 endured this formation process for approximately 100 minutes, conventional cell number 3 only endured approximately 15 minutes. This could be due to differences in internal resistance or capacities.



(a) Voltage and current against time from $t = 0$ to end of formation process for conventional cell 2.



(b) Voltage and current against time from $t = 0$ to end of formation process for conventional cell 2.

Figure 43: Voltage and current against time from $t = 0$ to end of formation process for conventional cells.

As can be observed for the formation process of conventional cell number 2 in Figure 31, the constant current periods are longer when charging than when discharging. Another observation is that the periods of constant current when charging shortens for each interval and that the periods when discharging become slightly longer. This is due to the concept of the Coulomb efficiency, which is usually used to describe released capacity. The Coulomb efficiency is the ratio of discharge capacity to the charge capacity [75]. At the stage where the discharge periods are shorter than the charge periods, the battery has a low Coulomb efficiency. This is due to the battery "losing" lithium to the SEI layer. The Coulomb efficiency increases as the charging periods shorten, becoming more like the discharging periods. When the Coulomb efficiency increases, the SEI layer stabilizes.

For further research, cells with sufficiently extended tabs should be provided. The three semi-solid state LIBs are shown in Figure 44 below. The figure shows the leftmost cell missing the aluminium

tab after it got ripped off in a failed attempt to reattach it. The cell in the middle had long enough tabs, and the cell to the right had tabs that were too short. An attempt was made to extend the aluminium tab by wrapping it in a piece of aluminium foil. In the figure, the nickel tabs are on the right side of the two leftmost pouch cells while on the right for the rightmost cell.



Figure 44: Three semi-solid state cells, the middle one having long enough tabs for formation and HPPC-testing.

While the typical internal resistance of a production-grade NMC LIB usually measures in milliohms, the internal resistance of the conventional cells tested for this project measured much higher. One possible reason for this could be that these pouch cells were made in-house, as mentioned previously. Several factors may affect the internal resistance, but insufficient vacuuming and gas formation inside the cells are likely to be significant factors. Gas formation inside the battery can increase the internal resistance by further hindering the flow of electrons.

Figure 45 below shows how the internal resistance of the cells develops for decreasing SOC.

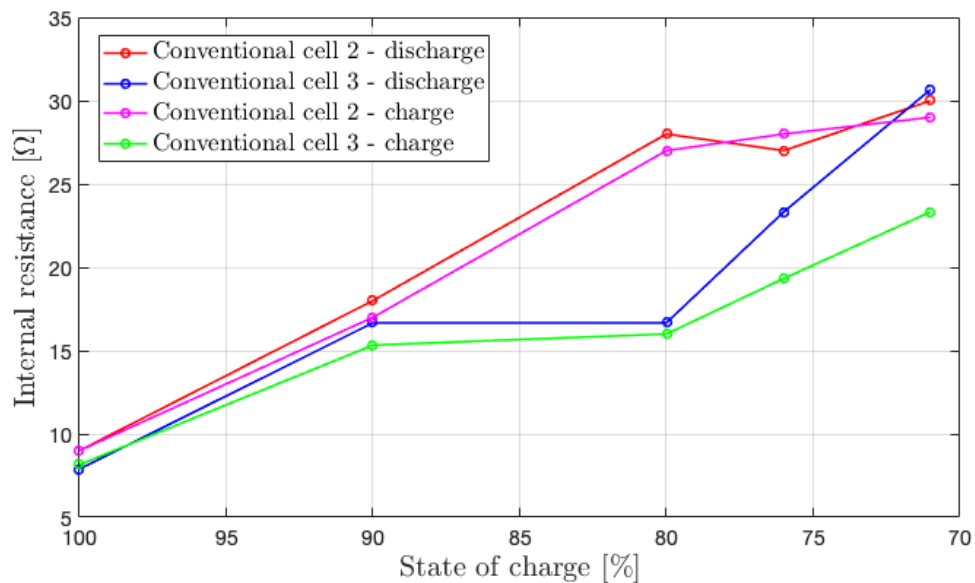


Figure 45: Internal resistance as a function of SOC for both cells. Plots for both charge and discharge are presented in the figure.

It can be observed that the trend is the same for both cells, with the internal resistance increasing for decreasing SOC, both for charging and discharging. This makes sense considering that the more the cells are charged and discharged, the more overpotentials will build up, thus increasing resistance. Generally, the discharge processes have a slightly higher internal resistance than the charge processes.

5.3.1 Heat Generation from Internal Resistance

The heat generation calculated in this project results from ohmic overpotential and is the main contributor to irreversible energy loss. However, the reversible heat generation occurs due to the chemical reactions within the cell. The change in entropy is a parameter that the reversible heat generation depends on. This project's neglect of the reversible heat generation is due to insufficient material information. Therefore, to form a complete model of the heat generation, one should include reversible heat generation as well as irreversible heat generation. The entropy change in the battery and the reversible heat generation is therefore suitable for further research.

Figure 46 below shows the specific heat generation of the cells with respect to SOC.

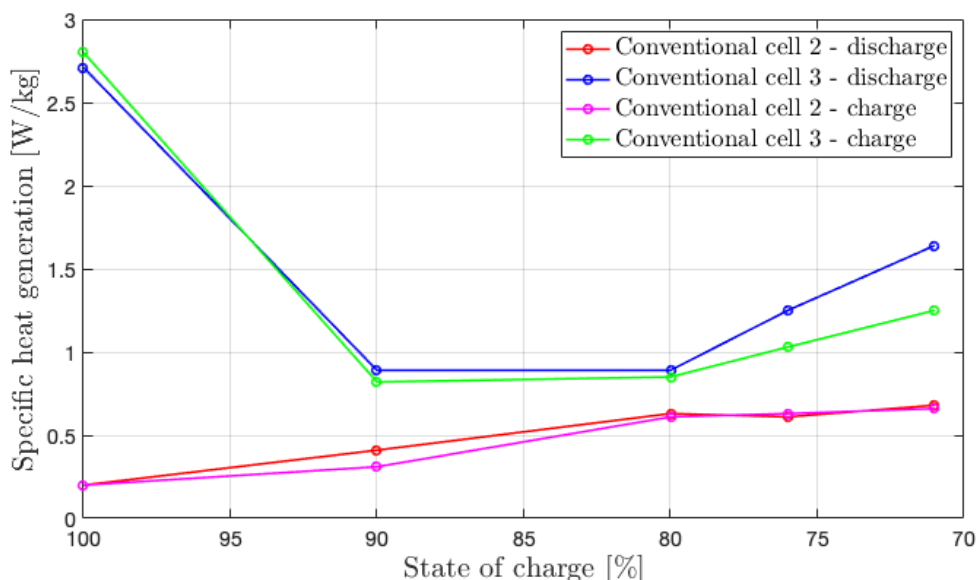


Figure 46: Specific heat generation as a function of SOC for both cells. Plots for both charge and discharge are presented in the figure.

In Figure 45, the trend remains the same as for the internal resistance, except that the specific heat generation peaks at 100 % SOC for conventional cell 3. The heat generation, in general, was higher for conventional cell 3 due to it being cycled with a greater current. Since the heat generation is directly proportional to the square of the current, the magnitude of the current affects the heat generation significantly. The first HPPC-test conducted on conventional cell 3, at 100 % SOC, applied the "typical" C-rate used for other LIBs. However, the C-rate was decreased because the voltage drop was too high for lower SOC. In Figure 45, the heat generation is therefore greatest at 100 % SOC due to the current magnitude being 0.038 A instead of 0.015 A, which was applied for the remaining of the HPPC-tests.

The high current at 100 % SOC may be due to the battery having a slight difference in capacity from what the provided information stated. Both capacity values and C-rate had to be stated prior to the formation process and HPPC-tests. If the actual capacity was either greater or lower than the stated value, the current magnitude would be affected. Since the C-rate is directly proportional to the current and inversely proportional to the capacity (see Equation 2.9), one can assume that the actual capacity was slightly larger than what was stated.

Ideally, the heat generation calculation for the two cells should have been executed with the same current to ensure that the basis of comparison was as accurate as possible.

5.4 Thermal Imaging

The thermal imaging of the cells indicated no significant heat dissipation exceeding the radius of the insulation tube. There was, however, some heat dissipation inside this radius. This further supports the claim that to obtain results with minimal deviation or heat loss, the cells should be designed to fit inside the diameter of the steel rods.

In Figure 41, heat dissipation from high temperatures can be seen for both cell types. These images were taken separately, with separate calibrations of the camera, both of which could cause the conventional cell to have a brighter color. Another cause of this brighter color and more significant heat dissipation could be the thickness of the cell, with heat dissipating faster and further for the thinner cell. This could correlate with the semi-solid state cells having a greater specific heat capacity than the conventional ones, making them hold on to the heat longer. However, these images were taken with the sole intent to visualize heat dissipation throughout the pouch cells and not to measure any values or differences between them.

Multiple experiments can be carried out for further research, such as measuring the precise temperatures around the cell and how they change as the heat dissipates. Another experiment could be recording the heat dissipation for both cells and measuring the time it takes the heat to reach points throughout the cells and eventually the time it takes for the cell to reach room temperature again.

6 Conclusions

The purpose of this project was to investigate thermal conductivity, specific heat capacity, and heat generation of semi-solid state LIBs. In order to gain a better understanding of the differences in these thermal properties, identical experiments were conducted on both the conventional and semi-solid state LIBs.

The first thermal property measured was the thermal conductivity of the cells. The thermal conductivity was measured by placing cells from each technology in a thermal conductivity meter between steel rods with a known thermal conductivity, and measuring the amount of heat transferred between the rods. From these tests, the thermal conductivity peak was measured $0.3986 \pm 0.168 \text{ W}\cdot\text{m}^{-1}\cdot\text{K}^{-1}$ for the conventional cells, and $0.4795 \pm 0.181 \text{ W}\cdot\text{m}^{-1}\cdot\text{K}^{-1}$ for the semi-solid state cells.

For the heat capacity, the cells of each technology were stacked separately. First, three conventional cells were taped together, and then the same procedure was done for the semi-solid state cells. The stacks were then heated to $45 \text{ }^\circ\text{C}$ in a thermal chamber and submerged in an insulated water bath at $22 \text{ }^\circ\text{C}$. At the same time, the temperature development in the system was measured and recorded with three thermocouples. As a result, the specific heat capacities of the conventional cells and the semi-solid state cells were calculated to be $1193.31 \text{ J}\cdot\text{kg}^{-1}\cdot\text{K}^{-1}$ and $1646.05 \text{ J}\cdot\text{kg}^{-1}\cdot\text{K}^{-1}$, respectively. However, the measurements had considerable uncertainty.

From the HPPC-tests, the internal resistance and irreversible heat generation were calculated. While two of the conventional cells produced results, the third had a broken current collector. Unfortunately, the semi-solid state cells produced zero results of value, either due to broken tabs or a suspected internal short circuit. The internal resistances calculated for different SOC were higher than expected for the conventional cells that produced results. The internal resistance ranged from $7.89 \text{ }\Omega$ at 100 % SOC to $30.67 \text{ }\Omega$ at 71 % SOC. While the semi-solid state cells could not produce results, the internal resistance was expected to be higher than for the conventional cells due to their thicker electrodes resulting in increased diffusion distance. A consequence of this increase in internal resistance is an increase in heat generation.

6.1 Further Research

For the thermal conductivity tests, the general setup should be improved to heighten the jig's accuracy, only relying on the batteries. Several improvements could be made to the setup, such as making sure the steel rods are accurately centred and improving the insulation. For further research within this area, all components for both technologies should be separated for individual measurements. This would make it possible to investigate the batteries' thermal conductivity more accurately. Another exciting result would be finding the difference in thermal conductivity from measurements versus theoretical calculations. This would require additional material information.

For further research regarding the specific heat capacity tests, the room temperature, water temperature, and Styrofoam temperature should be investigated further to find a better convergence. To produce more accurate readings, the thermocouples should also be calibrated with additional temperature points. While these factors are essential for further research, the batteries also show significant potential for improvement. Having one LIB of each technology with several stacked electrode pairs inside would provide a better basis for accurate results. With the provided unit cells' temperatures dropping rapidly, a larger cell with more electrode pairs should hold on to this temperature for a more extended period of time. Another improvement could be replacing the water bath with, e.g., an ethanol bath, as ethanol has a much lower specific heat capacity than water.

The main cause of the semi-solid state LIBs not being able to produce results for internal resistance was broken or ripped tabs. For the cell with sufficiently extended tabs, a suspected short circuit may have prevented it from producing results. Therefore, it would be suitable to suggest that different cells with sufficiently long tabs are provided for further research in this area.

To develop a complete thermal model for semi-solid state LIBs, several additional thermal properties need to be examined, e.g., reversible heat generation, thermal expansion, and thermal diffusivity. With time, semi-solid state technology will develop, and theoretical information will become more accessible. Simultaneously, more accurate thermal models will be developed.

Bibliography

- [1] *MATLAB - MathWorks*. en. URL: <https://se.mathworks.com/products/matlab.html> (visited on 10/05/2022).
- [2] *What is LabVIEW?* en. URL: <https://www.ni.com/en-no/shop/labview.html> (visited on 10/05/2022).
- [3] *Software*. en-US. URL: <https://www.arbin.com/software/> (visited on 11/05/2022).
- [4] *Zotero — Your personal research assistant*. URL: <https://www.zotero.org/> (visited on 10/05/2022).
- [5] *Microsoft Excel Spreadsheet Software — Microsoft 365*. en-ww. URL: <https://www.microsoft.com/en-ww/microsoft-365/excel> (visited on 10/05/2022).
- [6] Naoki Nitta et al. ‘Li-ion battery materials: present and future’. en. In: *Materials Today* 18.5 (June 2015), pp. 252–264. ISSN: 1369-7021. DOI: 10.1016/j.mattod.2014.10.040. URL: <https://www.sciencedirect.com/science/article/pii/S1369702114004118> (visited on 29/03/2022).
- [7] Yet-Ming Chiang et al. ‘Semi-solid electrodes having high rate capability’. U.S. pat. US8993159B2. 24M Technologies Inc. 31st Mar. 2015. URL: <https://patents.google.com/patent/US8993159?q=semi+solid+lithium+ion+batteries#patentCitations>.
- [8] Chen Liao. ‘Fundamentals of rechargeable lithium ion and beyond lithium ion batteries’. In: *Batteries*. 2053-2563. IOP Publishing, 2021, 1-1 to 1–24. ISBN: 978-0-7503-2682-7. DOI: 10.1088/978-0-7503-2682-7ch1. URL: <https://dx.doi.org/10.1088/978-0-7503-2682-7ch1>.
- [9] Colin Ringdalen MacDonald and Christian Helledal Trandem. ‘Impact of Cooling Methods on Ageing in Lithium-ion Battery Cells’. eng. In: (2021). Accepted: 2021-10-20T17:28:45Z Publisher: NTNU. URL: <https://ntnuopen.ntnu.no/ntnu-xmlui/handle/11250/2824272> (visited on 28/03/2022).
- [10] Marco Sauermoser. *Lithium-Ion Batteries*. Lecture Notes Week 38 - Lithium-ion Batteries, FENT2314 Energy storage 2, NTNU, ntnu.blackboard.com. Sept. 2021. (Visited on 31/03/2022).
- [11] Da Deng. ‘Li-ion batteries: basics, progress, and challenges’. en. In: *Energy Science & Engineering* 3.5 (2015). eprint: <https://onlinelibrary.wiley.com/doi/pdf/10.1002/ese3.95>, pp. 385–418. ISSN: 2050-0505. DOI: 10.1002/ese3.95. URL: <https://onlinelibrary.wiley.com/doi/abs/10.1002/ese3.95> (visited on 19/05/2022).
- [12] Shilpi Nagpal. *Electrochemical Series - Chemistry, Class 12, Electro Chemistry*. Class Notes. 29th May 2019. URL: <https://classnotes.org.in/class12/chemistry12/electro-chemistry/electrochemical-series/> (visited on 09/05/2022).
- [13] *How Does a Lithium-ion Battery Work?* Energy.gov. 14th Sept. 2017. URL: <https://www.energy.gov/eere/articles/how-does-lithium-ion-battery-work> (visited on 24/03/2022).
- [14] Gregory L. Plett. *Battery management systems: battery modeling. Volume 1*. en. OCLC: ocn909081842. Boston : London: Artech House, 2015. ISBN: 978-1-63081-023-8.
- [15] Jakob Sandstad and Geir Martin Haarberg. *elektrode*. In: *Store norske leksikon*. 7th Nov. 2021. URL: <http://snl.no/elektrode> (visited on 29/03/2022).
- [16] Lena Spitthoff, Paul R. Shearing and Odne Stokke Burheim. ‘Temperature, Ageing and Thermal Management of Lithium-Ion Batteries’. In: *Energies* 14.5 (2021). ISSN: 1996-1073. DOI: 10.3390/en14051248. URL: <https://www.mdpi.com/1996-1073/14/5/1248>.
- [17] Gert Berckmans et al. ‘Analysis of the effect of applying external mechanical pressure on next generation silicon alloy lithium-ion cells’. en. In: *Electrochimica Acta* 306 (May 2019), pp. 387–395. ISSN: 0013-4686. DOI: 10.1016/j.electacta.2019.03.138. URL: <https://www.sciencedirect.com/science/article/pii/S0013468619305614> (visited on 29/03/2022).
- [18] Xiuxia Zuo et al. ‘Silicon based lithium-ion battery anodes: A chronicle perspective review’. en. In: *Nano Energy* 31 (Jan. 2017), pp. 113–143. ISSN: 2211-2855. DOI: 10.1016/j.nanoen.2016.11.013. URL: <https://www.sciencedirect.com/science/article/pii/S2211285516304931> (visited on 29/03/2022).

- [19] Veerapandian Ponnuchamy, Stefano Mossa and Ioannis Skarmoutsos. ‘Solvent and salt effect on Lithium ion solvation and contact ion pair formation in organic carbonates: a quantum chemical perspective’. In: *The Journal of Physical Chemistry C* 122.45 (Nov. 2018). arXiv: 1806.09947, pp. 25930–25939. ISSN: 1932-7447, 1932-7455. DOI: 10.1021/acs.jpcc.8b09892. URL: <http://arxiv.org/abs/1806.09947> (visited on 29/03/2022).
- [20] Ghassan Zubi et al. ‘The lithium-ion battery: State of the art and future perspectives’. en. In: *Renewable and Sustainable Energy Reviews* 89 (June 2018), pp. 292–308. ISSN: 1364-0321. DOI: 10.1016/j.rser.2018.03.002. URL: <https://www.sciencedirect.com/science/article/pii/S1364032118300728> (visited on 29/03/2022).
- [21] Geir Martin Haarberg. *anode*. In: *Store norske leksikon*. 13th Sept. 2021. URL: <http://snl.no/anode> (visited on 29/03/2022).
- [22] Manh-Kien Tran et al. ‘Comparative Study of Equivalent Circuit Models Performance in Four Common Lithium-Ion Batteries: LFP, NMC, LMO, NCA’. en. In: *Batteries* 7.3 (Sept. 2021). Number: 3 Publisher: Multidisciplinary Digital Publishing Institute, p. 51. ISSN: 2313-0105. DOI: 10.3390/batteries7030051. URL: <https://www.mdpi.com/2313-0105/7/3/51> (visited on 31/03/2022).
- [23] Geir Martin Haarberg. *katode*. In: *Store norske leksikon*. 13th Sept. 2021. URL: <http://snl.no/katode> (visited on 29/03/2022).
- [24] Imanol Landa-Medrano et al. ‘In Situ Analysis of NMCgraphite Li-Ion Batteries by Means of Complementary Electrochemical Methods’. en. In: *Journal of The Electrochemical Society* 167.9 (Jan. 2020), p. 090528. ISSN: 0013-4651, 1945-7111. DOI: 10.1149/1945-7111/ab8b99. URL: <https://iopscience.iop.org/article/10.1149/1945-7111/ab8b99> (visited on 31/03/2022).
- [25] Rahul Bollini. *Understanding a Lithium-ion cell datasheet • EVreporter*. en-US. Section: EV Learning. Dec. 2021. URL: <https://evreporter.com/understanding-a-lithium-ion-cell-datasheet/> (visited on 01/04/2022).
- [26] Sewon Park et al. ‘Replacing conventional battery electrolyte additives with dioxolone derivatives for high-energy-density lithium-ion batteries’. en. In: *Nature Communications* 12.1 (Feb. 2021). Number: 1 Publisher: Nature Publishing Group, p. 838. ISSN: 2041-1723. DOI: 10.1038/s41467-021-21106-6. URL: <https://www.nature.com/articles/s41467-021-21106-6> (visited on 31/03/2022).
- [27] Youzhi Song et al. ‘From separator to membrane: Separators can function more in lithium ion batteries’. In: *Electrochemistry Communications* 124 (1st Mar. 2021), p. 106948. ISSN: 1388-2481. DOI: 10.1016/j.elecom.2021.106948. URL: <https://www.sciencedirect.com/science/article/pii/S1388248121000321> (visited on 10/05/2022).
- [28] Tetsuya Kawamura, Shigeto Okada and Jun-ichi Yamaki. ‘Decomposition reaction of LiPF₆-based electrolytes for lithium ion cells’. In: *Journal of Power Sources* 156.2 (2006), pp. 547–554. ISSN: 0378-7753. DOI: <https://doi.org/10.1016/j.jpowsour.2005.05.084>. URL: <https://www.sciencedirect.com/science/article/pii/S0378775305008219>.
- [29] Pengcheng Zhu et al. ‘A review of current collectors for lithium-ion batteries’. In: *Journal of Power Sources* 485 (2021), p. 229321. ISSN: 0378-7753. DOI: <https://doi.org/10.1016/j.jpowsour.2020.229321>. URL: <https://www.sciencedirect.com/science/article/pii/S0378775320316098>.
- [30] Silje Nornes Bryntesen et al. ‘Opportunities for the State-of-the-Art Production of LIB Electrodes-A Review’. In: *Energies* 14 (Mar. 2021), p. 1406. DOI: 10.3390/en14051406.
- [31] Arno Kwade et al. ‘Current status and challenges for automotive battery production technologies’. en. In: *Nature Energy* 3.4 (Apr. 2018). Number: 4 Publisher: Nature Publishing Group, pp. 290–300. ISSN: 2058-7546. DOI: 10.1038/s41560-018-0130-3. URL: <https://www.nature.com/articles/s41560-018-0130-3> (visited on 04/04/2022).
- [32] Tuan-Tu Nguyen et al. ‘The electrode tortuosity factor: why the conventional tortuosity factor is not well suited for quantifying transport in porous Li-ion battery electrodes and what to use instead’. en. In: *npj Computational Materials* 6.1 (Aug. 2020). Number: 1 Publisher: Nature Publishing Group, pp. 1–12. ISSN: 2057-3960. DOI: 10.1038/s41524-020-00386-4. URL: <https://www.nature.com/articles/s41524-020-00386-4> (visited on 06/04/2022).

- [33] Quan-Qing Yu et al. ‘A Comparative Study on Open Circuit Voltage Models for Lithium-ion Batteries’. In: *Chinese Journal of Mechanical Engineering* 31.1 (17th Aug. 2018), p. 65. ISSN: 2192-8258. DOI: 10.1186/s10033-018-0268-8. URL: <https://doi.org/10.1186/s10033-018-0268-8> (visited on 31/03/2022).
- [34] Ahmet Aktaş and Yağmur Kirçiçek. *Solar Hybrid Systems*. English. 2021. URL: <https://www.sciencedirect.com/topics/engineering/battery-capacity> (visited on 20/04/2022).
- [35] Energizer Holdings. *Battery Internal Resistance*. English. 2005. URL: <https://data.energizer.com/pdfs/batteryir.pdf> (visited on 20/04/2022).
- [36] A. Jossen. ‘BATTERIES — Dynamics’. In: *Encyclopedia of Electrochemical Power Sources*. Ed. by Jürgen Garche. Amsterdam: Elsevier, 2009, pp. 478–488. ISBN: 978-0-444-52745-5. DOI: <https://doi.org/10.1016/B978-044452745-5.00940-0>. URL: <https://www.sciencedirect.com/science/article/pii/B9780444527455009400>.
- [37] Isidor Buchmann. *BU-402: What Is C-rate?* Battery University. 17th Feb. 2011. URL: <https://batteryuniversity.com/article/bu-402-what-is-c-rate> (visited on 30/03/2022).
- [38] Bengt Sundén. ‘Chapter 6 - Thermal management of batteries’. en. In: *Hydrogen, Batteries and Fuel Cells*. Ed. by Bengt Sundén. Academic Press, Jan. 2019, pp. 93–110. ISBN: 978-0-12-816950-6. DOI: 10.1016/B978-0-12-816950-6.00006-3. URL: <https://www.sciencedirect.com/science/article/pii/B9780128169506000063> (visited on 01/04/2022).
- [39] W. Waag and D. U. Sauer. ‘SECONDARY BATTERIES – LEAD– ACID SYSTEMS — State-of-Charge/Health’. en. In: *Encyclopedia of Electrochemical Power Sources*. Ed. by Jürgen Garche. Amsterdam: Elsevier, Jan. 2009, pp. 793–804. ISBN: 978-0-444-52745-5. DOI: 10.1016/B978-044452745-5.00149-0. URL: <https://www.sciencedirect.com/science/article/pii/B9780444527455001490> (visited on 19/05/2022).
- [40] Markus Solberg Wahl. *Batteries 1*. Lecture notes, FENT2011 Energy storage 1, NTNU. en. Apr. 2022. (Visited on 01/04/2022).
- [41] Witold Maranda. ‘Capacity Degradation of Lead-acid Batteries Under Variable-depth Cycling Operation in Photovoltaic System’. In: 1st June 2015. DOI: 10.1109/MIXDES.2015.7208584.
- [42] Chris South and Theresa Duncan. *Building Better Batteries: Characterize Battery Parameters for Simulation*. en-US. Apr. 2021. URL: <https://www.ansys.com/blog/building-better-batteries> (visited on 20/04/2022).
- [43] Anthony Barré et al. ‘A review on lithium-ion battery ageing mechanisms and estimations for automotive applications’. en. In: *Journal of Power Sources* 241 (Nov. 2013), pp. 680–689. ISSN: 0378-7753. DOI: 10.1016/j.jpowsour.2013.05.040. URL: <https://www.sciencedirect.com/science/article/pii/S0378775313008185> (visited on 04/04/2022).
- [44] Keith J. Laidler. *reaction rate — Facts & Formula — Britannica*. 2020. URL: <https://www.britannica.com/science/reaction-rate> (visited on 11/05/2022).
- [45] Muhammad Fahad Zia, Elhoussin Elbouchikhi and Mohamed Benbouzid. ‘Optimal Operational Planning of Scalable DC Microgrid with Demand Response, Islanding, and Battery Degradation Cost Considerations’. In: *Applied Energy* 237 (Mar. 2019), pp. 697–707. DOI: 10.1016/j.apenergy.2019.01.040.
- [46] Chelsea Snyder. ‘The effects of charge/discharge rate on capacity fade of lithium ion batteries’. Publication Title: Ph.D. Thesis ADS Bibcode: 2016PhDT.....260S. PhD thesis. 1st Jan. 2016. URL: <https://ui.adsabs.harvard.edu/abs/2016PhDT.....260S> (visited on 11/05/2022).
- [47] Martha A. Gialampouki, Javad Hashemi and Andrew A. Peterson. ‘The Electrochemical Mechanisms of Solid–Electrolyte Interphase Formation in Lithium-Based Batteries’. In: *The Journal of Physical Chemistry C* 123.33 (2019), pp. 20084–20092. DOI: 10.1021/acs.jpcc.9b03886. eprint: <https://doi.org/10.1021/acs.jpcc.9b03886>. URL: <https://doi.org/10.1021/acs.jpcc.9b03886>.
- [48] Jiagang Xu et al. ‘Electrode Side Reactions, Capacity Loss and Mechanical Degradation in Lithium-Ion Batteries’. In: *Journal of The Electrochemical Society* 162 (Jan. 2015), pp. 2026–2035. DOI: 10.1149/2.0291510jes].

- [49] Andrew Gordon. *Study Finds a Way to Prevent Fires in Next-Generation Lithium Batteries*. en. URL: <https://www6.slac.stanford.edu/news/2015-06-17-study-finds-way-prevent-fires-next-generation-lithium-batteries.aspx> (visited on 10/05/2022).
- [50] M.J. Moran et al. *Fundamentals of Engineering Thermodynamics, 9e WileyPLUS + Loose-leaf*. Wiley, 2018. ISBN: 9781119391760.
- [51] Guangming Liu et al. ‘Analysis of the heat generation of lithium-ion battery during charging and discharging considering different influencing factors’. In: *Journal of Thermal Analysis and Calorimetry* 116 (May 2014). DOI: 10.1007/s10973-013-3599-9.
- [52] Xiao-Feng Zhang et al. ‘Potentiometric measurement of entropy change for lithium batteries’. In: *Phys. Chem. Chem. Phys.* 19 (15 2017), pp. 9833–9842. DOI: 10.1039/C6CP08505A. URL: <http://dx.doi.org/10.1039/C6CP08505A>.
- [53] Suguna Thanagasundram et al. ‘A Cell Level Model for Battery Simulation’. In: Nov. 2012.
- [54] W. Wang et al. ‘Chapter 1 - Electrochemical cells for medium- and large-scale energy storage: fundamentals’. In: *Advances in Batteries for Medium and Large-Scale Energy Storage*. Ed. by Chris Menictas, Maria Skyllas-Kazacos and Tuti Mariana Lim. Woodhead Publishing Series in Energy. Woodhead Publishing, 2015, pp. 3–28. ISBN: 978-1-78242-013-2. DOI: <https://doi.org/10.1016/B978-1-78242-013-2.00001-7>. URL: <https://www.sciencedirect.com/science/article/pii/B9781782420132000017>.
- [55] Kangkang Wang et al. ‘Internal resistance and heat generation of soft package Li4Ti5O12 battery during charge and discharge’. In: *Energy* 149 (2018), pp. 364–374. ISSN: 0360-5442. DOI: <https://doi.org/10.1016/j.energy.2018.02.052>. URL: <https://www.sciencedirect.com/science/article/pii/S0360544218302809>.
- [56] Y.A. Çengel and A.J. Ghajar. *Heat and Mass Transfer: Fundamentals & Applications*. Asia Higher Education Engineering/Computer Science Mechanica. McGraw Hill Education, 2015. ISBN: 9789814595278.
- [57] Thomas S. Bryden et al. ‘Methodology to determine the heat capacity of lithium-ion cells’. In: *Journal of Power Sources* 395 (2018), pp. 369–378. ISSN: 0378-7753. DOI: <https://doi.org/10.1016/j.jpowsour.2018.05.084>. URL: <https://www.sciencedirect.com/science/article/pii/S0378775318305688>.
- [58] Dieter Haemmerich. ‘1 - Mathematical modeling of heat transfer in biological tissues (bioheat transfer)’. en. In: *Principles and Technologies for Electromagnetic Energy Based Therapies*. Ed. by Punit Prakash and Govindarajan Srimathveeravalli. Academic Press, Jan. 2022, pp. 1–24. ISBN: 978-0-12-820594-5. DOI: 10.1016/B978-0-12-820594-5.00012-5. URL: <https://www.sciencedirect.com/science/article/pii/B9780128205945000125> (visited on 19/05/2022).
- [59] Kazuaki Kisu et al. ‘Internal resistance mapping preparation to optimize electrode thickness and density using symmetric cell for high-performance lithium-ion batteries and capacitors’. In: *Journal of Power Sources* 396 (2018), pp. 207–212. ISSN: 0378-7753. DOI: <https://doi.org/10.1016/j.jpowsour.2018.05.083>. URL: <https://www.sciencedirect.com/science/article/pii/S0378775318305676>.
- [60] David L. Chandler. *How to prevent short-circuiting in next-gen lithium batteries*. en. URL: <https://news.mit.edu/2021/dendrite-prevent-lithium-batteries-0316> (visited on 28/03/2022).
- [61] O. Chernysh et al. ‘Effect of binder’s solvent on the electrochemical performance of electrodes for lithium-ion batteries and supercapacitors’. In: *Materials Today: Proceedings* 6 (2019). 3rd ISE Satellite Student Regional Symposium on Electrochemistry in Ukraine – Promising Materials and Processes in Applied Electrochemistry-2018, 18th April, 2018, Ukraine, pp. 42–47. ISSN: 2214-7853. DOI: <https://doi.org/10.1016/j.matpr.2018.10.073>. URL: <https://www.sciencedirect.com/science/article/pii/S2214785318323678>.
- [62] Amrita Sarkar et al. ‘Recovery and Reuse of Composite Cathode Binder in Lithium Ion Batteries’. In: *ChemistryOpen* 10.5 (May 2021), pp. 545–552. ISSN: 2191-1363. DOI: 10.1002/open.202100060. URL: <https://www.ncbi.nlm.nih.gov/pmc/articles/PMC8095295/> (visited on 06/05/2022).
- [63] Kaylee Towey and Kelsie Oshinsky. *NMP: Manufacturing Uses and Hazards*. en-US. Section: News. URL: <https://www.miltec.com/en/news/nmp-manufacturing-uses-and-hazards/> (visited on 06/05/2022).

- [64] Yet-Ming Chiang et al. ‘Damage tolerant batteries’. en. US10230128B2. Mar. 2019. URL: <https://patents.google.com/patent/US10230128B2/en> (visited on 30/03/2022).
- [65] Callie W. Babbitt. ‘Sustainability perspectives on lithium-ion batteries’. In: *Clean Technologies and Environmental Policy* 22.6 (1st Aug. 2020), pp. 1213–1214. ISSN: 1618-9558. DOI: 10.1007/s10098-020-01890-3. URL: <https://doi.org/10.1007/s10098-020-01890-3> (visited on 01/04/2022).
- [66] Melissa Pistilli. *Top Cobalt Production by Country*. INN. Section: How to Invest in Cobalt. 21st June 2021. URL: <https://investingnews.com/where-is-cobalt-mined/> (visited on 04/04/2022).
- [67] Storm William D. Gourley, Tyler Or and Zhongwei Chen. ‘Breaking Free from Cobalt Reliance in Lithium-Ion Batteries’. In: *iScience* 23.9 (25th Sept. 2020), p. 101505. ISSN: 2589-0042. DOI: 10.1016/j.isci.2020.101505. URL: <https://www.sciencedirect.com/science/article/pii/S2589004220306970> (visited on 01/04/2022).
- [68] Yue Yang et al. ‘On the sustainability of lithium ion battery industry – A review and perspective’. In: *Energy Storage Materials* 36 (1st Apr. 2021), pp. 186–212. ISSN: 2405-8297. DOI: 10.1016/j.ensm.2020.12.019. URL: <https://www.sciencedirect.com/science/article/pii/S2405829720304827> (visited on 05/05/2022).
- [69] Frank Richter et al. ‘Measurements of ageing and thermal conductivity in a secondary NMC-hard carbon Li-ion battery and the impact on internal temperature profiles’. In: *Electrochimica Acta* 250 (1st Oct. 2017), pp. 228–237. ISSN: 0013-4686. DOI: 10.1016/j.electacta.2017.07.173. URL: <https://www.sciencedirect.com/science/article/pii/S0013468617316146> (visited on 06/04/2022).
- [70] Seraph Hu. ‘Power Efficient Battery Formation’. en. In: (), p. 4. URL: <https://www.analog.com/en/technical-articles/power-efficient-battery-formation.html>.
- [71] Seong Jin An et al. ‘Fast formation cycling for lithium ion batteries’. In: *Journal of Power Sources* 342 (2017), pp. 846–852. ISSN: 0378-7753. DOI: <https://doi.org/10.1016/j.jpowsour.2017.01.011>. URL: <https://www.sciencedirect.com/science/article/pii/S0378775317300113>.
- [72] Hans-Georg Schweiger et al. ‘Comparison of Several Methods for Determining the Internal Resistance of Lithium Ion Cells’. In: *Sensors (Basel, Switzerland)* 10 (June 2010), pp. 5604–25. DOI: 10.3390/s100605604.
- [73] Yue Ming et al. ‘Effect of Thickness on the Thermal Conductivity and Microstructure of Die-Cast AZ91D Magnesium Alloy’. en. In: *Metallurgical and Materials Transactions A* 50.12 (Dec. 2019), pp. 5969–5976. ISSN: 1543-1940. DOI: 10.1007/s11661-019-05473-w. URL: <https://doi.org/10.1007/s11661-019-05473-w> (visited on 19/05/2022).
- [74] Jinlong He, Lin Zhang and Ling Liu. ‘Improving thermal conduction across cathode/electrolyte interfaces in solid-state lithium-ion batteries by hierarchical hydrogen-bond network’. In: *Materials Design* 194 (2020), p. 108927. ISSN: 0264-1275. DOI: <https://doi.org/10.1016/j.matdes.2020.108927>. URL: <https://www.sciencedirect.com/science/article/pii/S0264127520304615>.
- [75] Shunli Wang et al. ‘Chapter 1 - Lithium-ion battery characteristics and applications’. In: *Battery System Modeling*. Ed. by Shunli Wang et al. Elsevier, 2021, pp. 1–46. ISBN: 978-0-323-90472-8. DOI: <https://doi.org/10.1016/B978-0-323-90472-8.00003-2>. URL: <https://www.sciencedirect.com/science/article/pii/B9780323904728000032>.

Appendices

A MATLAB Scripts

A.1 Specific Heat Capacity

```
1 clear all; close all; clc
2
3 %% Semi-solid state cell stack
4
5 data1 = readtable('temp_SSS_stacked','readvariablenames',true
6 , 'preservevariablename',true); % data file for the semi-solid state
   test
7
8 test_time = table2array(data1(:,2)); % time vector [time of day]
9 test_time_sec = seconds(test_time); % time vector [s]
10 test_time_plot = test_time_sec - 56525; % to make the first time
   element become 0 seconds
11
12 temp1 = table2array(data1(:,4)); % temperature vector 1 [degrees C]
13 temp2 = table2array(data1(:,5)); % temperature vector 2 [degrees C]
14 temp3 = table2array(data1(:,6)); % temperature vector 3 [degrees C]
15
16 figure(1) % plot of temperature over time for semi-solid state stack
17 %title('Temperature development against time for three thermocouples')
18 plot(test_time_plot, temp1, '-r', 'Linewidth',2)
19 set(gca, 'FontSize',14)
20 xlabel('Time [s]', 'FontSize',20, 'interpreter', 'latex')
21 ylabel('Temperature [^\circ C]', 'FontSize',20, 'interpreter', 'latex')
22 hold on
23 plot(test_time_plot, temp2, '-g', 'Linewidth',2)
24 plot(test_time_plot, temp3, '-b', 'Linewidth',2)
25 hold off
26 grid
27 legend(['Thermocouple in the water'], ['Thermocouple under the cell
   stack'], ['Thermocouple on the cell stack'], 'FontSize',17, '
   interpreter', 'latex')
28
29 %% Conventional cell stack
30
31 data2 = readtable('temp_conv_stacked','readvariablenames',true
32 , 'preservevariablename',true); % data file for the conventional test
33
34 test_time = table2array(data2(:,2)); % time vector [time of day]
35 test_time_sec = seconds(test_time); % time vector [s]
36 test_time_plot = test_time_sec - 51863; % to make the first time
   element
37
   % become 0 seconds
38
39 temp1 = table2array(data2(:,4)); % temperature vector 1 [degrees C]
40 temp2 = table2array(data2(:,5)); % temperature vector 2 [degrees C]
41 temp3 = table2array(data2(:,6)); % temperature vector 3 [degrees C]
42
43 figure(2) % plot of temperature over time for conventional stack
44 %title('Temperature development against time for three thermocouples')
45 plot(test_time_plot, temp1, '-r', 'Linewidth',2)
```

```
46 set(gca,'FontSize',14)
47 xlabel('Time [s]', 'FontSize',20, 'interpreter','latex')
48 ylabel('Temperature [ $^{\circ}$ C]', 'FontSize',20, 'interpreter','latex')
49 hold on
50 plot(test_time_plot, temp2, '-g', 'Linewidth',2)
51 plot(test_time_plot, temp3, '-b', 'Linewidth',2)
52 hold off
53 grid
54 legend(['Thermocouple in the water'], ['Thermocouple under the cell
      stack'], ['Thermocouple on the cell stack'], 'FontSize',17, '
      interpreter','latex')
```

A.2 Internal Resistance and Specific Heat Generation

```
1 %% Conventional cell nr. 2
2 clear all; close all; clc
3
4 data = readmatrix('conventional_2-formation_Channel-11'); % data file
5 % matrix
6 test_time_s = data(:,3); % time vector [s]
7 test_time_min = data(:,3)/60; % time vector [min]
8 test_time_h = data(:,3)/3600; % time vector [h]
9 current = data(:,7); % current vector [A]
10 voltage = data(:,8); % voltage vector [V]
11
12 figure(1) % plot of the whole test
13 %title('Voltage and current against time')
14 yyaxis left
15 plot(test_time_h, voltage, 'Linewidth',1.5)
16 set(gca, 'FontSize',14)
17 xlabel('Time (h)', 'FontSize',20, 'interpreter', 'latex')
18 ylabel('Voltage (V)', 'FontSize',20, 'interpreter', 'latex')
19 grid
20 hold on
21 yyaxis right
22 plot(test_time_h, current, 'Linewidth',1.5)
23 ylim([-0.011,0.026])
24 ylabel('Current (A)', 'FontSize',20, 'interpreter', 'latex')
25 legend(['Voltage'], ['Current'], 'FontSize',17, 'interpreter', 'latex')
26
27 figure(2) % plot from t=0 to end of formation process
28 %title('Voltage and current against time during formation process')
29 yyaxis left
30 plot(test_time_min, voltage, 'Linewidth',1.5)
31 set(gca, 'FontSize',14)
32 xlabel('Time (min)', 'FontSize',20, 'interpreter', 'latex')
33 ylabel('Voltage (V)', 'FontSize',20, 'interpreter', 'latex')
34 grid
35 hold on
36 yyaxis right
37 plot(test_time_min, current, 'Linewidth',1.5)
38 ylim([-0.011,0.011])
39 ylabel('Current (A)', 'FontSize',20, 'interpreter', 'latex')
40 legend(['Voltage'], ['Current'], 'FontSize',17, 'interpreter', 'latex')
41 xlim([0,360])
42
43 figure(3) % zoomed plot of the formation process
44 %title('Voltage and current against time during formation process')
45 yyaxis left
46 plot(test_time_min, voltage, 'Linewidth',1.5)
47 set(gca, 'FontSize',14)
48 xlabel('Time (min)', 'FontSize',20, 'interpreter', 'latex')
49 ylabel('Voltage (V)', 'FontSize',20, 'interpreter', 'latex')
50 grid
51 hold on
52 yyaxis right
53 plot(test_time_min, current, 'Linewidth',1.5)
54 ylim([-0.011,0.011])
55 ylabel('Current (A)', 'FontSize',20, 'interpreter', 'latex')
56 legend(['Voltage'], ['Current'], 'FontSize',17, 'interpreter', 'latex')
```

```

57 xlim([200,360])
58
59 figure(4) % plot of the whole HPPC process (all five tests)
60 %title('Voltage and current against time during HPPC test ')
61 yyaxis left
62 plot(test_time_min, voltage, 'Linewidth',1.5)
63 ylim([2.7,4.5])
64 set(gca, 'FontSize',14)
65 xlabel('Time (min)', 'FontSize',20, 'interpreter', 'latex')
66 ylabel('Voltage (V)', 'FontSize',20, 'interpreter', 'latex')
67 grid
68 hold on
69 yyaxis right
70 plot(test_time_min, current, 'Linewidth',1.5)
71 ylim([-0.03,0.03])
72 ylabel('Current (A)', 'FontSize',20, 'interpreter', 'latex')
73 legend(['Voltage'], ['Current'], 'FontSize',17, 'interpreter', 'latex')
74 xlim([500,700])
75
76 figure(5) % plot of the second HPPC test (90% SOC)
77 %title('Voltage and current against time during HPPC test ')
78 yyaxis left
79 plot(test_time_min, voltage, 'Linewidth',1.5)
80 ylim([2.6,4.3])
81 set(gca, 'FontSize',14)
82 xlabel('Time (min)', 'FontSize',20, 'interpreter', 'latex')
83 ylabel('Voltage (V)', 'FontSize',20, 'interpreter', 'latex')
84 grid on
85 hold on
86 yyaxis right
87 plot(test_time_min, current, 'Linewidth',1.5)
88 ylim([-0.013,0.013])
89 ylabel('Current (A)', 'FontSize',20, 'interpreter', 'latex')
90 legend(['Voltage'], ['Current'], 'FontSize',17, 'interpreter', 'latex')
91 xlim([560,561])
92
93 figure(6) % zoomed plot of the second HPPC test (90% SOC)
94 %title('Voltage and current against time during HPPC test at 90% SOC')
95 yyaxis left
96 plot(test_time_min, voltage, 'Linewidth',1.5)
97 ylim([2.6,4.3])
98 set(gca, 'FontSize',14)
99 xlabel('Time (min)', 'FontSize',20, 'interpreter', 'latex')
100 ylabel('Voltage (V)', 'FontSize',20, 'interpreter', 'latex')
101 grid on
102 hold on
103 yyaxis right
104 plot(test_time_min, current, 'Linewidth',1.5)
105 ylim([-0.013,0.013])
106 ylabel('Current (A)', 'FontSize',20, 'interpreter', 'latex')
107 legend(['Voltage'], ['Current'], 'FontSize',17, 'interpreter', 'latex')
108 xlim([560.15,560.58])
109
110 %% Conventional cell nr. 3
111 clear all; close all; clc
112
113 data = readmatrix('conventional_3-formation_Channel_13'); % data file
114 % matrix

```

```

115 test_time_s = data(:,3); % time vector [s]
116 test_time_min = data(:,3)/60; % time vector [min]
117 test_time_h = data(:,3)/3600; % time vector [h]
118 current = data(:,7); % current vector [A]
119 voltage = data(:,8); % voltage vector [V]
120
121 figure(1) % plot of the whole test
122 %title('Voltage and current against time')
123 yyaxis left
124 plot(test_time_h, voltage, 'Linewidth',1.5)
125 set(gca, 'FontSize',14)
126 xlabel('Time (h)', 'FontSize',20, 'interpreter', 'latex')
127 ylabel('Voltage (V)', 'FontSize',20, 'interpreter', 'latex')
128 grid
129 hold on
130 yyaxis right
131 plot(test_time_h, current, 'Linewidth',1.5)
132 ylabel('Current (A)', 'FontSize',20, 'interpreter', 'latex')
133 legend(['Voltage'], ['Current'], 'FontSize',17, 'interpreter', 'latex')
134
135 figure(2) % plot from t=0 to end of formation process
136 %title('Voltage and current against time during formation process')
137 yyaxis left
138 plot(test_time_min, voltage, 'Linewidth',1.5)
139 ylim([3.4,4.23])
140 set(gca, 'FontSize',14)
141 xlabel('Time (min)', 'FontSize',20, 'interpreter', 'latex')
142 ylabel('Voltage (V)', 'FontSize',20, 'interpreter', 'latex')
143 grid
144 hold on
145 yyaxis right
146 plot(test_time_min, current, 'Linewidth',1.5)
147 ylim([-0.017,0.017])
148 ylabel('Current (A)', 'FontSize',20, 'interpreter', 'latex')
149 legend(['Voltage'], ['Current'], 'FontSize',17, 'interpreter', 'latex')
150 xlim([0,160])
151
152 figure(3) % zoomed plot of the formation process
153 %title('Voltage and current against time during formation process')
154 yyaxis left
155 plot(test_time_min, voltage, 'Linewidth',1.5)
156 set(gca, 'FontSize',14)
157 xlabel('Time (min)', 'FontSize',20, 'interpreter', 'latex')
158 ylabel('Voltage (V)', 'FontSize',20, 'interpreter', 'latex')
159 grid
160 hold on
161 yyaxis right
162 plot(test_time_min, current, 'Linewidth',1.5)
163 ylabel('Current (A)', 'FontSize',20, 'interpreter', 'latex')
164 legend(['Voltage'], ['Current'], 'FontSize',17, 'interpreter', 'latex')
165 xlim([132,150])
166
167 figure(4) % plot of the whole HPPC process (all five tests)
168 %title('Voltage and current against time during HPPC test')
169 yyaxis left
170 plot(test_time_min, voltage, 'Linewidth',1.5)
171 ylim([2.2,4.8])
172 set(gca, 'FontSize',14)

```

```

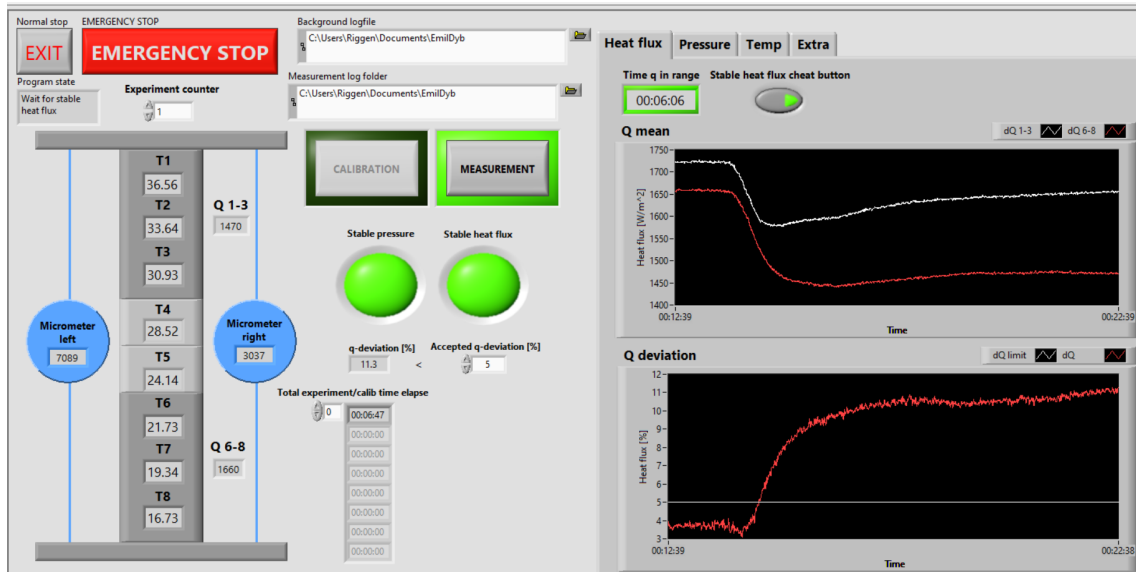
173 xlabel('Time (min)', 'FontSize', 20, 'interpreter', 'latex')
174 ylabel('Voltage (V)', 'FontSize', 20, 'interpreter', 'latex')
175 grid
176 hold on
177 yyaxis right
178 plot(test_time_min, current, 'Linewidth', 1.5)
179 ylim([-0.07, 0.05])
180 ylabel('Current (A)', 'FontSize', 20, 'interpreter', 'latex')
181 legend(['Voltage'], ['Current'], 'FontSize', 17, 'interpreter', 'latex')
182 xlim([300, 515])
183
184 figure(5) % zoomed plot of the second HPPC test (90% SOC)
185 %title('Voltage and current against time during HPPC test at 90% SOC')
186 yyaxis left
187 plot(test_time_min, voltage, 'Linewidth', 1.5)
188 ylim([3.2, 4.3])
189 set(gca, 'FontSize', 14)
190 xlabel('Time (min)', 'FontSize', 20, 'interpreter', 'latex')
191 ylabel('Voltage (V)', 'FontSize', 20, 'interpreter', 'latex')
192 grid on
193 hold on
194 yyaxis right
195 plot(test_time_min, current, 'Linewidth', 1.5)
196 ylim([-0.03, 0.03])
197 ylabel('Current (A)', 'FontSize', 20, 'interpreter', 'latex')
198 legend(['Voltage'], ['Current'], 'FontSize', 17, 'interpreter', 'latex')
199 xlim([366.98, 367.42])
200
201 %% Comparison
202 clear all; close all; clc
203
204 SOC = [0.71, 0.76, 0.8, 0.9, 1]*100; % State of charge [%]
205 IR_conv2_disch = [30, 27, 28, 18, 9]; % Internal resistance
      conventional cell 2 [ohm]
206 IR_conv3_disch = [30.67, 23.33, 16.67, 16.67, 7.89]; % Internal
      resistance conventional cell 3 [ohm]
207 IR_conv2_charge = [29, 28, 27, 17, 9]; % Internal resistance
      conventional cell 2 [ohm]
208 IR_conv3_charge = [23.33, 19.33, 16, 15.33, 8.16]; % Internal
      resistance conventional cell 3 [ohm]
209
210 q_conv2_disch = [0.68, 0.61, 0.63, 0.41, 0.2]; % Specific heat
      generation cell 2 [W/kg]
211 q_conv3_disch = [1.64, 1.25, 0.89, 0.89, 2.71]; % Specific heat
      generation cell 3 [W/kg]
212 q_conv2_charge = [0.66, 0.63, 0.61, 0.31, 0.2]; % Specific heat
      generation cell 2 [W/kg]
213 q_conv3_charge = [1.25, 1.03, 0.85, 0.82, 2.8]; % Specific heat
      generation cell 3 [W/kg]
214
215 figure(1) % plot of internal resistance against SOC for both cells
216 plot(SOC, IR_conv2_disch, 'r-o', 'Linewidth', 1.5)
217 set(gca, 'xdir', 'reverse', 'FontSize', 14)
218 xlabel('State of charge [%]', 'FontSize', 20, 'interpreter', 'latex')
219 ylabel('Internal resistance [ $\Omega$ ]', 'FontSize', 20, 'interpreter',
      'latex')
220 grid on
221 hold on

```

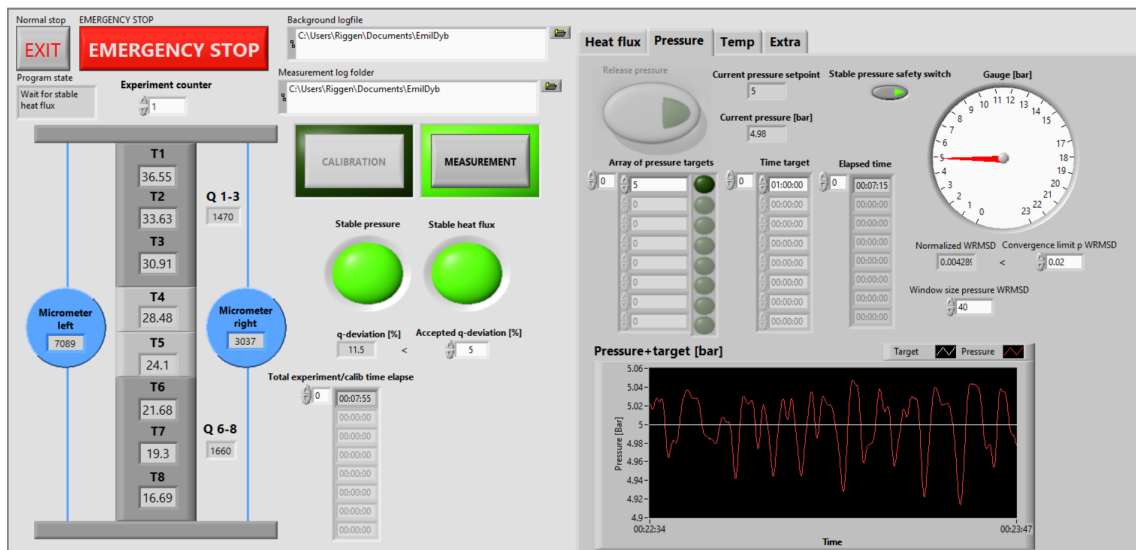
```
222 plot(SOC, IR_conv3_disch, 'b-o', 'Linewidth',1.5)
223 plot(SOC, IR_conv2_charge, 'm-o', 'Linewidth',1.5)
224 plot(SOC, IR_conv3_charge, 'g-o', 'Linewidth',1.5)
225 legend(['Conventional cell 2 - discharge'], ['Conventional cell 3 -
        discharge'], ['Conventional cell 2 - charge'], ['Conventional cell 3
        - charge'], 'FontSize',17, 'interpreter', 'latex')
226
227 figure(2) % plot of specific heat generation against SOC for both cells
228 plot(SOC, q_conv2_disch, 'r-o', 'Linewidth',1.5)
229 set(gca, 'xdir', 'reverse', 'FontSize',14)
230 xlabel('State of charge [%]', 'FontSize',20, 'interpreter', 'latex')
231 ylabel('Specific heat generation [W/kg]', 'FontSize',20, 'interpreter', '
        latex')
232 grid on
233 hold on
234 plot(SOC, q_conv3_disch, 'b-o', 'Linewidth',1.5)
235 plot(SOC, q_conv2_charge, 'm-o', 'Linewidth',1.5)
236 plot(SOC, q_conv3_charge, 'g-o', 'Linewidth',1.5)
237 legend(['Conventional cell 2 - discharge'], ['Conventional cell 3 -
        discharge'], ['Conventional cell 2 - charge'], ['Conventional cell 3
        - charge'], 'FontSize',17, 'interpreter', 'latex')
```

B LabVIEW

B.1 Thermal Conductivity

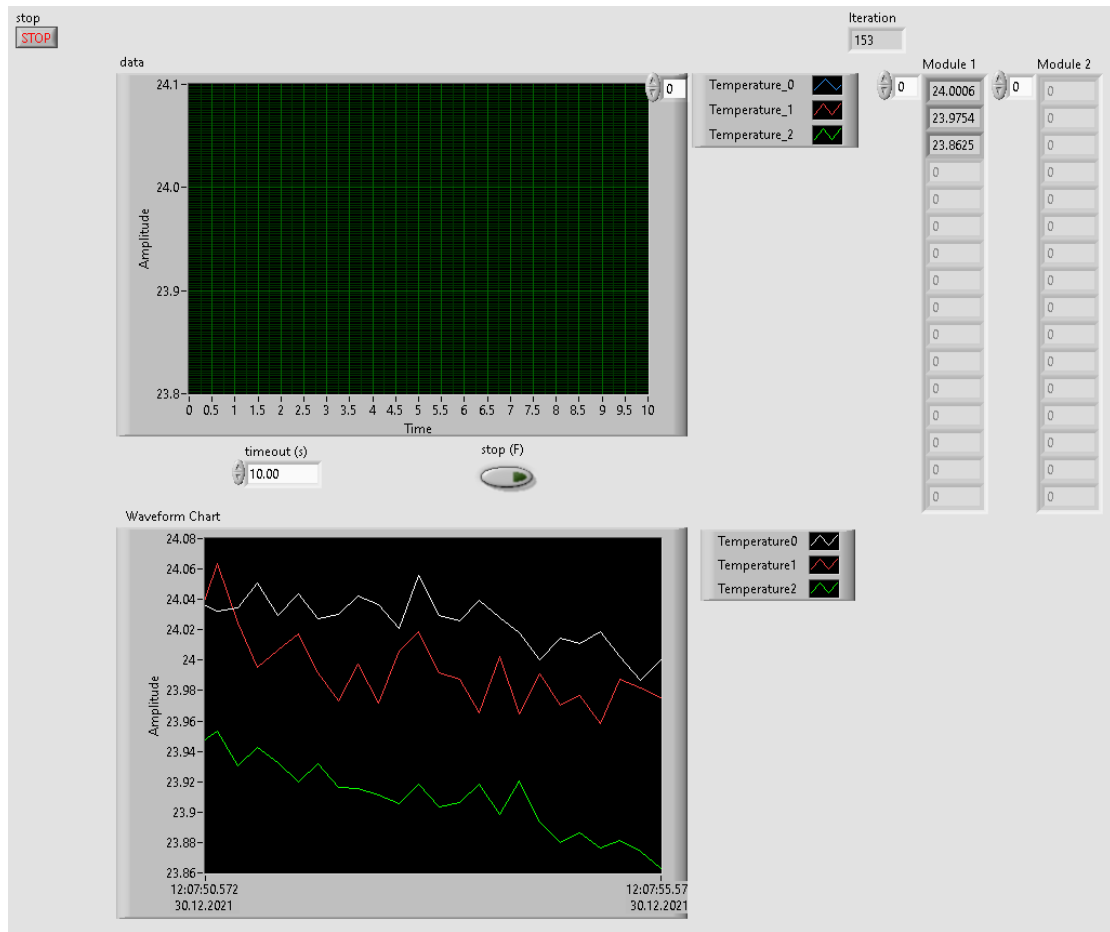


LabVIEW program for thermal conductivity measurements, showing the heat flux window.

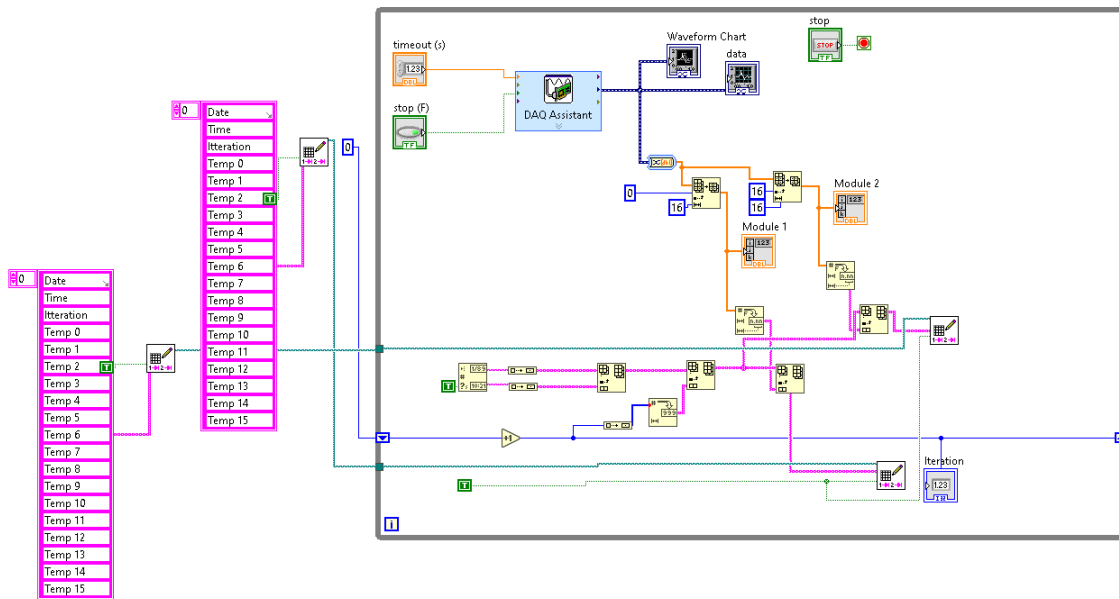


LabVIEW program for thermal conductivity measurements, showing the pressure window.

B.2 Specific Heat Capacity



LabVIEW program for specific heat capacity measurements, showing the layout of the temperature measurements.



LabVIEW program for specific heat capacity measurements, showing the block diagram of the system.

C Formation and HPPC-Program

	Step Label	Number Of Limits	Control Type	Control Value	Extra Control Value 1	Extra Control Value 2
1	Initial rest	2	Rest			
	Add Limit		Goto Step	Variable1	Operator1	Value1
	Step Limits	1	Next Step	PV_CHAN_Step_Time	>=	00:01:00
	Log Limits	2		DV_Time	>=	00:00:10
2	Internal resistance - 1	1	Internal Resistance	Amp:0.005	ms:60.00	Offset:0
	Add Limit		Goto Step	Variable1	Operator1	Value1
	Step Limits	1	Next Step			
3	Reset capacities - 1	1	Set Variable(s)	Reset	Increment	Decrement
	Add Limit		Goto Step	Variable1	Operator1	Value1
	Step Limits	1	Next Step	PV_CHAN_Step_Time	>=	00:00:00
4	Formation partial/full charge	2	C-Rate	0.2		
	Add Limit		Goto Step	Variable1	Operator1	Value1
	Step Limits	1	Next Step	PV_CHAN_Voltage	>=	4.2
	Log Limits	2		DV_Time	>=	00:00:30
5	Decide to finish formation	3	Rest			
	Add Limit		Goto Step	Variable1	Operator1	Value1
	Step Limits	1	Formation complete discharge	TC_Counter1	>=	5
		2	Formation partial discharge	TC_Counter1	<	5
	Log Limits	3		DV_Time	>=	00:01:00
6	Formation partial discharge	2	C-Rate	-0.2		
	Add Limit		Goto Step	Variable1	Operator1	Value1
	Step Limits	1	Reset capacities - 1	PV_CHAN_Voltage	<=	3.9
	Log Limits	2		DV_Time	>=	00:00:30
7	Formation complete discharge	2	C-Rate	-0.2		
	Add Limit		Goto Step	Variable1	Operator1	Value1
	Step Limits	1	Next Step	PV_CHAN_Voltage	<	3
	Log Limits	2		DV_Time	>=	00:00:30
8	Rest after formation	2	Rest			
	Add Limit		Goto Step	Variable1	Operator1	Value1
	Step Limits	1	Next Step	PV_CHAN_Step_Time	>=	00:10:00
	Log Limits	2		DV_Time	>=	00:00:30
9	Internal resistance - 2	1	Internal Resistance	Amp:0.005	ms:60.00	Offset:0
	Add Limit		Goto Step	Variable1	Operator1	Value1
	Step Limits	1	Next Step			
10	Reset capacities and counters (before HPPC)	1	Set Variable(s)	Reset	Increment	Decrement
	Add Limit		Goto Step	Variable1	Operator1	Value1
	Step Limits	1	Next Step	PV_CHAN_Step_Time	>=	00:00:00
11	CC charge before HPPC	2	C-Rate	0.5		
	Add Limit		Goto Step	Variable1	Operator1	Value1
	Step Limits	1	Next Step	PV_CHAN_Voltage	>=	4.2
	Log Limits	2		DV_Time	>=	00:00:30
12	CV charge before HPPC	2	Voltage(V)	(V):4.2		IR(ohm):0
	Add Limit		Goto Step	Variable1	Operator1	Value1
	Step Limits	1	Next Step	PV_CHAN_Current	<=	0.005
	Log Limits	2		DV_Time	>=	00:00:30
13	Rest at upper voltage before HPPC	2	Rest			
	Add Limit		Goto Step	Variable1	Operator1	Value1
	Step Limits	1	Next Step	PV_CHAN_Step_Time	>=	00:10:00
	Log Limits	2		DV_Time	>=	00:00:30
14	Negative HPPC pulse - 1	2	C-Rate	-0.2		
	Add Limit		Goto Step	Variable1	Operator1	Value1
	Step Limits	1	Next Step	PV_CHAN_Step_Time	>=	00:00:05
	Log Limits	2		DV_Time	>=	00:00:00:005
15	Rest after HPPC pulse - 1	2	Rest			
	Add Limit		Goto Step	Variable1	Operator1	Value1
	Step Limits	1	Next Step	PV_CHAN_Step_Time	>=	00:00:01
	Log Limits	2		DV_Time	>=	00:00:00:005

16	Proceed to discharge HPPC	2	Set Variable(s)	Reset	Increment	Decrement
	Add Limit		Goto Step	Variable1	Operator1	Value1
	Step Limits	1	Next Step	TC_Counter1	>=	3
		2	Negative HPPC pulse - 1	TC_Counter1	<	3
17	Reset counters	1	Set Variable(s)	Reset	Increment	Decrement
	Add Limit		Goto Step	Variable1	Operator1	Value1
	Step Limits	1	Next Step	PV_CHAN_Step_Time	>=	00:00:00
18	Partial discharge HPPC	3	C-Rate	-0.1		
	Add Limit		Goto Step	Variable1	Operator1	Value1
	Step Limits	1	Final rest	PV_CHAN_Voltage	<=	3
		2	Next Step	PV_CHAN_Step_Time	>=	00:30:00
	Log Limits	3		DV_Time	>=	00:00:30
19	Rest before HPPC pulses	2	Rest			
	Add Limit		Goto Step	Variable1	Operator1	Value1
	Step Limits	1	Next Step	PV_CHAN_Step_Time	>=	00:10:00
	Log Limits	2		DV_Time	>=	00:00:30
20	Check if close to lower cut-off voltage	3	Rest			
	Add Limit		Goto Step	Variable1	Operator1	Value1
	Step Limits	1	Next Step	PV_CHAN_Voltage	>=	3.5
		2	Positive HPPC pulse - 2	PV_CHAN_Voltage	<	3.5
	Log Limits	3		DV_Time	>=	00:00:01
21	Negative HPPC pulse - 2	2	C-Rate	-0.2		
	Add Limit		Goto Step	Variable1	Operator1	Value1
	Step Limits	1	Next Step	PV_CHAN_Step_Time	>=	00:00:05
	Log Limits	2		DV_Time	>=	00:00:00:005
22	Rest after negative HPPC pulse	2	Rest			
	Add Limit		Goto Step	Variable1	Operator1	Value1
	Step Limits	1	Next Step	PV_CHAN_Step_Time	>=	00:00:01
	Log Limits	2		DV_Time	>=	00:00:00:005
23	Positive HPPC pulse - 2	2	C-Rate	0.2		
	Add Limit		Goto Step	Variable1	Operator1	Value1
	Step Limits	1	Next Step	PV_CHAN_Step_Time	>=	00:00:05
	Log Limits	2		DV_Time	>=	00:00:00:005
24	Rest after positive HPPC pulse	2	Rest			
	Add Limit		Goto Step	Variable1	Operator1	Value1
	Step Limits	1	Next Step	PV_CHAN_Step_Time	>=	00:00:01
	Log Limits	2		DV_Time	>=	00:00:00:005
25	Repeat 3x HPPC pulses	2	Set Variable(s)	Reset	Increment	Decrement
	Add Limit		Goto Step	Variable1	Operator1	Value1
	Step Limits	1	Next Step	TC_Counter1	>=	3
		2	Check if close to lower cut-off voltage	TC_Counter1	<	3
26	Loop back to partial discharge HPPC	1	Set Variable(s)	Reset	Increment	Decrement
	Add Limit		Goto Step	Variable1	Operator1	Value1
	Step Limits	1	Partial discharge HPPC	PV_CHAN_Step_Time	>=	00:00:00
27	Final rest	2	Rest			
	Add Limit		Goto Step	Variable1	Operator1	Value1
	Step Limits	1	Next Step	PV_CHAN_Step_Time	>=	00:15:00
	Log Limits	2		DV_Time	>=	00:00:30

